



**Search for Long-Lived Neutral Particles in Final State  
with Delayed Photons and Missing Transverse Energy in  
 $pp$  Collisions at  $\sqrt{S} = 8$  TeV**

A DISSERTATION  
SUBMITTED TO THE FACULTY OF THE GRADUATE SCHOOL  
OF THE UNIVERSITY OF MINNESOTA  
BY

**Tambe Ebai Norbert**

IN PARTIAL FULFILLMENT OF THE REQUIREMENTS  
FOR THE DEGREE OF  
Doctor of Philosophy

**Prof. Yuichi Kubota**

**October, 2015**

**© Tambe Ebai Norbert 2015  
ALL RIGHTS RESERVED**

# Acknowledgements

# Dedication

## Abstract

We perform a search for long-lived neutral particles in final state with delayed photons and large missing transverse energy produced in LHC proton-proton collisions at center-of-mass energy,  $\sqrt{S} = 8\text{ TeV}$ . Capitalizing on the excellent timing resolution of the CMS Electromagnetic Calorimeter, the search uses photon time measurements made by the Electromagnetic Calorimeter as the main search quantity. We found a single event consistent with our background expectations from the Standard Model and proceed to compute limits on the number of events. We also interpret these results in the context of the SPS8 benchmark GMSB model and show that light neutralinos with mean lifetime,  $\tau_{\tilde{\chi}_1^0} \leq 45\text{ ns}$ , and mass,  $m_{\tilde{\chi}_1^0} \leq 300\text{ GeV}/c^2$ , or effective Supersymmetry breaking energy scale,  $\Lambda \leq 220\text{ TeV}$ , are ruled out of existence at 95%  $CL_S$  confidence level. The exclusion limit on the product of the production cross section and branching ratio of the lightest neutralino to photon and gravitino decay channel,  $\sigma_{(\tilde{\chi}_1^0 \rightarrow \gamma + \tilde{G})} \times BR$ , for different lifetimes and masses is given. These results confirm for the first time that the CMS Electromagnetic Calorimeter provides good sensitivity using only timing measurements to search for long-lived neutral particles with lifetime up to 40 ns and masses up to  $300\text{ GeV}/c^2$ .

# Contents

<b>Acknowledgements</b>	<b>i</b>
<b>Dedication</b>	<b>ii</b>
<b>Abstract</b>	<b>iii</b>
<b>List of Tables</b>	<b>viii</b>
<b>List of Figures</b>	<b>x</b>
<b>1 Introduction</b>	<b>1</b>
<b>2 Phenomenology of Long-Lived Particles</b>	<b>3</b>
2.1 The Standard Model . . . . .	3
2.1.1 Fermions . . . . .	3
2.1.2 Bosons . . . . .	4
2.1.3 Spontaneous Symmetry Breaking . . . . .	4
2.1.4 Beyond Standard Model Physics . . . . .	9
2.2 Supersymmetry . . . . .	12
2.2.1 The Minimal Supersymmetric Standard Model . . . . .	12
2.3 Gauge Mediated Supersymmetry Breaking Models . . . . .	17
2.3.1 Long-Lived Neutral Particles in GMSB Models . . . . .	19
2.3.2 Benchmark Scenario . . . . .	22
2.3.3 Signal Modeling . . . . .	24
2.3.4 Lifetime of the Lightest Neutralino . . . . .	29

2.4	Previous Search Experiments . . . . .	32
<b>3</b>	<b>Hadron Collider and Detector</b>	<b>35</b>
3.1	Large Hadron Collider . . . . .	35
3.1.1	Overview . . . . .	35
3.1.2	Colliding Energy . . . . .	36
3.1.3	Luminosity . . . . .	37
3.1.4	LHC Bunch Structure . . . . .	39
3.2	Compact Muon Solenoid . . . . .	41
3.2.1	Overview . . . . .	41
3.2.2	Calorimeters . . . . .	42
3.2.3	Muon Chambers . . . . .	55
3.2.4	Event Triggering . . . . .	56
<b>4</b>	<b>Time Reconstruction and Resolution</b>	<b>60</b>
4.1	Time Reconstruction . . . . .	60
4.2	ECAL Time Performance from Test Beam . . . . .	62
4.2.1	ECAL Time Resolution . . . . .	62
4.3	ECAL Time Performance from Collision . . . . .	64
4.3.1	Crystal Time Synchronization . . . . .	65
4.3.2	Time Bias . . . . .	70
4.4	ECAL Time Performance With Z Bosons . . . . .	72
<b>5</b>	<b>Event Reconstruction</b>	<b>76</b>
5.1	Event Reconstruction Overview . . . . .	76
5.2	Supercluster Reconstruction . . . . .	76
5.3	Track and Vertex Reconstruction . . . . .	78
5.4	Photon and Electron Reconstruction . . . . .	79
5.5	Muon Reconstruction . . . . .	80
5.6	Particle Flow Algorithm . . . . .	81
5.7	Jet Reconstruction . . . . .	82
5.8	Missing Transverse Energy Reconstruction . . . . .	83
5.9	Anomalous Signals . . . . .	84

<b>6 Search Analysis for Long-Lived Neutral Particles</b>	<b>86</b>
6.1 Analysis Strategy . . . . .	86
6.1.1 Signal and Background Events . . . . .	86
6.1.2 Samples . . . . .	87
6.2 ECAL Timing . . . . .	89
6.2.1 Photon Time Measurement for this Analysis . . . . .	89
6.2.2 Satellite Bunches . . . . .	92
6.2.3 $E_T^{\text{miss}}$ Adjustments . . . . .	93
6.3 Event Selection . . . . .	94
6.3.1 Trigger Selection . . . . .	94
6.3.2 Offline Selection . . . . .	96
6.4 Background Estimation . . . . .	100
6.4.1 Collision Background . . . . .	101
6.4.2 Non-Collision Background . . . . .	102
6.4.3 Event Vetoing . . . . .	107
6.4.4 Background Estimation with ABDC Method . . . . .	110
6.4.5 Background Estimation Cross Check . . . . .	114
6.5 Results . . . . .	120
<b>7 Limit Setting and Interpretation</b>	<b>122</b>
7.1 Exclusion Limit Setting . . . . .	122
7.1.1 $CL_S$ Method to Determine Exclusion Limits . . . . .	123
7.1.2 Uncertainty Studies . . . . .	124
7.1.3 The HIGGS COMBINE Tool for Evaluating Upper Limits . . . . .	126
7.2 Limit Interpretation in the SPS8 Benchmark GMSB Model . . . . .	131
7.2.1 Cross-section Upper Limits . . . . .	131
7.2.2 Mass and Lifetime Upper Limits . . . . .	133
<b>8 Conclusion</b>	<b>139</b>
<b>Bibliography</b>	<b>140</b>

<b>Appendix A. Glossary and Acronyms</b>	<b>145</b>
A.1 Glossary . . . . .	145
A.2 Acronyms . . . . .	146
A.3 Analysis How To and Data Samples . . . . .	147
A.3.1 Check Out Software Packages . . . . .	147
A.3.2 Data Samples . . . . .	147

# List of Tables

2.1	Fermions of the SM. Particle symbols are explained in text. . . . .	8
2.2	Interaction mediating vector bosons in the SM and the characteristic lifetime of the interaction. . . . .	8
2.3	Particles in the MSSM. SUSY particles (sparticles) have a “~” on the symbol . . . . .	13
2.4	Gauge and mass eigenstates of SUSY particles in the Minimal Supersymmetric SM (MSSM). . . . .	13
3.1	CMS Sub-detectors performance for LHC RUN 1 [34]. . . . .	59
4.1	ECAL timing resolution absolute time and single precision for 2011 and 2012 of LHC Run 1. . . . .	75
6.1	Signal GMSB SPS8 Monte Carlo samples for different $\Delta$ with $50\text{ cm} < c\tau < 1000\text{ cm}$ and Branching Ratios (BR). . . . .	88
6.2	The $\gamma +$ jets samples for $\hat{p}_T$ from $50\text{ GeV}/c$ to $800\text{ GeV}/c$ . . . . .	89
6.3	The photon identification and selection criteria used in this analysis . .	99
6.4	The Jet ID and MET selection used in this analysis . . . . .	99
6.5	Summary of missing transverse expectation for events with out-of-time photons. . . . .	109
6.6	Definition of ABCD regions used for estimating non-collision background events in the signal region D. Events must satisfy the $\cancel{E}_T^{\gamma} > 60\text{ GeV}$ selection requirement, which reduces collision background events significantly. .	110
6.7	A,B,C,D,E,F regions used for estimating collision background events with out-of-time photons contamination the regions B and D of Table 6.6. Here, events must satisfy $\cancel{E}_T > 60\text{ GeV}$ , selection requirement. . . . .	112

6.8	Event yields used in validating the ABCD background estimation method using 0 and 1-jet events sample. Halo/cosmic/spikes yields are obtained from tagged events. All events must pass photon, jet and $E_T^{\text{miss}}$ selection requirements. . . . .	113
6.9	Number of Z boson events with di-electron invariant mass, $76 < m_{e^+e^-} < 100 \text{ GeV}/c^2$ ) in the in-time and out-of-time Z boson samples. . . . .	117
6.10	Event yields used in our final background estimation for signal candidate events whose final state consist of at least one photon, at least two jets, $\cancel{E}_T^{\gamma} > 60 \text{ GeV}$ and $\cancel{E}_T > 60 \text{ GeV}$ . . . . .	121
7.1	Summary of systematic uncertainties for signal efficiency and background estimation in this analysis and applied to our final results. . . . .	125
A.1	Acronyms . . . . .	147
A.2	Data samples and their corresponding integrated luminosity totaling $19.1 \text{ fb}^{-1}$ used in the our delayed photon search analysis . . . . .	148

# List of Figures

2.1	Higgs boson ‘‘Mexican hat’’ potential, $V(\phi^*\phi) = \mu^2(\phi^*\phi) + \lambda(\phi^*\phi)^2$ , which leads to spontaneous symmetry breaking with choice of parameters $\mu^2 < 0$ , $\lambda > 0$ . . . . .	7
2.2	Fermions and bosons and their interactions in the SM. The bosons (except the Higgs boson) mediate the interactions between fermions. . . . .	7
2.3	Higgs mass contributions arising from the Higgs field coupling to fermions (a) and scalar (b) fields. . . . .	10
2.4	Cross section for producing sparticles with different mass and in different type of interaction at the LHC. More higher mass sparticles are produced through strong interaction, $pp \rightarrow \tilde{g}\tilde{g}$ , than the others, $pp \rightarrow \tilde{\chi}^\pm\tilde{\chi}^\mp, \tilde{\chi}^0\tilde{\chi}^\pm$	16
2.5	Feynman diagrams of <i>Gravitino-Gaugino-Gauge boson</i> ( $\tilde{G}, \lambda, A$ ) ( <i>left</i> ) and <i>Gravitino-Scalar-Chiral fermion</i> ( $\tilde{G}, \phi, \psi$ ) ( <i>right</i> ) couplings. The coupling strength goes like $\frac{1}{\sqrt{F}}$ . . . . .	20
2.6	Sparticle mass spectra for SPS8 benchmark model: $\Lambda = 100$ TeV (left) and $\Lambda = 180$ TeV (right) with $C_{grav} = 93.5$ . The sparticle mass increases with $\Lambda$ . . . . .	24
2.7	Feynman diagrams for lightest neutralino ( $\tilde{\chi}_1^0$ ) production from the cascade decay of a pair of gluinos ( <i>top</i> ) and squarks ( <i>bottom</i> ). The final state can either have a single ( <i>left diagrams</i> ) or double photons ( <i>right diagrams</i> ). . . . .	25

2.8	Number of photons with photon $p_T > 50 \text{ GeV}/c$ (top left), number of jets (top right) and $E_T^{\text{miss}}$ (bottom) for events with $\tilde{\chi}_1^0$ decay to $\gamma$ and $\tilde{G}$ for different lifetimes $\tau = 6.7 \text{ ns}, 13.3 \text{ ns}, 20.0 \text{ ns}$ and $\Lambda = 180 \text{ TeV}$ of the SPS8 benchmark GMSB model. A $\gamma+\text{jet}$ with $120 < p_T^\gamma < 170 \text{ GeV}/c$ sample shown for comparison with the signal samples. . . . .	28
2.9	Neutralino transverse momentum ( $p_T^{\tilde{\chi}_1^0}$ ) distribution (top left) and transverse distance traveled (top right). Transverse momentum (bottom left) and time (bottom right) of photon from neutralino decay for different $\Lambda$ and $c\tau$ points. . . . .	30
2.10	Schematic diagram ( <i>left</i> ) of $\tilde{\chi}_1^0 \rightarrow \gamma + \tilde{G}$ decay topology within the ECAL volume of the CMS detector. The estimated photon arrival time ( <i>right</i> ) at ECAL from the decay of $\tilde{\chi}_1^0$ in the SPS8 benchmark GMSB model with $m_{\tilde{\chi}_1^0} = 256 \text{ GeV}/c^2$ and $\tau = 20 \text{ ns}$ . . . . .	32
2.11	Neutralino lifetime and mass upper limit from ATLAS (left) and CMS (7 TeV), DØ and CDF experiments (right) from the search for events with delayed or non-pointing photons. . . . .	34
3.1	Schematic diagram showing the full Large hadron Collider. . . . .	36
3.2	Cumulative luminosity versus month delivered (blue) by the LHC and recorded (orange) by CMS detector during stable beams of $pp$ collisions at $\sqrt{S} = 8 \text{ TeV}$ in 2012. . . . .	38
3.3	Longitudinal profile of a typical LHC proton beam taken with the Longitudinal Density Monitor (LDM) detector. Ghost/Satellite bunches and the main proton bunch shown. . . . .	40
3.4	Left: Arrival time (red) of events in ATLAS for LHC fill 1533 during 2010 $PbPb$ collision and an LDM profile (black) for Beam2 (same for Beam1). Right: Cluster time in the CMS endcap calorimeters from fill 1089 of the positive endcap detector(left side of IP $z > 0$ ) (left) and negative endcap detector(right side of IP, $z < 0$ ) (right). Both plots show a clear presence of events from Ghost/Satellite bunches with the expected time separation. . . . .	40
3.5	Schematic diagram of CMS calorimetry system with HCAL enclosing ECAL in the barrel and endcap regions. . . . .	42
3.6	CMS Detector showing the different subdetectors and their material. . .	43

3.7	CMS detector schematic view with definition of $x - y - z$ coordinates. . . . .	43
3.8	Layout of the CMS electromagnetic calorimeter showing the arrangement of crystal modules, supermodules in the barrel with the preshower in front of endcap with supercrystals. . . . .	47
3.9	Schematic diagram of the ECAL electronics readout Trigger Tower (TT) or Front End (FE) board. . . . .	51
3.10	Schematic diagram of the ECAL electronics readout for a single crystal. . . . .	51
3.11	Schematic diagram of the ECAL Off-Detector and Readout Architecture. . . . .	52
3.12	Cross section view showing the coverage range of CMS sub-detectors and their longitudinal distance from the IP. . . . .	58
3.13	Level-1 Trigger Architecture of CMS. . . . .	58
4.1	(a) A measured ECAL pulse shape for a single channel. (b) $\mathbf{T} - \mathbf{T}_{\max}$ Vs $R(T)$ relationship whose inverse is $T(R)$ . Solid line is pulse shape from test beam while dots are typical 10 discrete samples corresponding to signal from proton-proton collision. . . . .	61
4.2	Difference in the time measurements as a function of $A_{eff}/\sigma_n$ of two crystals sharing an energy and belonging to the same electromagnetic shower obtained during electron test beam measurements. The single crystal energy scales for barrel (EB) and endcap (EE) is overlaid. The fitted results give $N = (35.1 \pm 0.2)$ ns and $\bar{C} = (20 \pm 4)$ ns. . . . .	64
4.3	Timing maps showing the distribution of average (mean) time for each PbWO <sub>4</sub> crystal in EB (top) and EE (below: EE-(left), EE+(right)) before crystal synchronization. . . . .	67
4.4	Timing maps showing the distribution of average time of each crystal after synchronization with most crystals having an average time of zero indicating the success of the crystal synchronization process and validity of the time constants. . . . .	68
4.5	Average time ( $\mu$ ) against rechit energy for EB. The first gain transitions (gain-12 to 6) happens at about 130 GeV and time bias on energy is seen in CMSSW44X (left) and very little in CMSSW53X (right) where the corrections have been applied during rechit reconstruction. . . . .	71

4.6	The standard deviation against rechit energy for EB in CMSSW44X (left) and CMSSW53X (right). The time bias corrections don't affect the standard deviation on the time. . . . .	71
4.7	Time difference between the two reconstructed electrons in $Z \rightarrow e^-e^+$ decay. The electron time is the seed (crystal with highest energy deposit) time with additional correction due to the time of flight of the electron in EB and EE. . . . .	73
4.8	Absolute time of a single reconstructed electron in $Z \rightarrow e^-e^+$ decay. The electron time is the seed (crystal with highest energy deposit) time of the electron in EB and EE. . . . .	73
4.9	Timing resolution from: <i>left</i> : Two most energetic crystals in the same FE electronics, <i>right</i> : Two most energetic crystals belonging to different FE electronics, as a function of effective amplitude( $A_{eff} = A_1 A_2 / \sqrt{A_1^2 + A_2^2}$ ) normalized to noise in EB. Both crystals are from reconstructed electrons in $Z \rightarrow e^-e^+$ events. . . . .	74
5.1	Superclustering algorithm direction (left) in the $(\eta, \phi)$ plane in EB and fraction (right) of electromagnetic shower energy coverage in a crystal energy matrix. . . . .	77
5.2	Illustration of muons from proton-proton collision, cosmic rays and beam halo. (a) Muons from collision propagating from the center and moving outwards, (b) Cosmic muons traveling through the detector leaving signals in opposite hemispheres of the muon system, (c) Cosmic muons leaving signals in the tracker and opposite hemispheres, (d) cosmic muons entering and leaving the detector without passing through the muon detector layers, (e) beam halo muons penetrating the detector and leaving signals in the endcaps and (f) Cosmic muons entering the detector through the endcap (EE) and leaving through the barrel (EB). This can happen in the reverse way; EB to EE. . . . .	81
6.1	Seed (black) and Average (blue) times as the measured photon time. . .	90
6.2	$\chi^2$ against photon time distribution. Spikes misidentified as photons have very large $\chi^2$ and negative time particularly the region where $\chi^2 > 4$ and $t < -4$ ns. . . . .	91

6.3	Time distributions of in-time photons from $\gamma+$ jets MC (blue) and data (red) samples before (left) and after (right) we adjusted the MC photon time. . . . .	92
6.4	Time distribution of photons in barrel ( <b>EB</b> ), endcap ( <b>EE</b> ) and all of ECAL ( <b>ALL ECAL</b> ) with $p_T > 50 \text{ GeV}$ from data. A 2.5 ns delay timing pattern is observed in ECAL with clarity in EE. . . . .	93
6.5	Our HLT trigger efficiency turn-on curves in event $\cancel{E}_T$ (left) and photon $p_T$ (right). The $\gamma+$ jets samples require photon $p_T > 170 \text{ GeV}/c$ . . . . .	96
6.6	Comparing ECAL time distribution of events with different jet multiplicity from small sample of data and a single GMSB $\Lambda = 180 \text{ TeV}$ and $c\tau = 6000 \text{ mm}$ sample. Accepted photons must have $p_T > 60 \text{ GeV}$ and belong to barrel and encap. . . . .	98
6.7	ECAL time against $\eta$ (left) and ECAL time against $\phi$ (right) for photons with $p_T > 60 \text{ GeV}$ from data. . . . .	100
6.8	ECAL time <i>vs</i> $\Delta\phi(\text{CSC Seg}, \gamma)$ (left) for in time (black) and out-of-time (red and blue) photons. Photon ECAL time $V.s \eta$ (right), expected halo-induced photon time is shown as two red lines. . . . .	104
6.9	Scatter plot showing $\Delta\eta(\text{DT Seg}, \gamma)$ against $\Delta\phi(\text{DT Seg}, \gamma)$ for out-of-time ( $t_\gamma > 2 \text{ ns}$ and $t_\gamma < -3 \text{ ns}$ ) photons (right) compared to in-time ( $ t_\gamma  < 1 \text{ ns}$ ) photons (left). Cosmic photon candidates have small $\Delta\eta$ and $\Delta\phi$ . . . . .	105
6.10	Scatter plot of $\Delta\eta(\text{DT Seg}, \gamma)$ against $\Delta\phi(\text{DT Seg}, \gamma)$ for photons from pure cosmic muon data. Small $\Delta\eta$ and $\Delta\phi$ are cosmic photons. . . . .	105
6.11	<i>Number of crystals</i> belonging to a photon supercluster (left) plot for in-time photon candidates (black), spike-seeded photon candidates (magenta) and halo-induced photon candidates (red). The spike-seeded photon candidates are selected using a swiss-cross variable $(1-E_4/E_1)$ (right), shown comparing in-time photons ( $ t_\gamma  < 1.0$ ) to spike candidate sample selected using $S_{Minor}$ . . . . .	107
6.12	Photon ECAL time, for a data sample of 0 and 1-jet events, showing our tagging performance for non-collision background events. . . . .	108

6.13	Di-electron mass distribution (left) and the time (right) of the two electron candidates for the signal, $76 < m_{e^+e^-} < 100 \text{ GeV}/c^2$ , of Z boson sample. Events are from the <b>Single/DoubleElectron</b> data sample. . . . .	115
6.14	ECAL time $V s \eta$ (top plots) and $V s \phi$ (bottom plots) for electromagnetic particle candidates from <b>SinglePhoton</b> data sample (left) compared to electromagnetic particle candidates from the <b>Single/DoubleElectron</b> data sample (right). All electromagnetic particle candidates are in barrel. Most of the electromagnetic particles with “cross-shape” and at $\phi = 0, \pm\pi$ , are halo-induced photons. . . . .	116
6.15	Di-electron invariant mass and polynomial fit (red) for sideband sample ( $50 < m_{e^+e^-} < 76 \text{ GeV}/c^2$ and $100 < m_{e^+e^-} < 130 \text{ GeV}/c^2$ ). Di-electron invariant mass and polynomial fit (blue) for in-time ( $ t  < 2 \text{ ns}$ ) Z candidates ( <i>top right</i> ). Di-electron invariant mass and polynomial fit for out-of-time ( $t < -3 \text{ ns}$ ) Z candidates ( <i>bottom left</i> ). Di-electron invariant mass and polynomial fit for out-of-time ( $t > 3 \text{ ns}$ ) Z candidates ( <i>bottom right</i> ). The fits are used to estimated the number of true Z bosons in the int-time and out-of-time Z candidate samples. . . . .	119
7.1	The efficiency for different mean decay length, $c\tau$ [ mm ] with $\Lambda = 180 \text{ TeV}$ . TACC/ALL (yellow square markers) is the Efficiency $\times$ Acceptance( $t > 3 \text{ ns}$ ) i.e. $\varepsilon \times A$ , used in evaluating the exclusion limits. The TACC/ALL is magnified by factor $\times 10$ for display purpose. . . . .	132
7.2	$95\% CL_S$ CL on the lightest neutralino production cross-section times branching ratio ( $\sigma \times BR$ )[ pb ] against mean lifetime[ ns ] for $\Lambda = 180 \text{ TeV}$ in the SPS8 benchmark GMSB model. . . . .	135
7.3	$95\% CL_S$ CL on the lightest neutralino production cross-section times branching ratio ( $\sigma \times BR$ ) for different $\Lambda$ (or mass of lightest neutralino) for $\tau = 6.7 \text{ ns}$ ( $c\tau = 2000 \text{ mm}$ ) in the SPS8 benchmark GMSB model. . . . .	136
7.4	$95\% CL$ exclusion limit in lightest neutralino mass (or $\Lambda$ ) against mean lifetime in SPS8 benchmark GMSB model. Limits from previous experiments also shown. . . . .	137



# Chapter 1

## Introduction

We present in this thesis the results of a search for Long-Lived Neutral Particles (LLNPs) produced in proton-proton ( $pp$ ) collisions at  $\sqrt{S} = 8 \text{ TeV}$  by the Large Hadron Collider (LHC) on data recorded using the Compact Muon Solenoid (CMS) detector.

The Standard Model (SM) describes the interactions of fundamental particles with unmatched precision and has been very successful in terms of all its predictions of new particles and their properties agreeing with experiments. However, there are strong indications that the SM is incomplete. For example, the SM does not include gravity in its formulation and describes only visible matter, which is about 5 times less abundant than the total matter in the universe. The rest of the matter in the universe is referred to as Dark Matter (DM) [1, 2, 3], because we cannot “see” them.

There are many extensions to the SM where DM and other new phenomena are expected. LLNPs, which are not described by the SM are predicted to exist by many models generally referred to as Beyond the Standard Model (BSM) models. These LLNPs can decay into stable neutral particles which are good candidates for a DM particle and if they have low enough mass may be produced and detected at the LHC. The signatures for the decay of a LLNP include proton collisions with Missing Transverse Energy (MET), which indicates the escaping undetected candidate DM particle, and an electromagnetic particle like a photon which is detected late with respect to photons from normal LHC  $pp$  collision times, in the same event. The combination of a late photon and large MET is the central idea in the search presented in this thesis.

The LHC completed a successful first long operation in 2012. Data from  $pp$  collisions

during this period of operation (LHC RUN 1) was recorded by the CMS detector. The CMS detector was fully operational for nearly all of this period. The Electromagnetic Calorimeter (ECAL) which is a sub-detector of the CMS recorded the arrival time and energy of electromagnetic particles produced from  $pp$  collisions with excellent resolution. This resolution was maintained throughout the entire LHC RUN 1 by continuous energy and timing performance monitoring and calibration. Evidence for LLNPs is sought in these data using delayed photon and large MET in the same event. Understanding the signature of the LLNP in the CMS detector is studied using samples of events generated in a Monte Carlo simulation of the production and decay of LLNPs.

This thesis is organized as follows: A brief introduction of the Standard Model, Supersymmetry (SUSY) and the description of Gauge Mediating Supersymmetry Breaking (GMSB) models which are the benchmark models for the production of LLNPs [16] is presented in Chapters 2. In Chapter 3, the LHC and CMS particle detector are described with an emphasis on the sub-detectors used in our search for LLNPs. A description of the photon timing measurements made using the ECAL and its performance is discussed in Chapter 4, while the reconstruction of events and their constituent particles are described in Chapter 5 where the definition and measurement of quantities like MET and jets are presented. Chapter 6 describes the search method in detail including the data samples used, observable quantities, event selection requirements and background estimation techniques. The result of our search is also presented in this chapter. In Chapter 7, we describe the statistical methods used to estimate the sensitivities of the measurement. The systematic uncertainties arising from signal efficiency and acceptance in our signal event selection are also discussed in this chapter. Exclusion limits on the product of the production cross section and decay branching ratio for different lifetimes and masses of the LLNP together with the interpretation of our results in terms of possible extension of the SM by our search analysis is also discussed in this chapter and in Chapter 8 conclusions are presented.

## Chapter 2

# Phenomenology of Long-Lived Particles

### 2.1 The Standard Model

The Standard Model (SM) is a mathematical description of the fundamental components of matter and their interactions. Fermions are the building blocks of matter and their interaction is mediated by vector bosons. The SM describes the interactions of fermions through the weak, electromagnetic and strong interactions but does not describe gravity. Fermions and bosons get their mass by interacting with a scalar boson in a process called Spontaneous Gauge Symmetry Breaking [6].

#### 2.1.1 Fermions

Half-integer spin ( $\frac{1}{2}\hbar$ ) particles called *fermions* exist in nature, together with their anti-particles (particle with opposite charge), as either leptons ( $\ell$ ) or quarks ( $q$ ). Fermions come in 3 *generations* or *flavors* and are arranged in a mass hierarchy, where the third generation fermions are the heaviest. The third and second generation fermions are not stable and do decay to the first generation fermions which are stable.

Quarks carry fractional electric charges in units of the electron charge,  $e$ , and can participate in weak, electromagnetic and strong interactions since they have a *color* charge in addition to the electric charge. A quark generation consists of an “*Up-type*” and

a “*Down-type*” quark as given in Table 2.1. The *Up-type* quarks (**up** (u), **charm** (c), **top** (t)) have a charge of  $+\frac{2}{3}$ , while the *Down-type* quarks (**down** (d), **strange** (s), **bottom** (b)) have a charge of  $-\frac{1}{3}$ . The **top** quark (t) which is the heaviest SM fermion has a mass of  $m_t = 173 \text{ GeV}/c^2$  and can remain stable only for about  $10^{-24}$  seconds. Quarks do not exist as free particles in nature but remain in bound states of quarks and/or anti-quarks in the form of composite particles called *Hadrons*.

Leptons exist free in nature and also come in pairs consisting of a lepton and its corresponding neutrino. The leptons of all the 3 generations (**electron** (e), **muon** ( $\mu$ ), **tau** ( $\tau$ )) have a charge of  $-1$  in units of the electron charge,  $e$ , while their corresponding neutrinos (**electron neutrino** ( $\nu_e$ ), **muon neutrino** ( $\nu_\mu$ ), **tau neutrino** ( $\nu_\tau$ )) have no charge. Leptons can participate only in weak and electromagnetic interactions since they have no color charge. We present a summary of the fermions in each generation according to the SM in Table 2.1.

### 2.1.2 Bosons

*Bosonic* particles have integer spins which is either  $0\hbar$  for *scalar* or  $1\hbar$  for *vector* bosons. Vector bosons are responsible for mediating the interactions given in Table 2.2 between fermions and the only scalar boson (Higgs boson) discovered so far gives mass to both fermions and bosons.

The vector bosons  $W^\pm$  (charged) and  $Z$  (neutral) are massive and mediate the *weak* interactions, while the massless vector bosons: a *photon* ( $\gamma$ ) and 8 *gluons* (g) mediate the *electromagnetic* and *strong* interactions, respectively [6, 7]. The characteristic lifetimes of a particle decay through the SM interactions is presented in Table 2.2. The longest lifetimes are characteristic of the weak interactions, explained partly because the mediating vector bosons is massive or the interaction strength is weakest.

### 2.1.3 Spontaneous Symmetry Breaking

Symmetries play a central role in the SM. The weak, electromagnetic and strong interactions of the SM are described using a combination of 3 different symmetries called *gauge* symmetries. To each gauge symmetry is associated a *conserved quantum number* which

dictates the possibility of a particle interaction happening. The SM gauge symmetry is

$$SU(3)_C \otimes SU(2)_L \otimes U(1)_Y, \quad (2.1)$$

where,  $SU(3)_C$  is the gauge symmetry describing strong interactions with *color* ( $C$ ) charge as its conserved quantum quantity. Consequently, because of the color charge quarks can participate in strong interactions mediated by 8 massless gluons.

$SU(2)_L \otimes U(1)_Y$  is the gauge symmetry describing the weak and electromagnetic interactions also known as the *electro-weak* interaction and the conserved quantum number is derived from a combination of conserved quantum numbers: *isospin* ( $T_3$ ) of  $SU(2)_L$  and *hypercharge* ( $Y$ ) of  $U(1)_Y$  symmetry. After the spontaneous breaking of this electro-weak symmetry ( $SU(2)_L \otimes U(1)_Y \rightarrow U(1)_Q$ ), the resulting conserved quantum number describing the electromagnetic interaction which is based on the resulting  $U(1)_Q$  gauge symmetry is the electric charge,  $Q$ . The electric charge is expressed in units of the electron charge,  $e$ , and it is related to  $T_3$  and  $Y$  through the relation

$$Q = T_3 + \frac{Y}{2}. \quad (2.2)$$

Corresponding to the  $SU(2) \otimes U(1)$  symmetry, are 4 massless vector bosons or *eigen* states,  $W_\mu^{1,2,3}, B_\mu$ , which are capable of mixing quantum mechanically to form the physical electro-weak vector bosons or *mass* eigenstates:  $W^\pm, Z, \gamma$ . Through rotation with a rotation angle which relates the masses of the  $W^\pm$  and  $Z$  bosons, the weak isospin eigenstates are transformed into the mass eigenstates. The states, rotation angle and rotation are given as

$$W^\pm = \frac{W_\mu^1 \pm iW_\mu^2}{\sqrt{2}}, \quad \frac{m_{W^\pm}}{m_Z} = \cos \theta_w, \quad \begin{pmatrix} \gamma \\ Z \end{pmatrix} = \begin{pmatrix} \cos \theta_w & \sin \theta_w \\ -\sin \theta_w & \cos \theta_w \end{pmatrix} \begin{pmatrix} B_\mu \\ W_\mu^3 \end{pmatrix} \quad (2.3)$$

The rotation angle,  $\theta_w$ , known as the *Weinberg angle* is one of the input parameters to the SM and has been measured from experiments to be equal to 28.726 degrees.

According to the SM, the only way to explain the observed massive vector bosons and how fermions get their mass is through the *Higgs mechanism* [8], which involves

spontaneously breaking the gauge symmetry of the SM,

$$SU(3)_C \otimes SU(2)_L \otimes U(1)_Y \xrightarrow{SSB \text{ into}} SU(3)_C \otimes U(1)_Q. \quad (2.4)$$

In the SM, Spontaneous Symmetry Breaking (SSB) is realized through the potential of a spin  $0\hbar$  complex scalar field called the *Higgs field*. The Higgs field takes the representation of a weak isospin *doublet*, however, after SSB only one neutral physical real scalar field called the *Higgs Boson* is observed as the other three scalar fields called *Nambu-Goldstone bosons* are “engulfed” by the  $W^\pm$  and  $Z$  bosons to become massive. The Higgs field potential is written in terms of the Higgs field ( $\phi$ ) and its complex conjugate ( $\phi^*$ ) as  $V(\phi^*, \phi) = \mu^2(\phi^*\phi) + \lambda(\phi^*\phi)^2$ , where  $\mu$  and  $\lambda$  are real parameters. Among the many possible different configurations which can be realized for this potential, only a particular configuration represented by the choice of the parameters:  $\mu^2 < 0$  and  $\lambda > 0$ , shown in Figure 2.1, with the minimum value of the potential ( $\phi_0$ ) or the *Vacuum Expectation Value* (VEV),  $\nu$ , of the Higgs field given as  $|\phi_0| = \nu = \sqrt{\frac{-\mu^2}{\lambda}}$ , spontaneously breaks the  $SU(2)_L \otimes U(1)_Y$  gauge symmetry into the  $U(1)_Q$  gauge symmetry.

Through their interaction with the Higgs field fermions acquire mass,  $m_f$ , which is proportional to the strength of the interaction parametrized through a Yukawa coupling,  $\lambda_f$ .

The vector bosons,  $Z$ ,  $W^\pm$ , also acquire their masses,  $m_Z$  and  $m_{W^\pm}$ , respectively, by engulfing or “*eating*” the available Nambu-Goldstone bosons of the complex Higgs doublet. The masses of fermions and vector bosons as predicted by the SM are given as

$$m_f = \lambda_f \frac{\nu}{\sqrt{2}}, \quad \frac{m_{W^\pm}}{m_Z} = \frac{\frac{1}{2}\nu g}{\frac{1}{2}\nu \sqrt{g^2 + g'^2}}, \quad (2.5)$$

where  $g$  and  $g'$  are the coupling constants of the gauge symmetries  $SU(2)_L$  and  $U(1)_Y$ , respectively.

The Higgs boson and SSB are central to the SM because without SSB fermions and vector bosons would remain massless according to the SM. The Higgs boson was discovered at CERN on July 04, 2012 through its decay channels: two photons,  $H \rightarrow \gamma\gamma$ , and a pair of  $Z$  bosons,  $H \rightarrow ZZ$ , and its mass was measured to be,  $m_H = 125.36 \pm$

$0.37(stat.Unc) \pm 0.18(syst.Unc)$  GeV/ $c^2$ . Figure 2.2 shows a relational picture of how every SM particle interacts with the Higgs boson either directly or indirectly as in the case for photons and gluons. Gluons can interact with themselves because they carry the color charge but photons cannot.

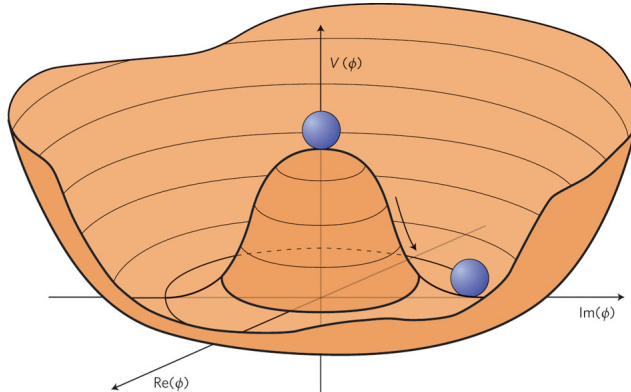


Figure 2.1: Higgs boson “Mexican hat” potential,  $V(\phi^*\phi) = \mu^2(\phi^*\phi) + \lambda(\phi^*\phi)^2$ , which leads to spontaneous symmetry breaking with choice of parameters  $\mu^2 < 0$ ,  $\lambda > 0$ .

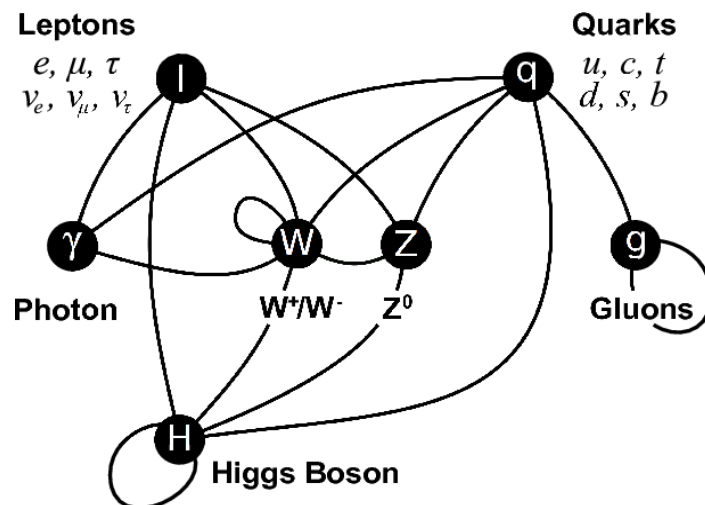


Figure 2.2: Fermions and bosons and their interactions in the SM. The bosons (except the Higgs boson) mediate the interactions between fermions.

<b>Fermions</b>	<b>Generation</b>			<b>Charge</b>
	First	Second	Third	
Leptons	$\begin{pmatrix} e^- \\ \nu_e \end{pmatrix}$	$\begin{pmatrix} \mu^- \\ \nu_\mu \end{pmatrix}$	$\begin{pmatrix} \tau^- \\ \nu_\tau \end{pmatrix}$	$\begin{pmatrix} -1 \\ 0 \end{pmatrix}$
Quarks	$\begin{pmatrix} u \\ d \end{pmatrix}$	$\begin{pmatrix} c \\ s \end{pmatrix}$	$\begin{pmatrix} t \\ b \end{pmatrix}$	$\begin{pmatrix} +\frac{2}{3} \\ -\frac{1}{3} \end{pmatrix}$

Table 2.1: Fermions of the SM. Particle symbols are explained in text.

<b>Bosons</b>	<b>Interaction</b>	<b>Symmetry</b>	<b>Characteristic Lifetime</b>
$W^\pm, Z$	Weak	$SU(2)_L \otimes U(1)_Y$	$10^{-8}$ to $10^{-13}$ seconds
$\gamma$	Electromagnetic	$U(1)_Q$	$10^{-14}$ to $10^{-20}$ seconds
$g$	Strong	$SU(3)_C$	$< 10^{-22}$ seconds

Table 2.2: Interaction mediating vector bosons in the SM and the characteristic lifetime of the interaction.

### 2.1.4 Beyond Standard Model Physics

The Higgs boson is vital in the formulation and experimental success of the SM, yet the SM itself provides no explanation for the choice of parameters ( $\mu^2 < 0$  and  $\lambda > 0$ ) of the potential of the Higgs field which spontaneously breaks the gauge symmetry or whether only one type of Higgs field exists through which all fermions couple with to get their mass. Some Beyond the Standard Model (BSM) models, like *Supersymmetry*, allow for the possibility of more than one Higgs field and predicts the existence of other particles in addition to those in the SM. The following are a few of the reasons for the interest we have developed in BSM physics, particularly Supersymmetry:

#### The Hierarchy Problem

The prediction of the mass of the Higgs boson,  $m_H^2$ , by the SM include corrections,  $\delta m_f^2$ , arising from its coupling with fermions. These corrections, at one-loop level interactions of the Higgs boson with fermions like the one given by the Feynman diagram in Figure 2.3(a), can be computed in the SM as

$$\delta m_f^2 = \frac{1}{16\pi^2} |\lambda_f|^2 \left( -2\Lambda^2 + 6m_f^2 \ln \left( \frac{\Lambda}{m_f} \right) + \dots \right), \quad (2.6)$$

where  $\lambda_f$  is the coupling strength parameter of the Higgs boson to fermions with the interaction Lagrangian density written as  $\lambda_f H \bar{f} f$ . The parameter,  $\Lambda$ , represents an arbitrary high energy scale (of the order  $10^{18}$  GeV) known as the *cut-off* energy scale. Because  $\Lambda = 10^{18}$  GeV is very large, we would expect the correction to the Higgs boson's mass to equally be very large eventually causing the Higgs boson's mass,  $m_H^2$ , to be very large. However, the Higgs boson's mass measured from experiment is only about  $125$  GeV/ $c^2$ . A dilemma thus arises, if one is to trust the SM prediction of the Higgs boson's mass then why are all these large corrections to the Higgs boson's mass not observed in experiments as they are equally predicted by the SM? This dilemma or problem is known as the *Hierarchy problem* and the SM does not provide an explanation for it.



Figure 2.3: Higgs mass contributions arising from the Higgs field coupling to fermions (a) and scalar (b) fields.

Supersymmetry (SUSY), on the other hand, provides a plausible explanation as to why these corrections are not observed in experiments. In SUSY models, there are in addition to the scalar Higgs boson new supersymmetric scalar particles, yet to be observed, which can also couple to the Higgs field as given by the one-loop interaction level Feynman diagram in Figure 2.3(b). The contributions to the Higgs boson's mass from these new scalar supersymmetric particles,  $\delta m_S^2$ , computed at the same order of one-loop as for the fermions is given as

$$\delta m_S^2 = \frac{1}{16\pi^2} |\lambda_S|^2 \left( \Lambda^2 - 2m_S^2 \ln \left( \frac{\Lambda}{m_S} \right) + \dots \right), \quad (2.7)$$

where  $\lambda_S$  is the coupling strength parameter of the Higgs field to the new scalar particle with the Lagrangian density given as:  $\lambda_S H S \bar{S}$ . An interesting observation comparing Equations 2.6 to Equation 2.7 up to the  $\Lambda^2$ -terms is that their signs are opposite. This means that these opposite signs corrections to the Higgs boson's mass can cancel each other so that their net contribution to the Higgs mass,  $m_H^2$ , is zero. This cancellation which happens at all orders of magnitude of these corrections is the reason why the mass of the Higgs boson from experiment is only about  $125 \text{ GeV}/c^2$ .

### Dark Matter and Long-Lived Particles

There is ample evidence [1] that dark matter (matter which does not interact with light) exists in the universe, and if this form of matter is made of particles, then, the lifetime of a dark matter particle must be comparable to the age of the universe. Furthermore, dark matter particles must be neutral since they do not interact with light. Such neutral stable particles are not described by the SM and so dark matter particles if they exists

should probably interact with ordinary matter in addition to gravity through a new kind of interaction.

Neutral meta-stable (particles that are stable for a long period of time and then decay) called *Long-Lived Neutral Particles* (LLNP) also not described by the SM can decay into dark matter particles through new interactions. These LLNPs are predicted by many BSM models and they have lifetimes longer than the characteristic lifetimes of particles and interactions described by the SM as given in Table 2.2. In addition to SUSY explaining the stability of the Higgs boson's mass, it also predicts the existence of LLNPs which decay into particles which are candidates for dark matter particles with lifetime beyond those in the SM [2, 3, 4, 5]. Such predictions have motivated many studies in theory and experiment of SUSY as an interesting candidate among other BSM models. The idea of experimentally finding LLNPs described by either SUSY or any other BSM model is certainly a motivation for the study presented in this thesis.

## 2.2 Supersymmetry

Supersymmetry relates space-time symmetries (rotation and translation) to gauge symmetries ( $SU(3)_C \otimes SU(2)_L \otimes U(1)_Y$ ) [10, 11]. The generators of Supersymmetry (SUSY),  $Q$ , can transform fermions into bosons and bosons into fermions as

$$Q|\text{Fermion}\rangle = |\text{Boson}\rangle, \quad Q|\text{Boson}\rangle = |\text{Fermion}\rangle, \quad (2.8)$$

and as a consequence of this transformation, fermions and their corresponding bosons have the same mass in SUSY.

### 2.2.1 The Minimal Supersymmetric Standard Model

The *Minimal Supersymmetric Standard Model* (MSSM) is an extension of the SM using only one SUSY generator,  $Q$ , in its formulation. Since the MSSM includes supersymmetric particles or *sparticles* as they are called which are partners of SM particles, the number of particles in the MSSM is obviously doubled, however, the gauge symmetries are the same as in the SM. The spin of a sparticle and its SM counterpart differ by half-integer.

In the MSSM, two complex Higgs doublets are required:  $\mathbf{H}_d = (H_1^0, H_1^-)$  and  $\mathbf{H}_u = (H_2^+, H_2^0)$ , to give mass to the Down-typed quarks (and leptons) and to the Up-typed quarks, respectively. The particles interact with a superpotential of the Higgs bosons through dimensionless Yukawa couplings to acquire their mass through spontaneous SUSY breaking. Details of the nature of these interactions and spontaneous SUSY breaking can be found in [12, 13, 14].

Bosons (fermions) in the SM have superpartners which are fermions (bosons) in SUSY as given in Tables 2.3 and 2.4 which present the particles in the MSSM. The names of sparticles are derived from their SM counterparts by adding an “*s*” in front of the SM particle name. For example, a *selectron* is the supersymmetric partner of the electron, *squarks* are the supersymmetric partners of SM quarks. Superpartners of the SM vector bosons are indicated with the suffix “-ino”, as in *wino* and *gluinos*. While the superpartners of SM fermions are scalars called *sfermions* ( $\tilde{l}$ ), like sneutrinos ( $\tilde{\nu}$ ) and squarks ( $\tilde{q}$ ), fermions like *gluinos* ( $\tilde{g}$ ) are the superpartners of the massless gluons, the

gauge bosons of the strong interaction and *Winos* and *Binos* are the fermionic superpartners of the SM vector bosons ( $W^\pm, W^0, B$ ).

The symbols of sparticles carry the “~” sign above the SM symbol to distinguish them from their SM counterparts. For example, if  $q$  is the symbol for a SM particle then its supersymmetric partner has the symbol:  $\tilde{q}$ .

Standard Model			Supersymmetry		
Particle	Symbol	Spin	Particle	Symbol	Spin
quark	$q$	$\frac{1}{2}$	squark	$\tilde{q}$	0
lepton	$\ell$	$\frac{1}{2}$	slepton	$\tilde{\ell}$	0
W bosons	$W^\pm, W^0$	1	Wino	$\tilde{W}^\pm, \tilde{W}^0$	$\frac{1}{2}$
B boson	$B$	1	Bino	$\tilde{B}$	$\frac{1}{2}$
gluon	$g$	1	gluino	$\tilde{g}$	$\frac{1}{2}$
Higgs bosons	$H (\times 4)$	0	higgsino	$\tilde{H} (\times 4)$	$\frac{1}{2}$
Graviton	$G$	2	gravitino	$\tilde{G}$	$\frac{3}{2}$

Table 2.3: Particles in the MSSM. SUSY particles (sparticles) have a “~” on the symbol

Particle Names	Gauge eigenstates	Mass eigenstates
squark	$\tilde{q}$	$\tilde{q}$
slepton	$\tilde{\ell}$	$\tilde{\ell}$
Neutralinos	$\tilde{W}^0, \tilde{B}^0, \tilde{H}_1^0, \tilde{H}_2^0$	$\tilde{\chi}_1^0, \tilde{\chi}_2^0, \tilde{\chi}_3^0, \tilde{\chi}_4^0$
Charginos	$\tilde{W}^\pm, \tilde{W}^\pm, \tilde{H}^\pm, \tilde{H}^\pm$	$\tilde{\chi}_1^\pm, \tilde{\chi}_2^\pm$
Higgs bosons	$H_1^0, H_2^0, H_1^-, H_2^+$	$h^0, H^0, A^0, H^\pm$
gluino	$\tilde{g}$	$\tilde{g}$
Gravitino	$\tilde{G}$	$\tilde{G}$

Table 2.4: Gauge and mass eigenstates of SUSY particles in the Minimal Supersymmetric SM (MSSM).

The superpartners of these Higgs bosons ( $H_1^0, H_2^0, H_1^-, H_2^+$ ) are fermions called *higgsinos* ( $\tilde{H}_1^0, \tilde{H}_1^-, \tilde{H}_2^0, \tilde{H}_2^+$ ) while the superpartners of the gauge bosons are called *gauginos* ( $\tilde{B}^0, \tilde{W}^0, \tilde{W}^-, \tilde{W}^+$ ). The neutral gauginos and higgsinos ( $\tilde{B}^0, \tilde{W}^0, \tilde{H}_1^0, \tilde{H}_2^0$ ) mix quantum mechanically to form four neutral fermions called *Neutralinos* ( $\tilde{\chi}_1^0, \tilde{\chi}_2^0, \tilde{\chi}_3^0, \tilde{\chi}_4^0$ ), and the charged gauginos and higgsinos ( $\tilde{W}^-, \tilde{W}^+, \tilde{H}_1^-, \tilde{H}_2^+$ ) mix quantum mechanically together to form four charged fermions called *Charginos* ( $\tilde{\chi}_1^\pm, \tilde{\chi}_2^\pm$ ). The masses of the neutralinos and charginos depend on the mixing parameters which include the masses of the gauginos and higgsinos and are model dependent.

## R-Parity

It is acceptable in principle in SUSY to include terms in the MSSM Lagrangian density which may not conserve quantum numbers like the *baryon* ( $B$ ) and *lepton* ( $L$ ) numbers. However, in practice a consequence of adding such terms, for example, is that these terms leads to predictions of the proton's lifetime which is much shorter than what is measured in experiments. Since there are no evidence of such phenomenons like the proton decay which violate these quantum numbers, SUSY models are constructed with the introduction of an additional matter symmetry called *R-Parity* which relates quarks to leptons through their baryon and lepton numbers. R-parity is defined as

$$R_P = (-1)^{3(B-L)+2S} \quad (2.9)$$

where  $S$  is the particle's spin. SM particles like quarks have an *even* R-parity,  $R_P = 1$ , while sparticles like squarks have *odd* parity  $R_P = -1$ .

The phenomenological consequence of R-parity conservation are the following: first, in the decay of sparticles, the lightest sparticle (LSP) have odd parity,  $R_P = -1$ , it is electrically neutral and considered to be absolutely stable. This makes the LSP a good dark matter candidate particle [2, 5]; second, every sparticle produced will eventually decay into an odd number of LSPs, third, sparticles can only be produced in pairs. These phenomenological consequences of R-parity makes *R-parity Conserving* (RPC) SUSY models very attractive for experimental studies since these models predict new particles with low enough masses which may be produced at current particle colliders like the LHC with unique experimental signatures like small missing transverse energy.

## Cross Sections, Decay Rate and Branching Ratio

### Cross Section

Cross section provides a way of counting the number of particles produced at a proton-proton ( $pp$ ) collider like the LHC. It is proportional to the probability that the proton beams will collide and interact in a certain way to produce the particle. The cross section of producing a new particle in a BSM model or supersymmetric particle (sparticle) at the LHC depends on the following: the available energy of the proton beams compared to the mass of the particle, the type of interaction or size of the couplings during collision and the flux of the proton beams, which affects the luminosity. Since the predicted masses of sparticles are higher than those of their SM counterparts, we expect very few sparticles, if any, to be produced at the LHC, and even less for higher mass sparticles. The typical cross section of producing a sparticle at the LHC is of the order of  $1 \text{ pb} = 10^{-12} \times 10^{-24} \text{ cm}^2$  or much smaller,  $1 \text{ fb} = 10^{-15} \times 10^{-24} \text{ cm}^2$  for extremely rare SUSY or BSM processes. This is very small compared to standard model processes like the production of the Z or  $W^\pm$  bosons which are of the order of a few  $nb = 10^{-9} \times 10^{-24} \text{ cm}^2$ .

Sparticles are most likely to be produced at the LHC through the process of strong interactions ( $pp \rightarrow \tilde{g}\tilde{g}, \tilde{q}\tilde{q}$ ) than through electro-weak interactions ( $pp \rightarrow \tilde{\chi}^\pm \tilde{\chi}^\mp, \tilde{\chi}^0 \tilde{\chi}^\pm$ ). This is because the cross section for strong interaction processes is larger than for electro-weak interactions. Figure 2.4, shows the cross section of producing a sparticle, on the vertical y-axis, against its mass, on the horizontal x-axis, and the number of events produced, on the z-axis. Looking at this plot, with  $20 \text{ fb}^{-1}$  of LHC integrated luminosity (luminosity relates the cross section to the numbers of events produced) of data from  $pp$  collisions at  $\sqrt{S} = 8 \text{ TeV}$ , we expect to see many events for a given sparticle mass to be produced at the LHC through strong interactions than through electro-weak interactions.

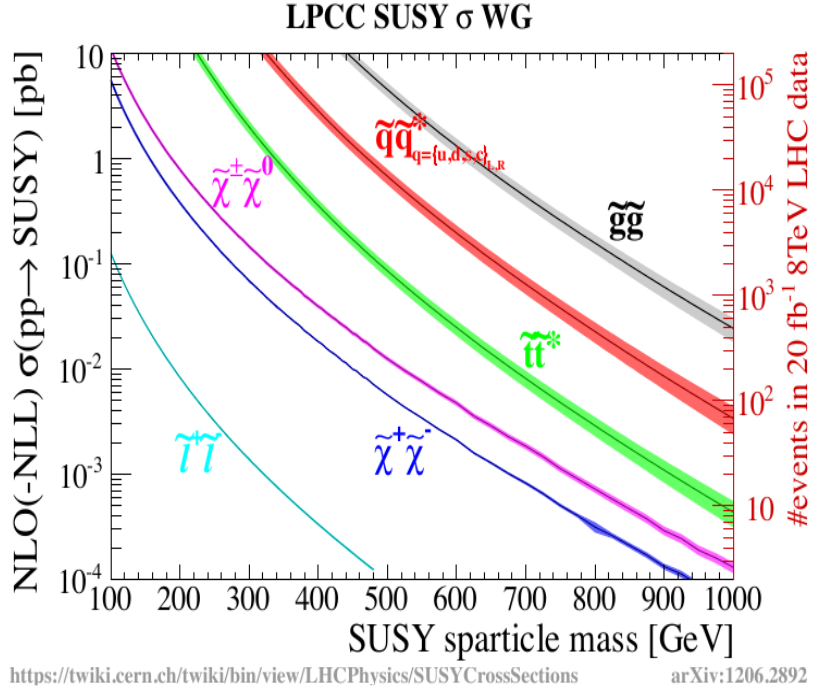


Figure 2.4: Cross section for producing sparticles with different mass and in different type of interaction at the LHC. More higher mass sparticles are produced through strong interaction,  $pp \rightarrow \tilde{g}\tilde{g}$ , than the others,  $pp \rightarrow \tilde{\chi}^\pm \tilde{\chi}^\mp, \tilde{\chi}^0 \tilde{\chi}^\pm$

### Decay Rate, Lifetime and Branching Ratio

The new particle or sparticle produced may decay either immediately or live for a while before it decays. The time it takes for the particle to stay stable after it was produced until when it finally decays is called its *lifetime*. The particle's mean lifetime ( $\tau$ ) is related to the decay rate also known as the *decay width* ( $\Gamma$ ) as

$$\tau = \frac{\hbar}{\Gamma}. \quad (2.10)$$

The decay width is proportional to the probability that the particle will decay and this probability in general depends on the coupling strength or the mass difference between the particle and its decay products or daughter particles. The type of daughter particles produced from the decay depends on the likelihood that the parent particle would decay to those daughter particles or decay through that decay channel and this likelihood is defined as the ratio of the decay rate through that channel to the total decay rate of

the parent particle through all possible decay channels. This channel “decay ratio” is known as the *Branching Ratio* (BR) for the given decay channel.

Particles with small mass differences or small couplings to their daughter particles have small decay widths and therefore live long or have long lifetimes while those with large mass differences or large couplings have large decay widths or short lifetimes. A particle may decay through SM interactions like the strong interaction in which its mean lifetime is about  $10^{-17}$  to  $10^{-25}$  seconds, electromagnetic interaction in which its mean lifetime can be between  $10^{-20}$  seconds to about  $10^{-14}$  seconds and weak interaction in which its mean lifetime varies from  $10^{-13}$  seconds to  $10^{-8}$  seconds.

The type of long-lived particles we study in this thesis are those which do not decay through any of the SM interactions and have typical mean lifetimes ranging from a few nanoseconds ( $10^{-9}$ s) to hundreds of nanoseconds.

### 2.3 Gauge Mediated Supersymmetry Breaking Models

A consequence of SUSY is that sparticles and their SM partners have the same mass. Because no sparticle have been observed with the same mass as its SM counterpart, it means SUSY is not an exact symmetry of nature and must be broken. In order to break SUSY, SUSY must first be promoted to a local symmetry since it includes gravity in its description and the local SUSY breaking should happen such that the mass of sparticles are higher than their SM partners. In any local symmetry which is realized in the broken phase, the gauge particle becomes massive by eating the Nambu-Goldstone particle, and we expect the same for spontaneously broken local SUSY. Most theoretical models favor spontaneous local SUSY breaking because it preserves renormalisability in the theory, which is a characteristic of the SM model.

Spontaneous local SUSY breaking is typically realized by introducing *soft* SUSY-breaking terms into the Lagrangian density. These soft terms ensure that those coupling constants which might lead to quadratic divergence are not introduced and the mass of the sparticles are predicted to be at about the TeV energy scale, which is accessible to present particle colliders [13, 14].

Often, the local SUSY breaking happens in the so-called *Hidden Sector* and can be mediated to the MSSM sector through interactions which do not change the flavor of the

particles called *flavor blind interactions*, e.g. gauge interactions [15]. The energy scale of the hidden sector is represented by an *order parameter*,  $\mathbf{F}$ , which is the Vacuum Expectation Value (VEV) of an auxiliary field responsible for SUSY breaking through some kind of *Super-Higgs mechanism*. The order parameter or fundamental SUSY breaking energy scale measures the magnitude of the SUSY breaking in the vacuum state.

In this super-Higgs mechanism the spin  $\frac{1}{2}$  Goldstino becomes the longitudinal component of the spin  $\frac{3}{2}$  gravitino ( $\tilde{G}$ ), the superpartner of the graviton which mediates gravitational interactions. The gravitino acquires a mass during the process which is given as

$$m_{\tilde{G}} = \frac{\mathbf{F}}{\sqrt{3}M_{Pl}} \simeq \left( \frac{\sqrt{\mathbf{F}}}{100 \text{ TeV}} \right)^2 \text{ eV}, \quad (2.11)$$

where  $M_{Pl} = 2.4 \times 10^{18} \text{ GeV}/c^2$  is the reduced Planck mass and the order parameter,  $\mathbf{F}$ , has units of [mass]<sup>2</sup>.

SUSY models in which the SUSY breaking is mediated through gauge interactions by *Messenger* particles from the hidden sector to the MSSM sector are called *Gauge Mediated Supersymmetry Breaking* (GMSB) models [16]. Depending on the GMSB model there are  $N_{mess}$  generations of messenger fields with a general SUSY mass of  $\mathbf{M}_{mess}$ . The simplest GMSB models with minimal gauge mediation assumes the messenger fields to be in the irreducible representations of dimension  $\mathbf{5} \oplus \bar{\mathbf{5}}$  of an  $SU(5)$  gauge group. The  $SU(5)$  group incorporates the SM gauge groups,  $SU(5) \supseteq SU(3)_C \otimes SU(2)_L \otimes U(1)_Y$ . The messenger field supermultiplet has scalar and fermion components which during SUSY breaking are split by an order parameter,  $F_m$ . As a consequence of this splitting gauginos in the MSSM get their mass given as

$$M_a = k_a N_{mess} \Lambda \frac{\alpha_a}{4\pi}, \quad (2.12)$$

through one-loop coupling with the messenger fields. The subscript,  $a = 1, 2, 3$ , for Bino, Wino, and gluino, respectively, with  $k_1 = \frac{5}{3}, k_2 = 1 = k_3$  and  $\alpha_a$  is the coupling strength. The effective MSSM or visible sector SUSY breaking parameter,  $\Lambda$ , relates the messenger field splitting order parameter to the messenger particle SUSY mass in the following way:

$$\Lambda = F_m / \mathbf{M}_{mess}. \quad (2.13)$$

The mass of scalars in the MSSM arise from their two-loop coupling to the messenger fields and it is given as

$$m_\phi^2 = 2N_{\text{mess}} \Lambda \left[ \frac{5}{3} \left( \frac{Y}{2} \right)^2 \left( \frac{\alpha_1}{4\pi} \right)^2 + C_2 \left( \frac{\alpha_2}{4\pi} \right)^2 + C_3 \left( \frac{\alpha_3}{4\pi} \right)^2 \right], \quad (2.14)$$

where  $Y$  is the weak hyper charge normalized to  $Q = T_3 + \frac{Y}{2}$ , same as in the SM,  $C_2 = \frac{3}{4}$  for weak isospin doublet scalars and zero for weak isospin singlets and  $C_3 = \frac{4}{3}$  for squarks and zero for other scalars.

It is possible that the fundamental SUSY breaking scale,  $\mathbf{F}$ , which determines the gravitino's mass given in Equation 2.11 is higher than the SUSY breaking scale,  $F_m$ , felt by the messenger fields. This difference is parameterized using a dimensionless parameter,  $C_{grav}$ , relating the parameters  $\mathbf{F}$  and  $F_m$  as

$$C_{grav} = \mathbf{F}/F_m. \quad (2.15)$$

If  $C_{grav} = 1$  then only one energy scale determines and fixes the masses of all the sparticles in GMSB models and the Next-To-Lightest Supersymmetric Particle (NLSP) decays instantaneously (prompt) to the Lightest-Supersymmetric Particle (LSP). If  $C_{grav} > 1$ , the mass difference between the NLSP and the LSP is no longer fixed and the decay rate may vary from prompt to non-prompt. Therefore,  $C_{grav}$  can be used to control the decay rate of the NLSP to the LSP and hence the lifetime of the NLSP from prompt to long-lived. The phenomenological consequences of GMSB models are interesting to study at experiments, for example, many GMSB models predict the existence of long-lived particles which can decay into a light gravitino which is in agreement with what is expected (order of eV) from cosmology for the mass range of dark matter particles. The light gravitino is a good candidate for dark matter since it is stable and neutral.

### 2.3.1 Long-Lived Neutral Particles in GMSB Models

GMSB models describe gravitino interactions with other particles in the same supermultiplet such as *gravitino-gaugino-gauge boson* ( $\tilde{G}, \lambda, A$ ) (left) and *gravitino-scalar-chiral fermion* ( $\tilde{G}, \phi, \psi$ ) (right) interactions shown by the Feynman diagrams in Figure 2.5. These interactions allow for a sparticle ( $\tilde{P}$ ) to decay into its SM partner ( $P$ ) and the

gravitino ( $\tilde{G}$ ). Since the interaction coupling strength is proportional to  $\frac{1}{\sqrt{\mathbf{F}}}$ , the decay rate is suppressed.

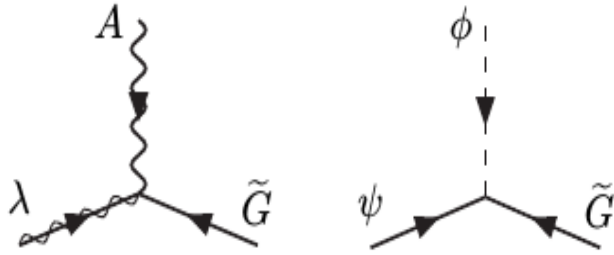


Figure 2.5: Feynman diagrams of *Gravitino-Gaugino-Gauge boson* ( $\tilde{G}, \lambda, A$ ) (left) and *Gravitino-Scalar-Chiral fermion* ( $\tilde{G}, \phi, \psi$ ) (right) couplings. The coupling strength goes like  $\frac{1}{\sqrt{\mathbf{F}}}$ .

The decay rate is given as

$$\Gamma(\tilde{P} \rightarrow P + \tilde{G}) = \kappa \frac{m_P^5}{16\pi \mathbf{F}^2} \left(1 - \frac{m_P^2}{m_{\tilde{P}}^2}\right)^2 \quad (2.16)$$

where  $\kappa$  is a mixing parameter to be evaluated for different model parameters. If  $P$  and  $\tilde{P}$  are unmixed states within the same supermultiplet, as in the decay of a slepton to a lepton and gravitino,  $\kappa = 1$ . For superpartner mass eigenstates which are a mixture of superpartners in different supermultiplets,  $\kappa < 1$  is possible, e.g. for Bino decay to photon and gravitino,  $\kappa = \cos^2 \theta_W$ . The other terms in the decay rate are due to the nature of the interaction and also from the kinematic phase space integral where the mass of the gravitino can be neglected in the computation [16, 17].

From Equation 2.16, we find that the decay width is larger for smaller values of the fundamental SUSY breaking parameter,  $\mathbf{F}$ , or equivalently for smaller masses of the gravitino since using Equation 2.11 and the relation between the fundamental SUSY breaking parameter and  $C_{grav}$ ,  $\mathbf{F} = C_{grav} \Lambda \mathbf{M}_{mess}$ , the gravitino's mass becomes,

$$m_{\tilde{G}} = C_{grav} \cdot \frac{\Lambda \mathbf{M}_{mess}}{\sqrt{3} M_{pl}}. \quad (2.17)$$

This confirms that  $C_{grav}$  is the parameter to use for controlling the gravitino's mass

and the lifetime of the NLSP and for a fixed mass of the NLSP determined by  $\Lambda$ , the decay width of the NLSP can be varied from small to large values.

In a scenario where the sparticle,  $\tilde{P}$ , is not the Next-To-Lightest Supersymmetric Particle (NLSP) the decay,  $\tilde{P} \rightarrow P + \tilde{G}$ , suffers from competition with other probably favorable decay channels and this decay process is not competitive enough to happen at a collider experiment. However, if  $\tilde{P}$  is the NLSP, then there is no competition and this decay always happens at a collider.

It is important to observe here that, if the mass of the NLSP,  $m_{NLSP}$ , is of the order of 100 GeV or more and  $\sqrt{\mathbf{F}} \ll 1000$  TeV, equivalent to saying  $m_{\tilde{G}} \leq 1$  keV, then the above decay rate is of the order that the NLSP can be observed as a long-lived particle in detectors at the large hadron collider.

### Lightest Neutralino as a Long-Lived Neutral Particle

In the scenario where the NLSP is the lightest neutralino,  $\tilde{\chi}_1^0$ , then its lifetime ( $c\tau_{\tilde{\chi}_1^0}$ ) for the decay into a photon and gravitino,  $\tilde{\chi}_1^0 \rightarrow \gamma + \tilde{G}$ , derived from Equations 2.10 and 2.16 is given as

$$c\tau_{\tilde{\chi}_1^0} \approx \left( \frac{m_{\tilde{\chi}_1^0}}{\text{GeV}} \right)^{-5} \left( \frac{\sqrt{\mathbf{F}}}{\text{TeV}} \right)^4, \quad (2.18)$$

where we have neglected  $\kappa$  as we focus on the most relevant parameters influencing the lifetime and in terms of  $C_{grav}$  the lifetime becomes,

$$c\tau_{\tilde{\chi}_1^0} \approx C_{grav}^2 \left( \frac{m_{\tilde{\chi}_1^0}}{\text{GeV}} \right)^{-5} \left( \frac{\sqrt{\Lambda \cdot \mathbf{M}_{mess}}}{\text{TeV}} \right)^4. \quad (2.19)$$

The dependence of the lifetime on the effective SUSY breaking scale,  $\Lambda$ , and  $C_{grav}$  means for a fixed mass of  $\tilde{\chi}_1^0$ ,  $m_{\tilde{\chi}_1^0}$ , given by  $\Lambda$ , we can scan the parameter space for different lifetimes of the lightest neutralino by varying  $C_{grav}$ , and for a fixed value of  $C_{grav}$ , we can also scan the parameter space for different masses of  $\tilde{\chi}_1^0$  by varying  $\Lambda$ . Therefore, using  $\Lambda$  and  $C_{grav}$  we can scan the entire parameter space for different masses and lifetimes of long-lived lightest neutralinos.

The full set of parameters which define a given GMSB model are the following:

$$\{\Lambda, \mathbf{M}_{mess}, \mathbf{N}_{mess}, \tan(\beta), sgn(\mu), C_{grav}\}, \quad (2.20)$$

with the meaning of each parameter given as follows:

- $\tan(\beta) = \frac{v_u}{v_d}$ , relates the VEVs:  $v_u$  and  $v_d$ , of the two Higgs doublets in the MSSM which are themselves not known. In most models,  $1.5 \leq \tan(\beta) \leq 60$ .
- $sgn(\mu)$  defines the sign of the Higgs and Higgsino mass parameter,  $\mu$ , which is arbitrary in their potential.  $sgn(\mu)$  appears in the neutralino and chargino mass mixing matrix.
- $N_{mess}$  is the number of messenger particles mediating SUSY breaking and also determines the masses of the MSSM sparticles with the mass of scalars proportional to  $\sqrt{N_{mess}}$ , while the masses of gauginos is linear with  $N_{mess}$ . For the lightest neutralino,  $\tilde{\chi}_1^0$ , to be the NLSP, the value of  $N_{mess}$  must be small.
- $\Lambda$  is the effective SUSY breaking energy scale at the visible sector with both the masses of the gauginos and scalars proportional to it.
- $M_{mess}$  is the mass of the messenger particles and must be lower than  $10^{16}$  GeV to allow for low energy SUSY breaking to happen in order that the gravitino is the LSP.  $M_{mess}$  must also be,  $M_{mess} > \Lambda$ , in order to avoid charge and color breaking in the messenger particle sector.

Different choices for the values of these parameters will represent different scenarios for GMSB models.

### 2.3.2 Benchmark Scenario

In this thesis we study an R-parity conserving benchmark GMSB model called the *Snowmass Point and Slopes* (SPS8) [18]. In the SPS8 benchmark GMSB model, the GMSB parameters are chosen as

$$M_{mess} = 2\Lambda, \quad \tan(\beta) = 15, \quad N_{mess} = 1, \quad (2.21)$$

while  $\Lambda$  and  $C_{grav}$  vary.

The LSP is the gravitino ( $\tilde{G}$ ) and the NLSP is the lightest neutralino ( $\tilde{\chi}_1^0$ ). The  $\tilde{\chi}_1^0$  is a mixture of the Bino ( $\tilde{B}^0$ ), Wino ( $\tilde{W}^0$ ) and higgsino ( $\tilde{H}_u^0, \tilde{H}_d^0$ ), and the decay to its

SM partner and the gravitino will depend on the choice of parameters which affect the mixing. Since the parameters:  $\Lambda$ ,  $\tan \beta$ , and  $\text{sgn}(\mu)$  affect the mixing, these parameters have been chosen in the SPS8 benchmark GMSB model to maximize the branching ratio for the decay of the  $\tilde{\chi}_1^0$  to a photon ( $\gamma$ ) and a gravitino over the other possible SM partners: Z boson,  $Z'$  and a higgs boson ( $H$ ) [17].

We study the decay of the lightest neutralino,  $\tilde{\chi}_1^0$ , as the Long-Lived Neutral Particle (LLNP), to a photon and gravitino,  $\tilde{\chi}_1^0 \rightarrow \gamma + \tilde{G}$ , in order to understand the signal of an event with a late photon and missing transverse energy in the final state. By varying  $\Lambda$  and  $C_{grav}$ , we study the production and decay of  $\tilde{\chi}_1^0$  with different masses and lifetimes.

### Supersymmetric Particle Mass Spectra

The effective SUSY breaking energy scale parameter,  $\Lambda$ , determines the masses of all sparticles in the MSSM and the mass of each sparticle increases with  $\Lambda$ . The sparticle mass spectra are shown in Figure 2.6 for  $\Lambda = 100$  TeV (left plot) and  $\Lambda = 180$  TeV (right plot) for the same values of  $C_{grav} = 93.5$  computed according to the SPS8 benchmark GMSB model. As shown in these Figures, the masses of the sparticles, including the mass of  $\tilde{\chi}_1^0$  is larger for  $\Lambda = 180$  TeV ( $m_{\tilde{\chi}_1^0} = 256 \text{ GeV}/c^2$ ) (right plot) than for  $\Lambda = 100$  TeV ( $m_{\tilde{\chi}_1^0} = 140 \text{ GeV}/c^2$ ) (left plot). This means that in order to expand our search towards heavier lightest neutralinos we must scan larger values of  $\Lambda$ .

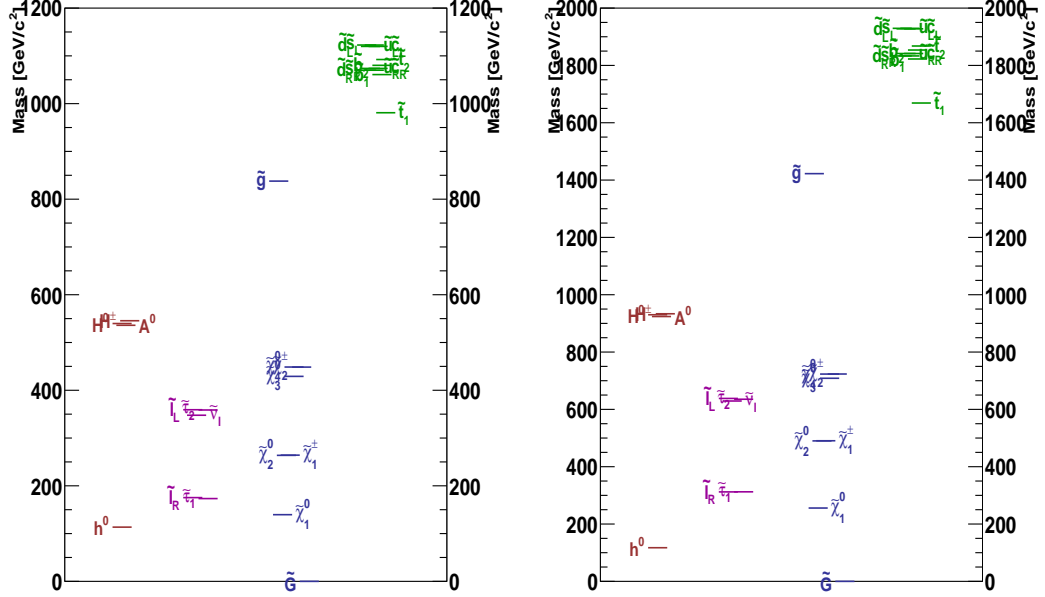


Figure 2.6: Sparticle mass spectra for SPS8 benchmark model:  $\Lambda = 100 \text{ TeV}$  (left) and  $\Lambda = 180 \text{ TeV}$  (right) with  $C_{grav} = 93.5$ . The sparticle mass increases with  $\Lambda$

### 2.3.3 Signal Modeling

We are interested in the production of the lightest neutralino,  $\tilde{\chi}_1^0$ , in strong interaction processes like  $pp \rightarrow \tilde{g}\tilde{g}, \tilde{q}\tilde{q}$ , since these processes have the highest production cross section at the LHC. The  $\tilde{\chi}_1^0$  is produced indirectly as a decay product from the *cascade decay* of massive sparticles like squarks ( $\tilde{q}$ ), excited squarks ( $\tilde{q}^*$ ) and gluinos ( $\tilde{g}$ ). The Feynman diagrams in Figure 2.7 represent the different production and decay channels of  $\tilde{\chi}_1^0$  through the cascade decay of gluinos and squarks. The final state can either have two photons (right Feynman diagrams) and two gravitinos if both  $\tilde{\chi}_1^0$  decay to a photon and a gravitino or a single photon (left Feynman diagrams) if only one  $\tilde{\chi}_1^0$  decay to a photon and gravitino. The signal events must contain at least a single photon which is late relative to normal photons produced directly from nominal LHC  $pp$  collisions and large Missing Transverse Energy ( $E_T^{\text{miss}}$ ) in the final state. The  $E_T^{\text{miss}}$  is due to the undetected gravitinos.

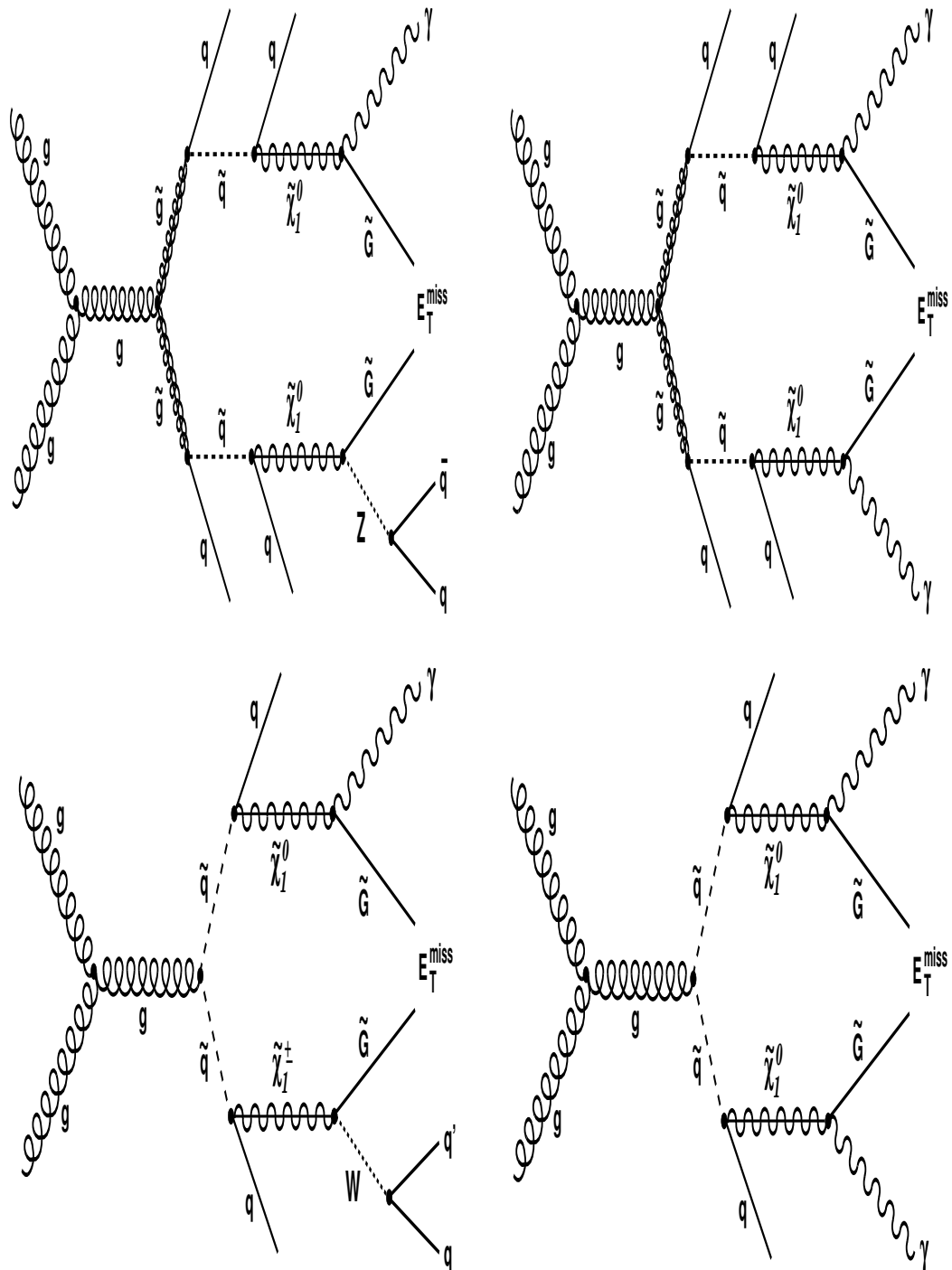


Figure 2.7: Feynman diagrams for lightest neutralino ( $\tilde{\chi}_1^0$ ) production from the cascade decay of a pair of gluinos (top) and squarks (bottom). The final state can either have a single (left diagrams) or double photons (right diagrams).

We generate high-energy-physics signal events as might be produced during  $pp$  collisions at the LHC with a center of mass energy,  $\sqrt{S} = 8$  TeV, using a general-purpose event generator called PYTHIA-6 [20]. The PYTHIA-6 software program is based on Monte Carlo (MC) methods of numerical computations and takes as input a file containing the masses, interaction couplings, decay widths and all possible decay channels and Branching Ratio ( $BR$ ) of every sparticle. This input file is called a *SUSY Les Houches Accord* (SLHA) file and it is the output of a sparticle production and decay simulation software program called ISASUSY [21]. In our case, the sparticle properties in each SLHA file have been produced according to the following choice of parameters of the SPS8 benchmark GMSB model:  $sgn(\mu) = 1$ ,  $\tan(\beta) = 15$ ,  $N_{mess} = 1$ ,  $M_{mess} = 2\Lambda$ , with  $C_{grav}$  and  $\Lambda$  chosen such that the signal event sample has events with a particular lightest neutralino mean lifetime ( $c\tau$ ) and mass. The decay of the sparticles including the  $\tilde{\chi}_1^0$  is simulated using HDECAY, a software program which is part of ISASUSY. We used HDECAY to simulate the decay of the sparticles according to our SPS8 benchmark GMSB model.

The events were generated according to the processes described by the Feynmann diagrams in Figure 2.7 with the  $\tilde{\chi}_1^0$  produced in the cascade decay of either a gluino or squark as:

$$p + p \rightarrow \tilde{g}\tilde{g}, \tilde{q}\tilde{q} \rightarrow [1 \text{ or } 2 \text{ cascade decays}] \rightarrow 2\tilde{\chi}_1^0 + \text{jets} \rightarrow 2\gamma + 2\tilde{G} + \text{jets}. \quad (2.22)$$

The  $\tilde{\chi}_1^0$  decays to either  $\gamma$ ,  $Z$ ,  $H$ ,  $e^+e^-$ , and the  $\tilde{G}$ . The dominant mode of decay is  $\tilde{\chi}_1^0 \rightarrow \gamma + \tilde{G}$  with a decay branching fraction ranging from 83 to 94%.

The interaction of the sparticles with the CMS detector is simulated using the particle-interaction-with-detector-simulation software program called GEANT4 [22]. A full physics event represented as the four vectors of a particle's momentum and position can be reconstructed from the energy deposits (hits) in the CMS detector using the CMS event reconstruction Software (CMSSW). To minimize any disagreement between MC and real  $pp$  collision data, we use the same CMSSW release version (**CMSSW\_5\_3\_29**) with the same detector conditions as the recorded data in the MC event reconstruction.

We perform some sanity checks to ensure that the signal MC samples have been correctly generated by PYTHIA-6 by analyzing the events in terms of the number of

photons,  $E_T^{\text{miss}}$  and the number of jets in each event. The mean lifetime of the  $\tilde{\chi}_1^0$  is obtained from fitting the distribution of the lifetime of each  $\tilde{\chi}_1^0$  computed using the transverse distance traveled by the  $\tilde{\chi}_1^0$  before it decay. This distance is computed using its production and decay vertex points. An agreement between the mean lifetime,  $c\tau$ , from the fit and the input lifetime value that was used in the event generation process is used to validate each generated sample.

After analyzing the MC samples we find that 97 to 99% of all our generated events have at least a single photon (left top plot) and at least 2 jets (right top plot) shown in Figure 2.9 which is what we would expect. Comparing different signal samples with  $c\tau = 2000 \text{ mm}, 4000 \text{ mm}, 6000 \text{ mm}$  (or  $\tau = 6.7 \text{ ns}, 13.3 \text{ ns}, 20 \text{ ns}$ ) of  $\Lambda = 180 \text{ TeV}$  and a  $\gamma +$  jet with  $120 < p_T^{\gamma} < 170 \text{ GeV}/c$  sample, we find that the  $E_T^{\text{miss}}$  (shown in the bottom plot of the same figure) from signal events was larger than the  $E_T^{\text{miss}}$  of events from the  $\gamma +$  jet sample which agrees with our expectation which is that the  $\gamma +$  jet sample has mostly false  $E_T^{\text{miss}}$  while signal events have large  $E_T^{\text{miss}}$  due to the undetected gravitino.

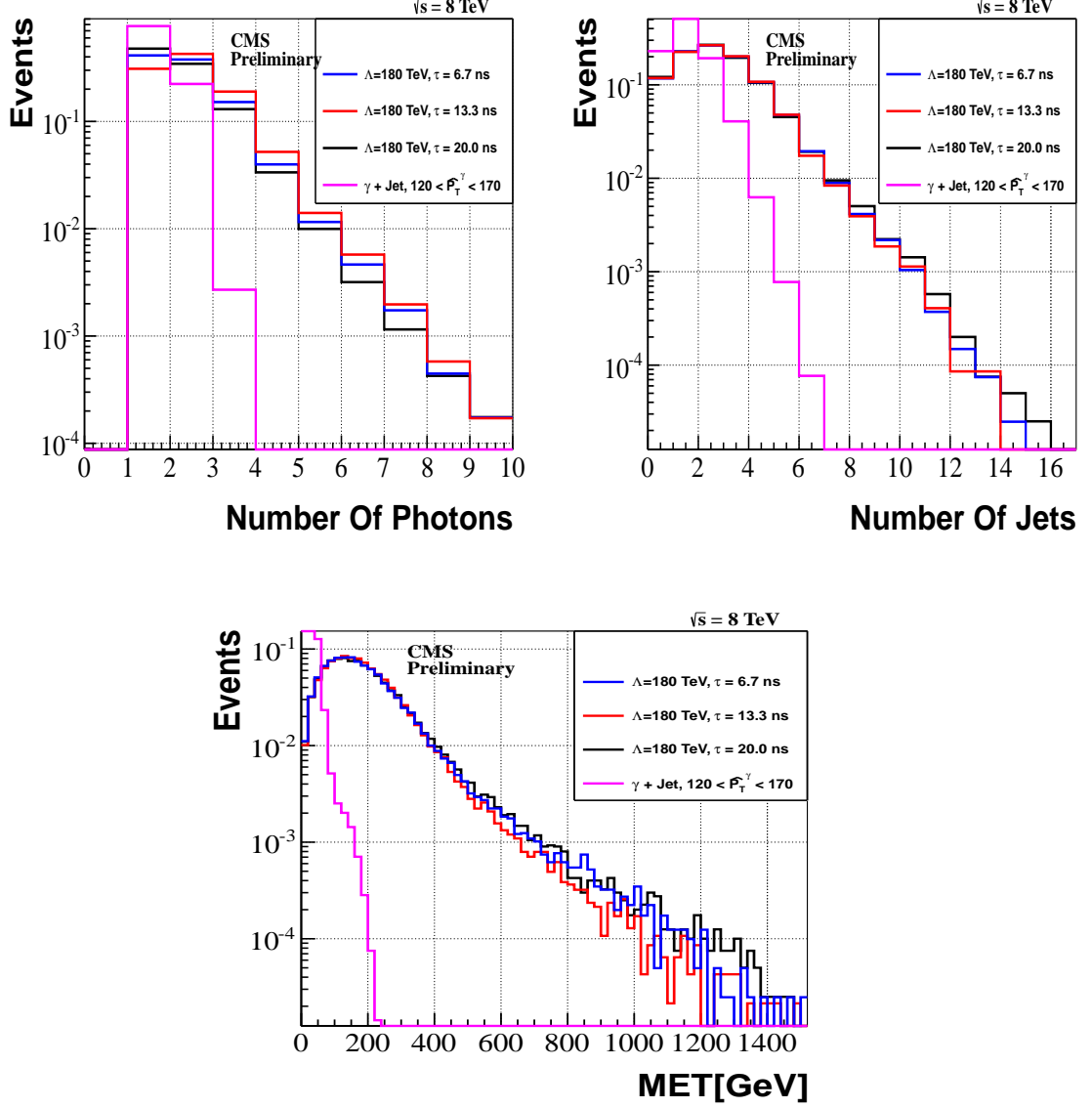


Figure 2.8: Number of photons with photon  $p_T > 50 \text{ GeV}/c$  (top left), number of jets (top right) and  $E_T^{\text{miss}}$  (bottom) for events with  $\tilde{\chi}_1^0$  decay to  $\gamma$  and  $\tilde{G}$  for different lifetimes  $\tau = 6.7 \text{ ns}, 13.3 \text{ ns}, 20.0 \text{ ns}$  and  $\Lambda = 180 \text{ TeV}$  of the SPS8 benchmark GMSB model. A  $\gamma + \text{jet}$  with  $120 < \hat{p}_T < 170 \text{ GeV}/c$  sample shown for comparison with the signal samples.

### 2.3.4 Lifetime of the Lightest Neutralino

The probability for a lightest neutralino ( $\tilde{\chi}_1^0$ ) with mass,  $m_{\tilde{\chi}_1^0}$ , produced with energy,  $E_{\tilde{\chi}_1^0}$ , to travel a distance less than  $x$  in the laboratory frame before it decays is  $\mathcal{P}(x) = 1 - \exp\left(-\frac{x}{L}\right)$ , where  $L$  is given as

$$L = \left(c\tau_{\tilde{\chi}_1^0}\right) \cdot (\gamma\beta) = \left(c\tau_{\tilde{\chi}_1^0}\right) \cdot \left(\frac{p}{m_{\tilde{\chi}_1^0}}\right). \quad (2.23)$$

The distance traveled in the CMS detector by the  $\tilde{\chi}_1^0$  before it decays depends on two main factors: the boost factor,  $(\beta\gamma)_{\tilde{\chi}_1^0} = \frac{|\vec{p}_{\tilde{\chi}_1^0}|}{m_{\tilde{\chi}_1^0}} = \sqrt{\left(\frac{E_{\tilde{\chi}_1^0}}{m_{\tilde{\chi}_1^0}}\right)^2 - 1}$ , which indicates how fast the neutralino is traveling before it decays and the inherent lifetime,  $c\tau_{\tilde{\chi}_1^0}$ , of the  $\tilde{\chi}_1^0$ . Slow moving  $\tilde{\chi}_1^0$  have  $(\beta\gamma)_{\tilde{\chi}_1^0} \ll 1$ . Both factors determine the sensitivity of the ECAL to detect late photons from the decay of  $\tilde{\chi}_1^0$ .

First, large values of  $c\tau_{\tilde{\chi}_1^0}$  means the distance traveled by  $\tilde{\chi}_1^0$  is large and if larger than the ECAL radius which is about 1.3 m, i.e. the  $\tilde{\chi}_1^0$  traveled outside the ECAL volume before it decays, then detecting the delayed photon is no longer possible and this results to a loss in sensitivity by the ECAL. On the other end, small values of  $c\tau_{\tilde{\chi}_1^0}$ ,  $c\tau_{\tilde{\chi}_1^0} < 10$  cm, means the  $\tilde{\chi}_1^0$  decays early and the photon is not late enough such that its detection using only ECAL timing measurements is not reliable and this once again results to loss in sensitivity by ECAL.

Second, lightest neutralinos ( $\tilde{\chi}_1^0$ s) produced with small momentum( $p$ ) are less boosted and travel slow enough for their decay to happen inside the ECAL volume and the delayed photon is detectable using ECAL timing measurements which results to gain in sensitivity by ECAL. On the other hand,  $\tilde{\chi}_1^0$ s produced with large momentum( $p$ ) are highly boosted and travel out of the ECAL volume before they decay. Photons from such decays are not detectable and this also results to loss in sensitivity. In Figure 2.9, we show a distribution of the momentum of the  $\tilde{\chi}_1^0$  in the transverse ( $x - y$ ) plane (transverse momentum ( $p_T^{\tilde{\chi}_1^0}$ )), the transverse distance traveled by  $\tilde{\chi}_1^0$  before it decays, the transverse momentum of the photon ( $p_T^\gamma$ ) and photon's estimated time ( $T_\gamma$ ) using only the event generator level information.

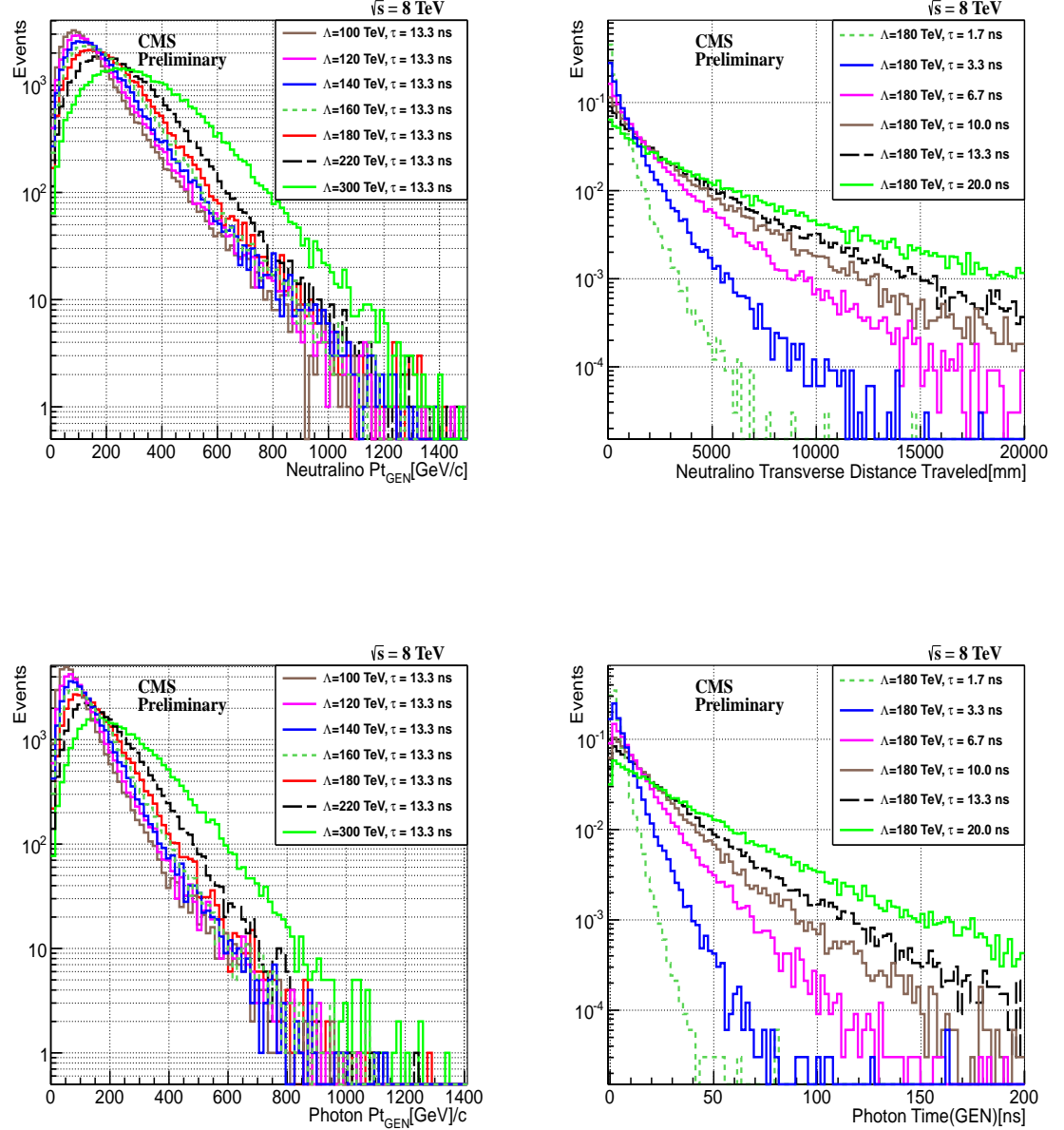


Figure 2.9: Neutralino transverse momentum ( $p_T^{\tilde{\chi}_1^0}$ ) distribution (top left) and transverse distance traveled (top right). Transverse momentum (bottom left) and time (bottom right) of photon from neutralino decay for different  $\Lambda$  and  $c\tau$  points.

These distributions are for different  $\Lambda$  and  $c\tau_{\tilde{\chi}_1^0}$  points of the SPS8 benchmark GMSB model. We find that  $p_T^{\tilde{\chi}_1^0}$  increases with  $\Lambda$ , from  $\Lambda = 100$  TeV to 220 TeV. This is because as  $\Lambda$  increases the masses of the gluino/squark also increases and so does  $p_T^{\tilde{\chi}_1^0}$  since the  $\tilde{\chi}_1^0$  is produced from the decay of the gluino/squark. In a similar argument, increasing the mass of  $\tilde{\chi}_1^0$  ( $m_{\tilde{\chi}_1^0}$ ) through increasing  $\Lambda$  leads to increase in the photon  $p_T$ . For a given value of  $\Lambda = 180$  TeV, which means the  $p_T^{\tilde{\chi}_1^0}$  is fixed, the transverse distance traveled by the  $\tilde{\chi}_1^0$  before decay (shown in the top right plot of Figure 2.9) and photon time (shown in the bottom right plot of the same figure) increases with increasing value of the mean lifetime of  $\tilde{\chi}_1^0$  from  $c\tau = 500$  mm ( $\tau = 1.7$  ns) to 6000 mm ( $\tau = 20.0$  ns). These observations support our expectation that the photon is delayed primarily due to the long lifetime or distance traveled by the  $\tilde{\chi}_1^0$  before it decays.

The photon from the decay of  $\tilde{\chi}_1^0$  can arrive late at ECAL for either one of the following reasons: first, because the  $\tilde{\chi}_1^0$  is traveling slow i.e. with boost,  $\beta = \frac{p_{\tilde{\chi}_1^0}}{m_{\tilde{\chi}_1^0}} \ll 1$ , and second, because the  $\tilde{\chi}_1^0$  is produced with significant boost in the forward direction such that the photon travel to ECAL through a non-direct flight path from the nominal  $pp$  interaction point. We study these two scenarios of the photon delay by estimating the photon arrival time at ECAL in each scenario using the distance traveled by  $\tilde{\chi}_1^0$  before it decays and the distance traveled by the photon from the decay point to ECAL. Figure 2.10 (left) shows a schematic representation of possible flight paths of the photon to ECAL. The estimated photon arrival ECAL time in each scenario is given as follows:

- Delay due to slow moving neutralinos:  $\Delta t_1 = (L1/c\beta) - (L1/c)$
- Delay due to non-direct traveled flight path:  $\Delta t_2 = (L1 + L2 - L3)/c$
- ECAL time recorded or measured =  $\Delta t_1 + \Delta t_2$

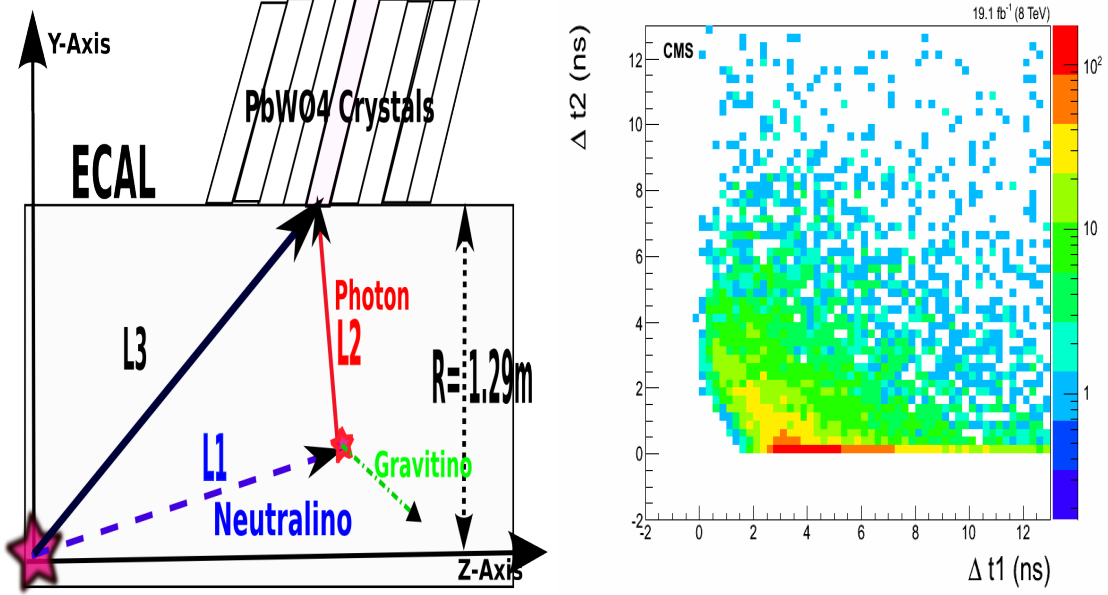


Figure 2.10: Schematic diagram (left) of  $\tilde{\chi}_1^0 \rightarrow \gamma + \tilde{G}$  decay topology within the ECAL volume of the CMS detector. The estimated photon arrival time (right) at ECAL from the decay of  $\tilde{\chi}_1^0$  in the SPS8 benchmark GMSB model with  $m_{\tilde{\chi}_1^0} = 256\text{ GeV}/c^2$  and  $\tau = 20\text{ ns}$ .

The  $\tilde{\chi}_1^0$  is traveling with velocity,  $v = c\beta$ , where  $c$  is the speed of light in vacuum. The distribution of the estimated delay in the photon arrival times due to the two sources,  $\Delta t_1$  and  $\Delta t_2$ , is shown in Figure 2.10(right), where the color intensity represents the photon population. We find that most of the late arrival time photons are from the decay of slow moving  $\tilde{\chi}_1^0$  compared to those from non-direct flight path of the photon to ECAL. This proves that when  $c\tau$  is not so small a good number of  $\tilde{\chi}_1^0$ 's which are produced with low momentum such that the ratio  $\frac{p_{\tilde{\chi}_1^0}}{m_{\tilde{\chi}_1^0}} \ll 1$ , produces most of our detectable delayed photons using ECAL timing measurements. On the other hand, very long lifetime ( $c\tau$ )  $\tilde{\chi}_1^0$ 's which are produced with high momentum will very likely produce photons which escape the ECAL unless the  $\tilde{\chi}_1^0$  decays inside the ECAL volume and the photon from the decay arrives at ECAL through a non-direct flight path.

## 2.4 Previous Search Experiments

There have been previous search experiments for events with delayed photons in their final state using the photon arrival time and missing transverse energy. Most (except

CMS which searched for events with at least one photon) of these experiments searched for events with at least two photons in the final state and interpreted their results in the context of the SPS8 benchmark GMSB model. The results shown in Figure 2.11 are from DØ, CDF, CMS and ATLAS [23, 24, 25, 26, 27] experiments and they present the excluded regions (shaded) in the mean lifetime ( $c\tau_{\tilde{\chi}_1^0}$  [mm] or  $\tau_{\tilde{\chi}_1^0}$  [ns]) and effective SUSY breaking scale ( $\Lambda$  [TeV]) or mass ( $m_{\tilde{\chi}_1^0}$  [GeV/c<sup>2</sup>]) of the lightest neutralino ( $\tilde{\chi}_1^0$ ) in the decay,  $\tilde{\chi}_1^0 \rightarrow \gamma + \tilde{G}$ . Figure 2.11 (left) is produced from the search on data recorded by the ATLAS detector during  $pp$  collisions at a center of mass energy,  $\sqrt{S} = 7$  TeV while Figure 2.11 (right) is from DØ, CDF, CMS experiments with  $p\bar{p}$  collision at  $\sqrt{S} = 1.9$  TeV for DØ and CDF and  $pp$  collision at  $\sqrt{S} = 7$  TeV for CMS.

The important message from the results of these experiments is that within the SPS8 benchmark GMSB model,  $\tilde{\chi}_1^0$ 's with mass,  $m_{\tilde{\chi}_1^0} \leq 245$  GeV, and mean lifetime,  $\tau_{\tilde{\chi}_1^0} \leq 3$  ns, are excluded at hadron colliders with the excluded region in  $\tau_{\tilde{\chi}_1^0}$  and  $m_{\tilde{\chi}_1^0}$  shrinking as the effective SUSY breaking scale,  $\Lambda$ , increases.

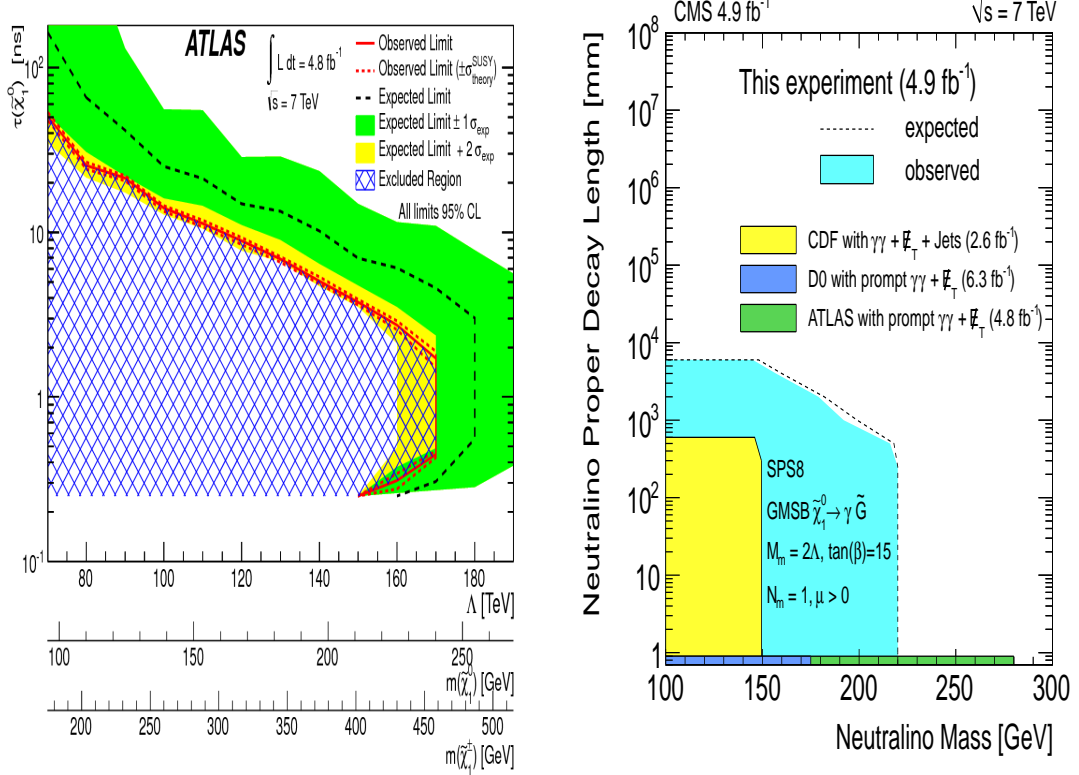


Figure 2.11: Neutralino lifetime and mass upper limit from ATLAS (left) and CMS (7 TeV), D $\emptyset$  and CDF experiments (right) from the search for events with delayed or non-pointing photons.

# Chapter 3

## Hadron Collider and Detector

The Large Hadron Collider (LHC) is a circular particle accelerator at CERN which accelerates two beams of either protons or ions in opposite directions in a circular ring and then collides the beams against each other at a collision point. Located at one of these collision points is a general purpose multi-particle detector called the Compact Muon Solenoid (CMS). Detailed descriptions of the LHC and CMS detector can be found in [28] and [29, 30].

### 3.1 Large Hadron Collider

#### 3.1.1 Overview

The LHC accelerates and collides proton and heavy ion beams at a design center of mass energy,  $\sqrt{S}$ , of 14 TeV. It is located across the border between France and Switzerland and hosted by the European Organization for Nuclear Research (CERN). Powerful superconducting magnets are used to control and maintain the circulation of the beams in a circular ring of nearly 27 km in circumference. The circulating beams gain energy as they are transferred from first a linear accelerator to a Booster and eventually into the LHC synchrotron where at 7 TeV they are steered by focusing magnets to a head-on collision at a collision point. Figure 3.1 shows the LHC and the different stages of accelerating the proton beams prior to collision.

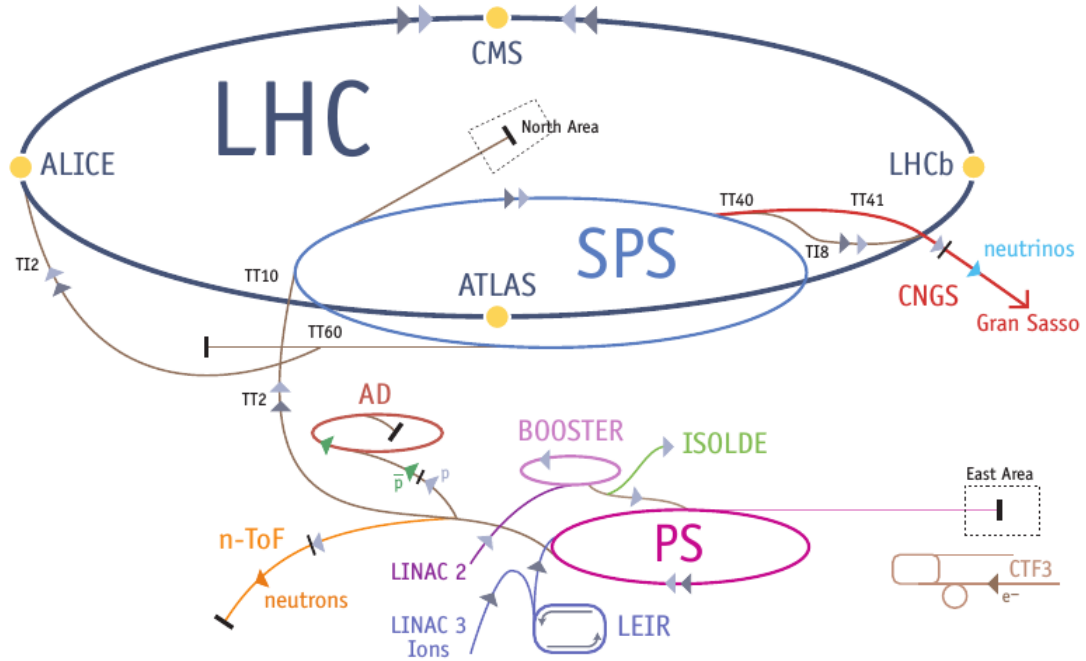


Figure 3.1: Schematic diagram showing the full Large hadron Collider.

### 3.1.2 Colliding Energy

The LHC has an injection chain which comprise of four (LINAC2, PSB, SB and SPS) particle accelerators. The proton source is a simple bottle of hydrogen gas where the orbiting electrons are stripped from the hydrogen gas to produced positive hydrogen ions (protons) using an electric field as the hydrogen gas passes through the first particle accelerator called LINAC2. The LINAC2 uses electromagnetic fields inside Radio Frequency (RF) cavities to accelerate the protons to an energy of 50 MeV creating a stream of particles called *proton beams* which are arranged in packets or *bunches*. The proton beams from LINAC2 are injected into the circular PROTON SYNCHROTRON BOOSTER (PSB) where the protons gain acceleration as they pass many times through the RF cavities with their energy increasing after each pass up to a design energy of 1.4 GeV after which the protons are injected into the PROTON SYNCHROTRON (PS) accelerator. The PS accelerates the protons to an energy of 25 GeV and at this stage the protons are traveling at 99.93% the speed of light. The proton beams are transferred

to the SUPER PROTON SYNCHROTRON (SPS) where further acceleration brings their energy to 450 GeV. The 450 GeV protons are finally transferred into the LHC ring (split into two beams accelerating in a clockwise and anti-clockwise directions) where they are accelerated for about 20 minutes to their nominal energy of 7 TeV and traveling with the speed of 99.9999% the speed of light before being squeezed by quadrupole magnets to collide head-on. The LHC uses electromagnets (dipole magnets) which can produce up to 8.4 Tesla magnetic fields to keep the beams traveling in the circular LHC ring. In a circular particle collider like the LHC the energy available to make new particles, which is the *center of mass* (COM) energy denoted as  $\sqrt{S}$ , is simply the sum of the energy of the two beams i.e.  $\sqrt{S} = E_{\text{beam1}} + E_{\text{beam2}}$ . This is larger than the available energy for fixed target colliders whose energy is  $\sqrt{E_{\text{beam}}}$ . For example, each LHC proton beam is designed to have an energy of 7 TeV making  $\sqrt{S} = 14 \text{ TeV}$ . This increase energy makes it more likely for new massive particles to be produced at a circular collider than at a linear collider.

### 3.1.3 Luminosity

Luminosity is defined as a measure of the number of collisions that can be produced in a collider per area per second and serves as the proportionality factor between the number of events per second and the cross section of the physics process producing the events. Luminosity depends on a number of factors which include the flux i.e. number of particles of the beams per second, the size of the beam at collision and the frequency of the collisions. The *integrated luminosity* which is defined as the total luminosity over a given period of time of about a year quantifies the amount of data that has been recorded by a particle detector and it represents the number of events produced from many different physics processes. Using the measured luminosity ( $\mathcal{L}$ ) and the predicted cross section ( $\sigma_p$ ) of a given physics process we can estimate the number of events per second (event rate ( $R$ )) we expect to be produced during  $pp$  collisions as

$$R = \mathcal{L} \cdot \sigma_p. \quad (3.1)$$

However, in cross section measurement experiments the observed number of events ( $N$ ) and the integrated luminosity are used to calculate the cross section ( $\sigma$ ) of a physics

process using the relation

$$\sigma = \frac{N}{\mathcal{A} \times \epsilon \times \mathcal{L}}, \quad (3.2)$$

where  $\epsilon$  and  $\mathcal{A}$  are the efficiency and acceptance, respectively, of the observed number of events passing some event selection criteria. The measured cross section can be compared to what is predicted by a given model in order to prove or disprove the model.

The LHC has been designed to collide proton beams with a peak instantaneous luminosity of  $1 \times 10^{34} \text{ cm}^{-2} \text{s}^{-1}$  and the total integrated luminosity measured by the CMS detector is separated into the “recorded” and “delivered” integrated luminosity. Delivered luminosity refers to the luminosity delivered by LHC to CMS and one would expect this to be equal to the amount recorded. However, there are instances when the CMS detector is unable to record data either because CMS Trigger and Data Acquisition System (TriDAS) are down or one of the CMS sub-detectors is temporarily being repaired. Figure 3.2 shows a monthly total integrated luminosity delivered by LHC and recorded by the CMS detector during the 8 TeV  $pp$  collisions.

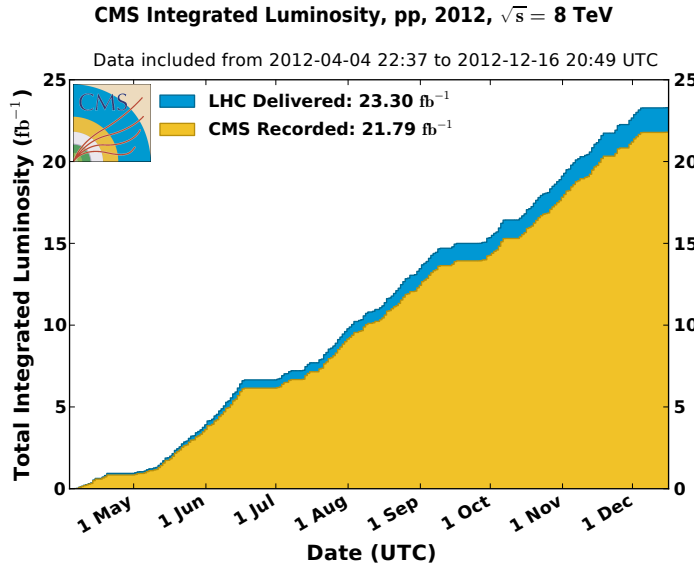


Figure 3.2: Cumulative luminosity versus month delivered (blue) by the LHC and recorded (orange) by CMS detector during stable beams of  $pp$  collisions at  $\sqrt{S} = 8 \text{ TeV}$  in 2012.

### 3.1.4 LHC Bunch Structure

The LHC proton bunch train filling and splitting scheme in the PS, SPS and LHC accelerators is organized in such a way that not all the RF buckets are filled with protons. The empty RF buckets or beam gaps provide the time required during beam injection, cleaning and dumping and avoid parasitic collisions near the collision point. The LHC RF system has a frequency of 400 MHz which means in the LHC ring each RF bucket filled or empty is separated in time from the next one by approximately 2.5 ns. The main proton bunch carries about  $10^{11}$  protons. During the filling in LINAC2 and the proton bunch train splitting in the PS and SPS (using appropriate amplitude and phase parameters of the RF cavities operating on harmonics) into much shorter proton bunches where each bunch occupies an RF bucket, it is possible that some protons end up filling adjacent empty RF buckets. The mistakenly filled empty RF buckets have a much smaller (of the order of  $10^{-5}$  smaller) proton population compared to the main proton bunch and can either be trailing or leading the main proton bunch. *Satellite* bunches lead or trail the main proton bunch within the a 12.5 ns window of the main bunch while *Ghost* bunches lead or trail the satellite bunches as can be seen in Figure 3.3 which shows a longitudinal profile of a typical LHC bunch train or orbit [31].

The presence of ghost/satellite bunches increase the uncertainty in LHC luminosity measurements and can also generate  $pp$  interactions near the collision point and their effects on the instantaneous luminosity measurements have been studied by CMS, ATLAS and ALICE experiments. Figure 3.4 taken from ATLAS and CMS show a clear presence of events produced from ghost and satellite bunch collisions. CMS uses the energy deposits in the endcap calorimeters to observe time spaced clusters which are consistent with the expectations from ghost/satellite bunches while ATLAS uses an LHC beam profile monitoring detector known as the LONGITUDINAL DENSITY MONITOR (LDM) to study the effects and events produced from ghost/satellite bunches. The details of these studies can be found in [32, 33].

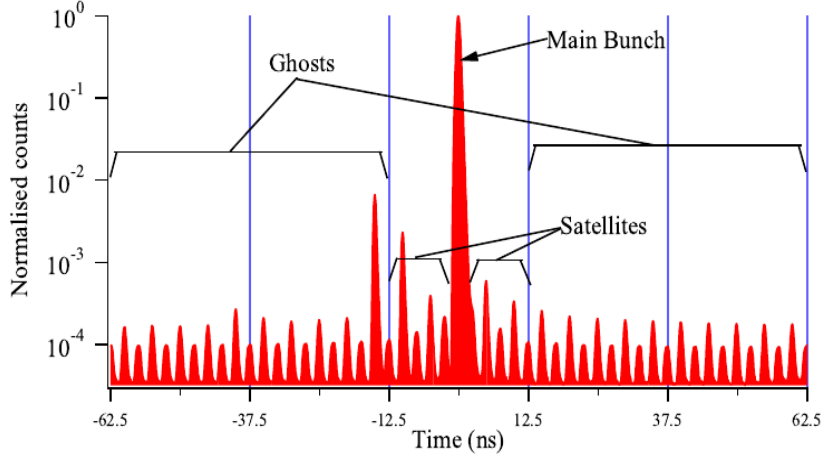


Figure 3.3: Longitudinal profile of a typical LHC proton beam taken with the Longitudinal Density Monitor (LDM) detector. Ghost/Satellite bunches and the main proton bunch shown.

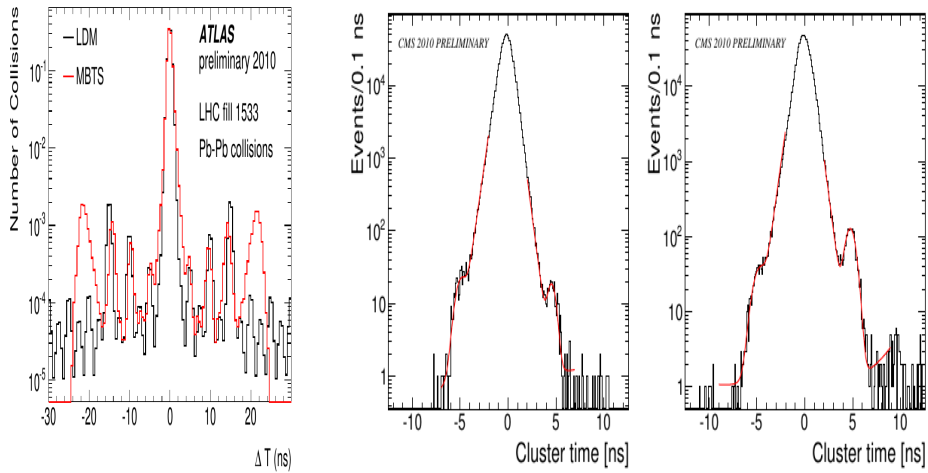


Figure 3.4: Left: Arrival time (red) of events in ATLAS for LHC fill 1533 during 2010  $PbPb$  collision and an LDM profile (black) for Beam2 (same for Beam1). Right: Cluster time in the CMS endcap calorimeters from fill 1089 of the positive endcap detector(left side of IP  $z > 0$ ) (left) and negative endcap detector(right side of IP,  $z < 0$ ) (right). Both plots show a clear presence of events from Ghost/Satellite bunches with the expected time separation.

## 3.2 Compact Muon Solenoid

### 3.2.1 Overview

The Compact Muon Solenoid (CMS) detector is located at one of the  $pp$  collision points along the LHC ring known as POINT 5. The detector has a simple cylindrical structure consisting of a barrel and two endcap regions and its design choice balances cost and robustness in the detection of many different particles. An extensive forward calorimetry detector provides an almost  $4\pi$  solid angle coverage which assures good hermetic particle detection needed for measuring missing transverse energy. The overall length of 21.6 m, a diameter of 14.6 m and weight of 12,500 tons define the size of the CMS detector. Figure 3.6 shows the CMS detector with its different sub-detectors and type of material used for their construction.

The main feature of the CMS detector is the presence of a superconducting solenoid magnet of 6 m internal diameter. The magnet provides a strong magnetic field of 3.8 Tesla which causes the bending of the tracks of charge particles as they travel across the detector. The particle's momentum is measured from the reconstructed track.

The magnetic field encloses an entirely silicon pixel and strip tracker detector which are used for finding the vertex points and for reconstructing tracks of charged particles, a lead-tungstate ( $\text{PbWO}_4$ ) scintillating-crystal Electromagnetic Calorimeter (ECAL) and a brass and plastic scintillator sampling Hadron Calorimeter (HCAL) which are used for measuring the energies of electromagnetic and hadronic particles, respectively. Very long lived particles like muons are detected using gas-ionization detectors embedded in the flux-return iron-yoke located at the outermost region of the detector called Muon Chambers.

The CMS detector employs a three-dimensional Euclidean coordinate system with the directions of  $x$ ,  $y$ , and  $z$ -axes as shown in Figure 3.7, where the origin coincides with the center of the detector, where the nominal  $pp$  collisions occur called the *interaction point* (IP). For particle identification CMS uses a more convenient coordinate system based on the polar coordinates where the azimuthal angle,  $\phi$ , is measured in the  $x - y$  plane with  $\phi = 0$  being the  $x$ -axis and  $\phi = \pi/2$ , the  $y$ -axis. The radial distance in this plane is denoted  $R$  and the polar angle,  $\theta$ , measured from the  $z$ -axis is related to the *pseudo-rapidity*,  $\eta$ , through the relation:  $\eta = -\ln \tan(\frac{\theta}{2})$ . The coordinate system,

$(\eta, \phi, R)$ , is used to identify a point in the cylindrical volume of the CMS detector. We now describe in detail the CMS sub-detectors used in our analysis.

### 3.2.2 Calorimeters

The calorimeter absorbs a good fraction of the energy of an incident particle and produces a signal with an amplitude proportional to the absorbed energy. The energy absorption happens through the cascade production of secondary particles with the energy of the incident particle directly proportional to the number of secondary particles produced. There are two types of calorimetry choices used in the CMS detector: an *Electromagnetic Calorimeter* (ECAL) which is used for absorbing the energy of electromagnetic particles like photons and electrons and a *Hadronic Calorimeter* (HCAL) constructed with more than one type of material and is used for absorbing the energy of hadrons such as kaons and pions. The combined calorimeter subdetectors in CMS covers a region of  $|\eta| < 5$ , making it nearly hermetic which is needed for good missing transverse energy measurements. ECAL and HCAL are arranged in a nested fashion shown in Figure 3.5 with the HCAL enclosing the ECAL so that electromagnetic particles can be distinguished from hadronic particles by comparing the energy deposited in both calorimeters.

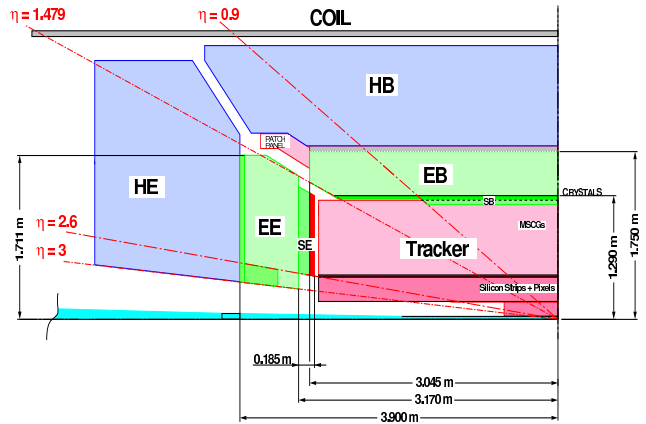


Figure 3.5: Schematic diagram of CMS calorimetry system with HCAL enclosing ECAL in the barrel and endcap regions.

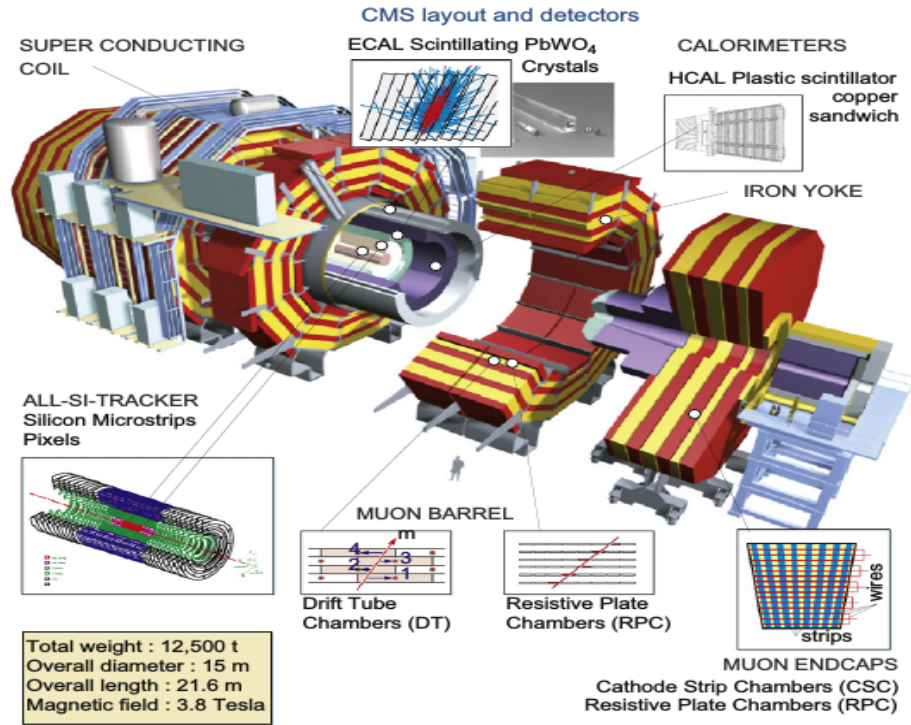


Figure 3.6: CMS Detector showing the different subdetectors and their material.

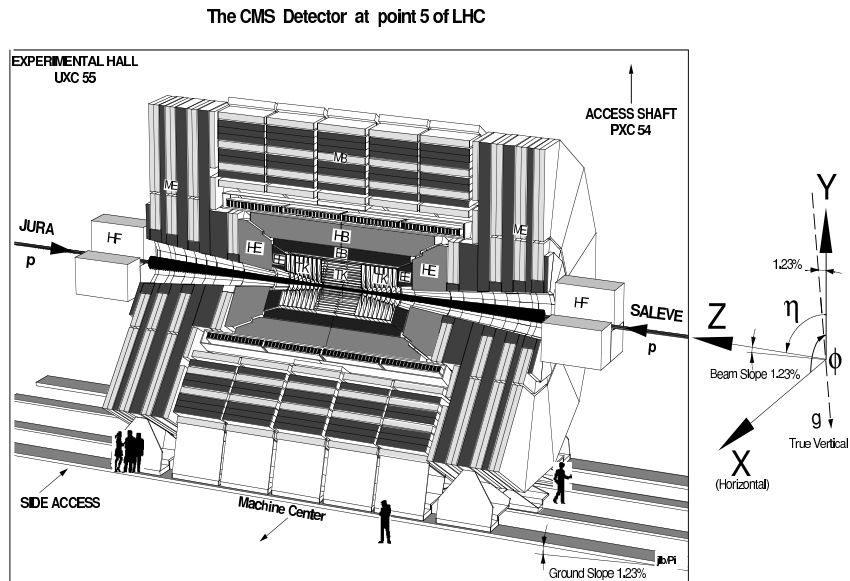


Figure 3.7: CMS detector schematic view with definition of  $x - y - z$  coordinates.

## Electromagnetic Calorimeter

The Electromagnetic Calorimeter (ECAL) detects photons and electrons through their interaction with the atoms of the lead tungstate ( $\text{PbWO}_4$ ) crystals. During this interaction process, which might happen through Coulomb scattering (electron-neutron scattering), Compton scattering (photon-electron scattering), photon emission (also known as *Bremsstrahlung*) and electron-positron pair production, the incoming photon or electron deposits practically almost all of its energy into the detecting  $\text{PbWO}_4$  crystals. Electrons loss most of their energy due to their small mass through radiation (photon emission). High energy electrons and photons of several GeV deposit their energy to the  $\text{PbWO}_4$  crystals through Bremsstrahlung and pair production interaction processes producing electrons, positrons and photons in the process which subsequently produce more electrons, positrons and photons creating an avalanche of electrons, positrons and photons called an *electromagnetic shower*. The process stops when the electron or photon energy becomes low for either pair production or Bremsstrahlung processes to occur. The probability of an electromagnetic particle with high energy to interact either through Bremsstrahlung or pair production with the detecting material is proportional to the square of the atomic number,  $Z^2$ , of the material.

The choice of  $\text{PbWO}_4$  crystals as the calorimetry material for operation in the LHC environment by CMS is because of the following reasons:  $\text{PbWO}_4$  crystal is a high  $Z$  material with a density of  $8.28 \text{ g/cm}^3$ , it has a short radiation length ( $X_0 = 0.89 \text{ cm}$ ) and a small Molière radius ( $R_M = 2.2 \text{ cm}$ ). The dense nature of the  $\text{PbWO}_4$  crystals allow for the electromagnetic shower to develop early and therefore likely to be fully contained within a compact detector like CMS. The short radiation length ensures that on average about 95 % of the electromagnetic shower energy produced by the photon or electron is contained within a crystal volume of about 9 crystals while the small Molière radius reduces the transverse spread of the electromagnetic cascade from multiple scattering of electrons and helps improve the estimation of the transverse position of impact of an incident particle. The arrangement of the  $\text{PbWO}_4$  crystals also provide a fine granularity for measuring the particle's energy by providing fewer overlap of particle signals.  $\text{PbWO}_4$  crystal is also preferred to other crystal materials because of its high radiation resistance and fast scintillation decay time which is comparable to the LHC bunch crossing interval of 25 ns required for the high radiation dose and fast timing (25 ns

proton bunch spacing) LHC environment. About 80% of the energy absorbed by the  $\text{PbWO}_4$  crystal is emitted as light in less than 25 ns.

The ECAL has 75848  $\text{PbWO}_4$  crystals in total mounted in a cylindrical geometry comprising of a barrel (EB) and endcap (EE) regions as shown in Figure 3.8.

The EB region of the ECAL covers a pseudo-rapidity range of  $|\eta| < 1.479$ . It has 61,200 crystals providing a granularity of 360-fold in  $\phi$  and  $(2 \times 85)$ -fold in  $\eta$ . The crystals are mounted in a quasi-projective geometry so that their axes make an angle of  $3^\circ$  with respect to a line vector from the nominal interaction vertex in  $\eta$  and  $\phi$  directions. This is to avoid loss of energy into cracks aligned with a particle's trajectory. A crystal in EB has a cross-section corresponding to approximately  $0.0174 \times 0.0174(1^\circ)$  in  $(\eta, \phi)$ ,  $22 \times 22 \text{ mm}^2$  at its front face and  $26 \times 26 \text{ mm}^2$  at its rear face. and is 230 mm long which is about  $25.8 X_0$  radiation lengths. The crystal's radial distance measuring from the center of the face of the crystal to the beam line is 1.29 m. For simplicity of construction and assembly, a group of  $2 \times 5$  crystals are placed in a very thin walled ( $200 \mu\text{m}$ ) alveolar structure to form a *submodule*. To reduce loss in the light collected from the rear face of each crystal, the internal surface of the alveolar structure is coated with aluminum which is a reflective material and it avoids oxidation which leads to coloration. Each submodule is arranged into 4 modules of different types according to their  $\eta$  position. There are about 400 to 500 crystals in each module and these 4 combined make one *supermodule* containing 1700 crystals. On the rear end of each EB crystal, two *Avalanche Photodiodes* (APD) are glued to collect the scintillating light from the crystals and converting the light into charge current which is further amplified by the read-out electronics.

The EE region cover a pseudo-rapidity range of  $1.479 < |\eta| < 3.0$  and placed immediately in front of it is a PRESHOWER (ES) detector made of silicon strip sensors interleaved with lead. The purpose of the preshower is to identify photons from the decay of neutral pion,  $\pi^0 \rightarrow \gamma\gamma$ , and also to help separate photons producing electrons through pair production from photons not producing electrons before their arrival at the EE. The endcap located on the  $+z$  side of the nominal IP is denoted EE+ while the other located on the  $-z$  side is denoted as EE-. The longitudinal distance between the IP and the center of the surface of the EE crystal is 3.154 m. Each endcap is divided into two halves called DEEs with each DEE holding 3662 crystals. Crystals in EE with

identical shape are grouped into  $5 \times 5$  mechanical units called *supercrystals* (SC). The crystals in the SC form an  $x - y$  grid. Each crystal is 220 mm ( $24.7 X_o$ ) in length and has a front and rear face cross sections of  $28.62 \times 28.62$  mm $^2$  and  $30 \times 30$  mm $^2$ , respectively. A VACUUM PHOTOTRIODE (VPT) instead of an APD is glued on the rear face of each crystal for receiving and converting the scintillating light into electrical signals. The VPT is used in the EE because of its high resistance to radiation and smooth operation in a strong magnetic field environment. CMS uses APDs and VPTs because they are not affected by the high magnetic field and they have a high gain relative to regular photodiodes which have no gain. Although the light yield for PbWO<sub>4</sub> crystals is rather low ( $\approx 70$  photons/ MeV), these photo-detectors have internal gain (50 for APDs and 10 for VPTs) and quantum efficiency of 75 % for APDs and 20 % for VPTs which makes it possible for them to detect the signals from incident particles with energies ranging from a few to high GeV. The signals from the APDs and VPTs are amplified and digitized by voltage-sensitive analogue-to-digital converters and transported through optical fibers as digital light signals to the underground counting room which is located adjacent to the CMS experimental cavern.

The energy resolution and geometry structure of the ECAL ensures that the photon or electron's energy, arrival time, position and even the direction through the shape of its electromagnetic shower in the crystals is measured with good precision.

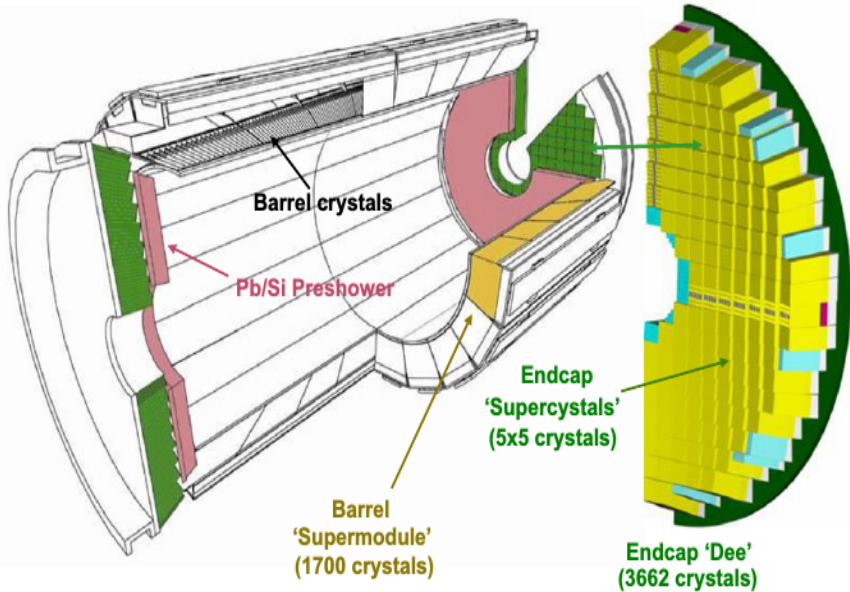


Figure 3.8: Layout of the CMS electromagnetic calorimeter showing the arrangement of crystal modules, supermodules in the barrel with the preshower in front of endcap with supercrystals.

### ECAL Readout Electronics

The ECAL readout electronics is divided into an On-Detector or Front End (FE) and an Off-Detector (OD) electronics. The FE electronics board is installed inside the detector volume behind the crystals and in front of the hadron calorimeter and is made with radiation-hard electronics to withstand the high radiation dose. Data from the FE is transferred by radiation hard fibers to the OD electronics which is in the underground service cavern located approximately 80 m from the CMS detector.

A Clock and Control Unit (CCU) chip on each FE board communicates through bi-directional optical links with the Clock and Control System (CCS) board of the OD. These links carry clock and control signals and the trigger Level 1 accept (L1A) signal from the Timing, Trigger and Control (TTC) board and the Trigger Control System (TCS). A voltage controlled Quartz Phase-Lock Loop (QPLL) time jitter-filter and clock multiplier chip with an output clock jitter of 16 ps rms ensures that the LHC clock signal is transmitted to both the FE and OD electronics for timing synchronization.

Each FE board, shown in Figure 3.9, receives signals from a group of crystals typically forming a  $5 \times 5$  crystal matrix and hosts five Very Front End (VFE) boards with each VFE board holding five analog channels. Each channel, shown in Figure 3.10, is carrying the signal from a single crystal and consists of a Multi-Gain Pre-Amplifier (MGPA) and three identical 12 bit Analog-to-Digital Converters (ADC) which are used to amplify, shape and digitize the signal coming from the Photo-Diode.

The MGPA chip has 3 gain ranges with gain ratios of 1, 6 and 12 to span the overall dynamic range of the signal which can go from 12 MeV up to 1.7 TeV. Equipped with a Capacitor-Resistor-Resistor-Capacitor (CR-RC) filter with a pulse shaping time of 40 ns and less than 1% of non-linearity, the MGPA ensures a uniform pulse shape matching and linearity across all 3 gain ranges allowing for precise pulse shape reconstruction across every channel.

The required readout and precision performance of the FE electronics demands a 12-bit ADC chip with a sampling frequency of 40 MHz to digitize the analog pulse signal of the highest unsaturated range into 10 discrete samples with an electronic noise of about 40 MeV. The FE card stores the digitized crystal data (ten 40 MHz discrete samples per channel) in 256-word-deep memories called *pipelines*. Five such pipelines and the logic to calculate the energy sum of 5 crystals once every LHC proton bunch crossing is integrated into a  $0.25 \mu\text{m}$  technology FERNIX ASIC chip. Each VFE card is serviced by one such chip allowing for the energy to be summed in strips of 5 crystals along  $\phi$ . In EE the five strip energy sums are transmitted to the Trigger Concentration Card (TCC) on the OD electronics, while for EB a sixth chip sums the five strip energy sums and calculates the “fine-grain” electromagnetic bit which identifies the electromagnetic shower candidates on the basis of the energy profile of the  $5 \times 5$  crystal matrix or *Trigger Tower* (TT). The TT energy sum and the fine grain bit are transmitted to the TCC at 800 Mbits/s. The corresponding crystal data (the ten 40 MHz discrete samples per crystal) upon receipt of a positive trigger L1A decision is transmitted to the Data Concentration Card (DCC) also on the OD electronics system over a distance of approximately 80 m through optical fibers at a data transfer rate of 800 Mbits/s.

The OD electronics system shown in Figure 3.11 hosts the DCC, TCC and CCS electronic boards. It serves both the Data Acquisition (DAQ) and trigger paths. In the DAQ path, the DCC collects the digitized crystal data from up to 68 FE boards and

performs data verification and data reduction based on readout flags from the Selective Read-Out Processor (SRP) system while in the trigger path the TCC collects trigger data from up to 68 FE boards corresponding to a supermodule in the barrel and 48 FE boards corresponding to the inner and outer part of a  $20^\circ$  in  $\phi$ . The TCC completes a Trigger Primitive Generation (TPG) process started at the FE by computing *trigger primitives* and synchronized them by the Synchronization and Link mezzanine Board (SLB) before their eventual transmission to the Regional Calorimeter Trigger system at each LHC proton bunch crossing. Each Trigger Primitive (TP) consist of the summed transverse energy deposited in each TT and the fine-grain bit. The 24 bits TP are stored in the TCC during a Level-1 trigger latency and multiplexed into an 8-bit word encoding the summed transverse energy in a tower and the fine-grain bit and finally transferred to the DCC at a rate of 1 word/25 ns.

The CCS is tasked primarily with distributing fast timing signals (LHC 40.08 MHz clock, L1A and control signals) to the TCC, DCC and CCUs of the FE board. By interfacing the On- and Off-detector electronics to the TCS and Trigger Throttling System (TTS), the CCS synchronizes all the activities of the OD and configures the On-detector electronics [36].

The 40.08 MHz LHC Bunch-Crossing (BX) clock and 11.246 KHz ( $88.9\ \mu\text{s}$ ) orbit signals from the RF generators of the LHC machine are broadcast over singlemode optical fibers from high power laser transmitters at the Prevessin Control Room (PCR) to the four LHC experiments. The combined signals are received at CMS by a TTC machine interface (TTCmi) minicrate carrying an LHC clock receiver (LHCrx) module and a TTC Clock fanout (TTCcf) module. Embedded in the TTCmi is a voltage controlled QUARTZ PHASE-LOCK LOOP (QPLL) ASIC chip with a clock frequency or locking range of 40.0749 MHz to 40.0823 MHz. The QPLL acts as a jitter-filter and clock multiplier for clock signals operating at the LHC bunch-crossing frequency with an output clock time jitter up to 16 picoseconds (ps) in rms. The QPLL adjusts for any clock phase and then makes multiple copies of the LHC clock signals before distributing them to the local TTC transmitters. The local TTCcf distributes the low-jitter LHC clock signals to the TTC receiver (TTCrx) module of the TTC system which is eventually distributed through optical fibers to FE boards, trigger and OD readout electronics used for Level trigger accept, bunch counter reset, bunch crossing number

event counter reset and event number and the millions of electronics channels. The TTCmi also has master phase adjustment for the orbit signal and facilitates monitoring of clock signal quality. The local TTC system is programmed to distribute to all the trigger synchronization circuits or Synchronization and Link mezzanine Board (SLB) the Bunch-Crossing zero (BC0) broadcast signal.

In the SLB of each TCC, the BC0 timing is synchronized [37] to match the arrival of the bunch zero or first bunch crossing TP data at the SLB. The synchronization circuits make use of FIFOs to archive the synchronization i.e. after a clear FIFO is executed during the LHC extraction gap of 127 missing proton bunches ( $3.2\ \mu s$ ) of the LHC orbit, the first data entering each FIFO must correspond to the bunch zero crossing. This synchronization is needed to account for the non-negligible and unpredictable phase on the trigger primitives arrival time to the processors introduced by different particle flight paths to different regions of the detector, different optical transmission fiber lengths and different phase lock delays in the electronic serializers and ensures that the electromagnetic and hadronic calorimeter trigger primitives in each TT is time aligned with respect to the “bunch 0 clock” which corresponds to the start of the LHC orbit. The synchronized trigger primitives are sent at 1.2 Gbits/s to the Regional Calorimeter Trigger through 10 m electrical cables where with HCAL trigger primitives, the electron/photon and jet candidates are computed together with their total transverse energy.

In the DCC the data integrity is verified and formatted together with the TCC information, the selective readout flags and the crystal data of the selected TT according to the selective readout processor flags. Words of 64 bits are formed and sent to the DAQ at L1A trigger rates provided by the trigger system.

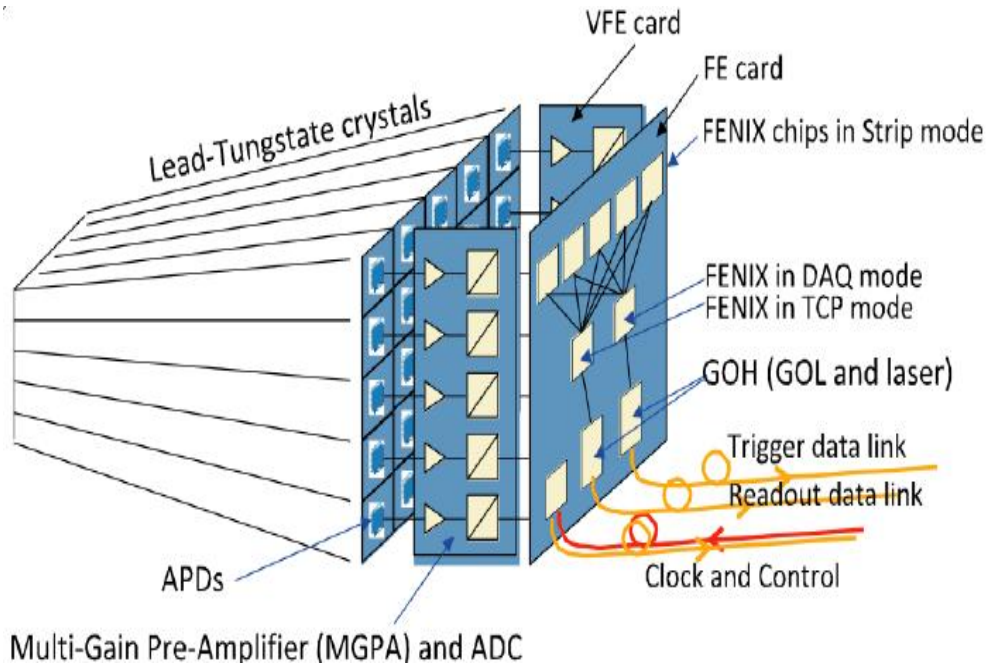


Figure 3.9: Schematic diagram of the ECAL electronics readout Trigger Tower (TT) or Front End (FE) board.

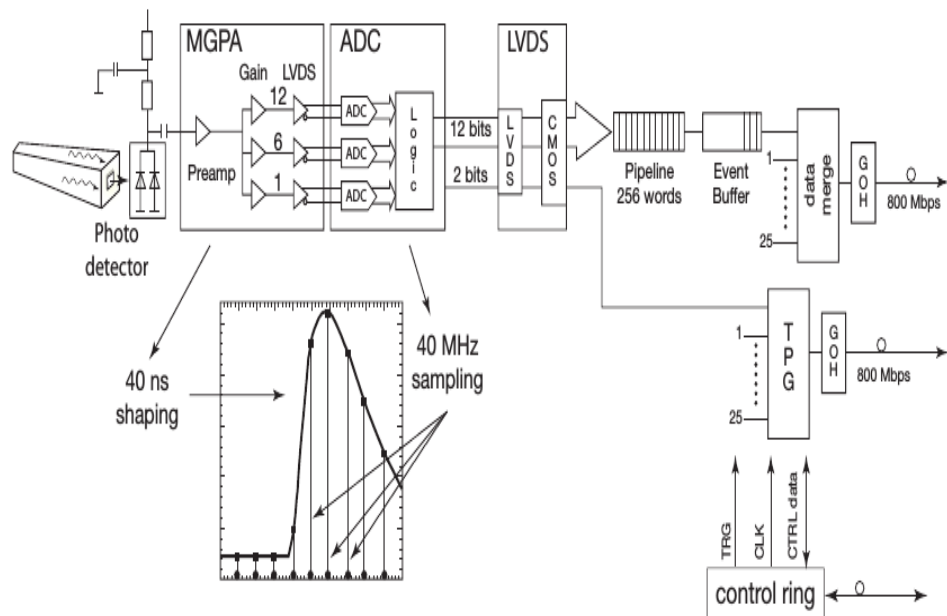


Figure 3.10: Schematic diagram of the ECAL electronics readout for a single crystal.

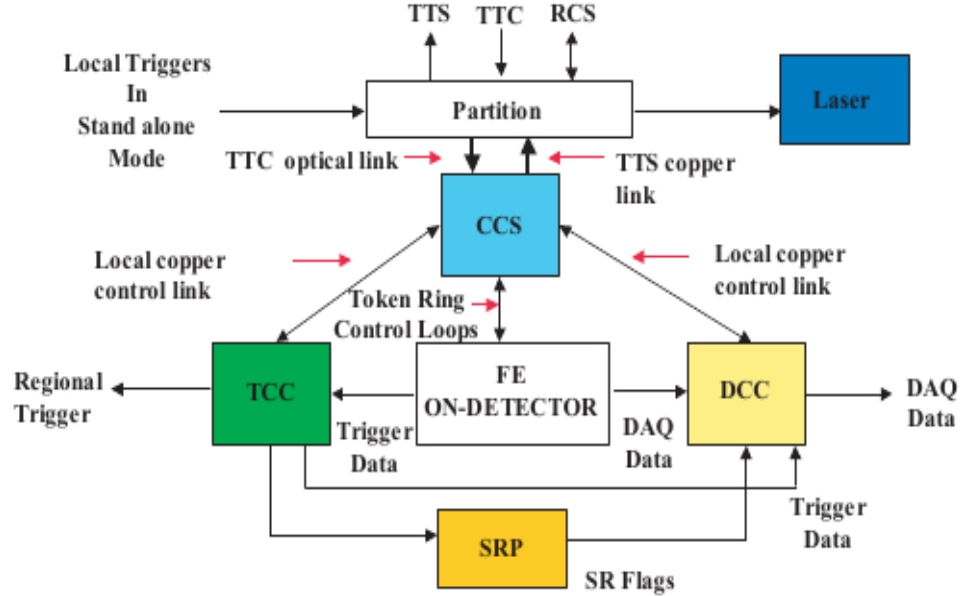


Figure 3.11: Schematic diagram of the ECAL Off-Detector and Readout Architecture.

### Hadronic Calorimeter

The Hadron Calorimeter (HCAL) is important for the measurement of the energies of protons, pions, kaons, fragmenting quarks and gluons known as *jets* with energies in the GeV to TeV range and neutrinos or exotic particles producing apparent Missing Transverse Energy (MET). High-energy hadrons traveling through a medium transfer their energy to the constituent atoms in the medium through ionization or excitation of these atoms. The energy deposition is through the formation of ion-electron pairs (positive ion and electron) which lead to the production of *hadronic showers*. A hadronic shower has an *electromagnetic* (em) and a *non-electromagnetic* (non-em) components. The em component which has about two thirds of the energy deposited by the high-energy hadron is measured in the same way as in ECAL using an active scintillating material while the non-em shower energy is deposited in an absorber material through inelastic collisions of the incident hadron with the nuclei of the atoms of the non-active absorber material. The non-em shower component does not contribute to the measured signal but rather in the production of secondary hadrons which travel through the next layers of the absorber material producing further hadrons and very densely ionizing

particles. This combination of active and non-active materials is the chosen design for high-energy hadron detection in HCAL and is the reason why the HCAL is called a *Sampling Calorimeter*.

The HCAL is comprised of four distinct subdetectors: the Hadronic Barrel (HB), Endcap (HE), Outer Barrel (HO) and Forward (HF). Unlike the ECAL, the HB, HE and HO sub-detectors are scintillator-sampling calorimeters which use brass plates as the inactive absorber material and plastic scintillator tiles as the active material. Embedded in the plastic scintillator tiles are wavelength shifting fibers (WLS) which are used to bring out the light to photodetectors. The brass plate is used to absorb and therefore for the containment of the energetic hadrons as these hadrons produce hadronic showers consisting of an em (particles like  $\pi^0$ ,  $\eta$  and other mesons which decay to photons and develop electromagnetic showers) and non-em (mostly charged pions and kaons) components. The plastic scintillator is used because of its long-term stability and moderate radiation hardness and along with the embedded WLS measures the energy of the em component. HYBRID PHOTODIODES (HPDs) are used in HB and HE as the choice of photodiode due to their low sensitivity to magnetic fields and their large dynamic range to collect the scintillating light brought out through the WLS. The HPDs also have high transient electrical noise and were used during the LHC Run 1 data recording by the CMS detector. During LHC Run 2 which began in July 2015, the HPDs had been replaced with SILICON PHOTON MULTIPLIERS (SiPM) which have low noise.

For pseudo-rapidity range  $|\eta| < 1.48$ , HCAL cells map on to  $5 \times 5$  ECAL crystal matrix to form calorimeter towers projecting outwards from near the nominal interaction point. In each tower, the energy in ECAL and HCAL cells is summed to define the calorimeter tower energy. The energy ratio of an HCAL tower to ECAL in a calorimeter tower energy is used to improve photon and electron identification.

The HB covers a pseudo-rapidity range of  $|\eta| < 1.3$  and is divided into two-half barrel (HB+ and HB-) sections with each section composed of 18 identical  $20^\circ$  in  $\phi$  wedges bolted together to minimize cracks between them. Each wedge is constructed out of flat brass absorber plates aligned parallel with the beam axis. The innermost and outer most plates are made of stainless steel to provide structural strength. The plastic scintillator active material is divided into 16  $\eta$  sectors resulting in a segmentation of  $(\Delta\eta, \Delta\phi) = (0.087, 0.087)$  which provides a fine granularity for energy measurements.

The HE covers a pseudo-rapidity range of  $1.3 < \eta < 3.1$  which is the region containing about 34% of the particles produced in the final state. The HE also uses brass as its absorber material and has plastic scintillation tiles with granularity of  $\Delta\eta \times \Delta\phi = 0.087 \times 0.087$  as in the HB for  $|\eta| < 1.6$  and  $\Delta\eta \times \Delta\phi = 0.17 \times 0.17$  for  $|\eta| > 1.6$ . This granularity provides good measurement of the energy of particles through non-overlapping showers. The HE also consists of an HE- and an HE+.

The HO is an extension of the HB tile outside the solenoid and because the EB and HB might not provide sufficient containment of the hadronic shower in the central pseudo-rapidity region, the HO utilizes the solenoid coil as an additional absorber and is used to identify late starting hadronic showers and to measure the shower energy deposited after HB. For this reason the HO is also known as the *tail catcher* sub-detector. The HO is made of large scintillator tiles and WLS fibers embedded in grooves for good light collection and less attenuation of light.

The HF occupies a pseudo-rapidity region of  $3 < |\eta| < 5$  and thus experiences the largest flux of particles. On average 760 GeV per  $pp$  interaction is deposited into the two forward HF sub-detectors compared to only 100 GeV in the rest of the sub-detectors in HCAL. Because of this very harsh environment of high particle fluxes, the HF calorimetry uses *quartz fibers* which is a combination of fused-silica core and polymer hard-cladding as its active material. A signal is generated when charged showering particles with energy above the Chrenkov threshold (190 keV for electrons) generate light. As a result the HF calorimetry is most sensitive to the electromagnetic component of the hadronic showers. The HF uses steel plates as its absorber material with each plate having 5 mm grooves through which the fibers are inserted into. This provides an arrangement where the HF sub-detector is functionally subdivided into two longitudinal segments with half of the fibers running over the full depth (165 cm) of the absorber plate called *long fibers* and the other half starting at a depth of 22 cm from the front of the detector called the *short fibers*. The two fibers are read out separately and this arrangement makes it possible to distinguish between the showers generated by electrons and photons, which do deposit a large fraction of their energy in the first 22 cm from those of generated hadrons, which produce nearly equal signals in both calorimeter segments (long and short fibers) on average. From the energy measurements of the long fibers (measures the total signal) and the short fibers (measures the energy deposition after 22 cm of steel) we are able to

distinguish between electromagnetic particles like electrons from hadronic particles like pions in the HCAL.

The purpose of the HF in addition to being capable of distinguishing between energetic electrons and pions in the forward region of the HCAL detector is to provide a nearly  $4\pi$  hermetic phase space coverage required for good calculation of MET. MET is the signal for particles like neutrino and exotic particles like gravitinos which escape detection.

### 3.2.3 Muon Chambers

Muon chambers are particle detectors which use the process of ionization and a 2 Tesla magnetic field from the return iron yokes (used for bending the tracks of charge particles) to measure the momentum of charged particles. The three different types of muon chambers used in the CMS detector are: the DRIFT TUBES (DT) chambers in the barrel, CATHODE STRIP CHAMBERS (CSC) in the endcaps and the RESISTIVE PLATE CHAMBERS (RPC) glued to the DT and CSC chambers. Four layers or stations of DT/RPC and CSC/RPC are embedded in an interleaved style with the iron yoke for charge particle track reconstruction and triggering. Figure 3.12 is a longitudinal view of the CMS detector showing the position of the muon stations. The DT and CSC record track segments characterized by the position of the track and the angle of entry. This information is used to determine the precise transverse momentum and charge of the particle during event reconstruction.

The Muon chambers are used primarily for detecting muons and other possibly long-lived charged particles. Muons unlike electrons and hadrons do not deposit most of their energy in the calorimeters and are capable of traveling across the entire CMS detector into the muon chambers. Muons produce tracks which run across the CMS detector starting from the TRACKER (a silicon pixel and strip sub-detector closest to the  $pp$  interaction point), depositing very small fraction of their energies in the calorimeters and unto the muon chambers. The RPCs (DTs and CSC will also be used after the current detector upgrade) are dedicated L1 trigger chambers to determine the candidate muon's approximate transverse momentum and proton bunch crossing number. The RPC has a timing resolution of about 3 ns.

The CMS detector performance for LHC Run 1 and material type of each sub-detector is summarize in Table 3.1.

### 3.2.4 Event Triggering

Assigning particles to the correct  $pp$  collisions or bunch crossing (BX) and storing the partially reconstructed event in the DAQ before the next collision happens in 25 ns is a very challenging problem. In addition to assigning particles to their correct BX, we want to select only potentially interesting events i.e. events with large transverse energy or interesting particle combination so as to reduce the event rate during read-out and since the full event information comes from millions of electronic channels of the CMS detector, the signals from every channel have to be synchronized with the 40.08 MHz LHC bunch crossing frequency. CMS solves these very challenging problems by using a Timing, Trigger and Control system and two event selection triggers: a LEVEL-1 (L1) and a HIGH LEVEL TRIGGER (HLT) trigger.

The L1 trigger consists of custom-designed programmable electronics system implemented in FPGA and ASIC technology and uses information from the calorimeter, muon and a global trigger board. The global trigger makes the final decision based on the decisions of the calorimeter and muon triggers to reject or keep an event for further processing at the HLT trigger. The L1 trigger is responsible for selecting the best 100,000 events/second from the potentially 1 billion events/second produced from  $pp$  collisions. The L1 trigger selection and synchronization starts with the Trigger Primitive Generators (TPGs) which are based on the summed transverse energy deposits in the calorimeter trigger towers and track segments of hit patterns in the muon chambers, respectively. The synchronization of the Trigger Primitives (TPs) with the LHC BX frequency is implemented in the TPG electronics which is integrated with the calorimeter read-out electronics described in section 3.2.2. The calorimeter TPs generation and synchronization begins in the on-detector front-end electronics which receives ADC signals from 25 crystals also known as trigger towers. An off-detector Trigger and Concentration Card communicating with the TRIGGER, TIMING AND CONTROL (TTC) system which distributes the 40.08 MHz LHC BX clock signal, collects the TPs (transverse energy sums) from 68 front-end electronics boards in the barrel and 48 boards in the endcaps, finalizes the TPG generation and store the TPs during a L1 latency before transferring them to the REGIONAL CALORIMETER TRIGGER (RCT) and finally the GLOBAL TRIGGER upon receipt of a Level-1 Accept (L1A) trigger signal from the TTC

system. In the RCT, SYNCHRONIZATION AND LINK BOARDS (SLB) carrying synchronization circuits synchronize the trigger data of each trigger tower. Each trigger tower is aligned with the bunch crossing zero signal by comparing it to histograms of the LHC bunch crossing profile. The aligned data is read by the data concentration card and after verification and reduction of the event size if necessary is sent to the DAQ.

In HCAL the energy values of the front and back towers are added to the trigger primitives and the bunch crossing number is assigned by a peak filtering algorithm. A schematic picture of the CMS Level-1 trigger architecture is shown in Figure 3.13.

The HLT is a software implementation of a sequence of preliminary event selection algorithms and runs on a farm of more than 1000 standard computers. These complex algorithms include instructions like, match tracks to hits from the muon chambers, select energy deposits above a certain threshold in the calorimeters with no tracks and more. The HLT begins the first step of event selection and in a similar fashion to the L1 trigger uses assimilated and synchronized information from different parts of the CMS detector to build and select an event from the energy deposits. By the time the HLT selection process is complete, there are now only 100 events/second with the remaining 99,900 thrown away. Considering an average event size is 1 Megabyte during stable and effective LHC  $pp$  collision period of a year ( $10^7$  seconds), CMS produces about a Petabyte of data each year which is stored and later used for offline physics analysis.

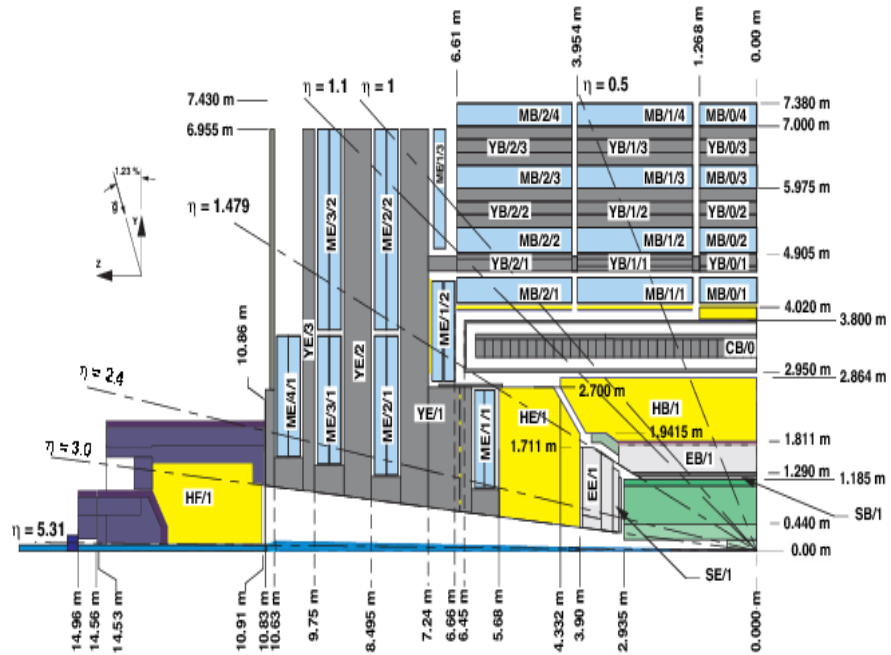


Figure 3.12: Cross section view showing the coverage range of CMS sub-detectors and their longitudinal distance from the IP.

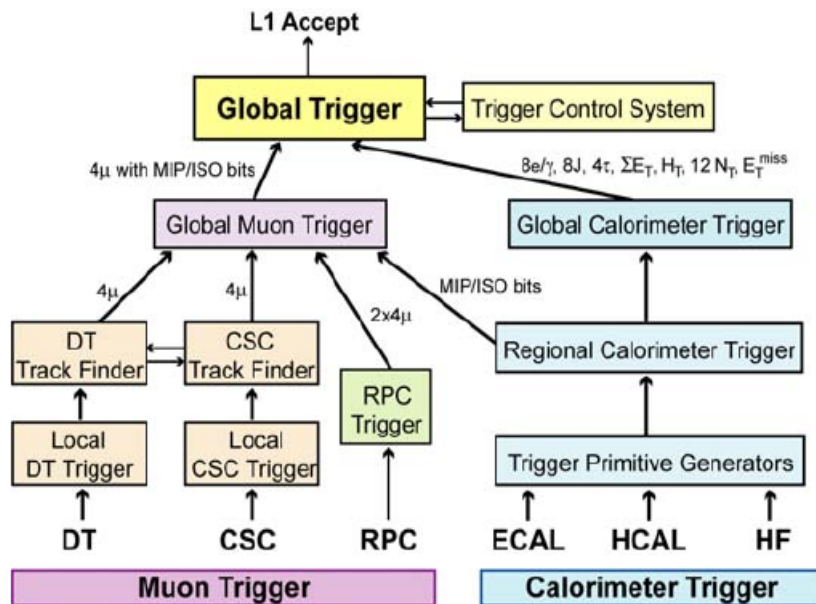


Figure 3.13: Level-1 Trigger Architecture of CMS.

**CMS Sub-detector Performance LHC Run 1 2012**

<b>Sub-detector</b>	<b>Quantity</b>	<b>Performance</b>	<b>Uses</b>
Tracker	Momentum[GeV/c]	$\sigma_T/p_T \approx 1.5 \times 10^{-4} p_T \oplus 0.005$	Silicon Pixels and Strips
ECAL	Energy[GeV]	$\sigma/E \approx 3\% / E \oplus 0.003$	PbWO <sub>4</sub> Crystals
	Time[ns]	$\sigma(t_1 - t_2) = \frac{N}{A_{eff}/\sigma_n} \oplus \sqrt{2}\bar{C}$	
HCAL	Energy[GeV]	$\sigma/E \approx 100\% / E \oplus 0.05$	Brass + Scintilator
Muon Chambers	Momentum[GeV/c]	$\sigma_T/p_T \approx 1\% \text{ } 50 \text{ GeV to } 10\% \text{ } 1 \text{ TeV}$	inner tracker + Muon Systems
Magnetic field	B-field strength[T]	3.8 T + 2 T	Solenoid + Return Yoke
Triggers	On/Off-line		L1(On-line) +HLT(Off-line)(L2+L3)

Table 3.1: CMS Sub-detectors performance for LHC RUN 1 [34].

## Chapter 4

# Time Reconstruction and Resolution

### ECAL Time Overview

The Electromagnetic Calorimeter (ECAL) was designed to precisely measure the energy of electrons and photons with a target barrel resolution of 0.5% for photons with energy more than 50 GeV. In addition to energy measurements, the combination of fast scintillation for PbWO<sub>4</sub> crystals, the electronic pulse shaping and a digitization rate of 40 MHz allows for an excellent time measurement. The time of the signal measured by each crystal is reconstructed from 10 discrete samples of the digitized analog pulse height[35, 36, 38].

#### 4.1 Time Reconstruction

An analog pulse shape from a single crystal is shown in Figure 4.1(a). Overlaying the pulse shape are typical 10 digitized samples in red. The first three samples are taken in the absence of a signal and correspond to the pedestal. The ADC chip responsible for the digitization, has a sampling frequency of 40 MHz, i.e. one sample is made every 25 ns, which is the same rate as the LHC proton-proton bunch collision frequency of one bunch crossing every 25 ns, and a total time of 250 ns corresponding to the 10 digitized samples is covered. In addition, the timing phase of sampling within the 25 ns

interval is adjusted so that the maximum of the signal pulse shape corresponds to one of the digitized samples to within 1 ns. A time reconstruction algorithm uses the 10 digitized samples to measure the time of a single channel by finding the precise time,  $\mathbf{T}_{\max}$ , corresponding to the maximum of the pulse shape [39, 40].

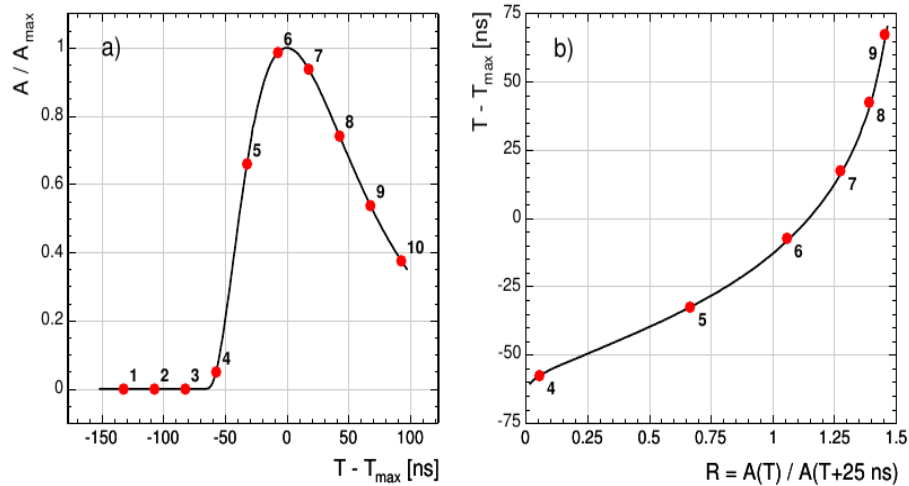


Figure 4.1: (a) A measured ECAL pulse shape for a single channel. (b)  $\mathbf{T} - \mathbf{T}_{\max}$  Vs  $R(T)$  relationship whose inverse is  $T(R)$ . Solid line is pulse shape from test beam while dots are typical 10 discrete samples corresponding to signal from proton-proton collision.

The pulse shape is used to determine  $\mathbf{T}_{\max}$  in the following way. The height ratio

$$R_i = A(T_i)/A(T_{i+1}), \quad (4.1)$$

where  $T_i$  is the time when the  $i^{\text{th}}$  pulse height sample is taken, is uniquely determined from the pulse shape. The pulse height ratio,  $R_i(T_i - T_{\max})$ , shown in Figure 4.1(b), is a function of the time that the pulse height of the first of a pair of samples is taken relative to the time of the maximum pulse height,  $\mathbf{T}_i - \mathbf{T}_{\max}$ . From the inverse of this function,  $T(R)$ , we obtain  $\mathbf{T}_{\max} = T_i - T(R_i)$  and the uncertainty,  $\sigma_i$ , for each  $R_i$  point. The uncertainty on each measurement is a product of the derivative of the function,  $T(R)$ , and the uncertainty on the value of  $R_i$  which itself depends on three separate uncertainties: the noise fluctuation ( $\sigma_n$ ) of each sample, the uncertainty in the

estimation of the pedestal value, which is always subtracted from the measured value, and the truncation during 12-bit digitization.

A precise value for  $\mathbf{T}_{\max}$  is, most of the time, obtained using the ratios  $R_4$  through  $R_7$ . The other ratios,  $R_8$  and  $R_9$  are not used for the estimation of  $T_{max}$  because their associated uncertainties are large due to the large slope of the  $T(R)$  function. A weighted average of each  $T_{max,i}$ , and  $\sigma_i$ , obtained from ratios  $R_4$  through  $R_7$  is given as

$$\mathbf{T}_{\max} = \frac{\sum \frac{T_{max,i}}{\sigma_i^2}}{\sum \frac{1}{\sigma_i^2}} , \quad \frac{1}{\sigma_T^2} = \sum \frac{1}{\sigma_i^2} \quad (4.2)$$

where the sum is from  $i = 4, \dots, 7$ , gives the best estimate of  $\mathbf{T}_{\max}$  and uncertainty.

## 4.2 ECAL Time Performance from Test Beam

### 4.2.1 ECAL Time Resolution

The intrinsic time resolution of ECAL, measured during test a beam study, can be parametrized using the standard deviation of a Gaussian distribution. It consists of three main contributions which can be summed in quadrature since they are uncorrelated. These three contributions are the noise, stochastic and constant terms. The *Noise* ( $N$ ) term arises from the electronic noise, coherent movement of the baseline and effects of overlapping hits. The *Stochastic* term ( $S$ ) arises from fluctuations in the number of photons collected during the sample times. Lastly, the *Constant* term ( $C$ ), whose contribution is independent of the energy deposited and arises from both variations in the point of shower initiation within the crystal, variations in the pulse shape for each channel and calibration effects. The full parametrization of the time resolution with all three contributions is given as

$$\sigma^2(t) = \left( \frac{N}{A/\sigma_n} \right)^2 + \left( \frac{S}{\sqrt{A}} \right)^2 + C^2, \quad (4.3)$$

where  $A$  is the measured amplitude in ADC counts corresponding to the energy deposited and  $\sigma_n$  is the intrinsic noise in the amplitude for an individual channel.  $\sigma_n$  has a value of 42 MeV and 140 MeV in the barrel and endcap, respectively.  $N = 33$  ns has

been estimated from Monte Carlo (MC) simulation studies and the contribution from the stochastic term, ( $S$ ) is small, with a value of  $S < 7.9 \text{ ns} \cdot \text{MeV}^{1/2}$ .

The measured timing resolution was obtained from the Gaussian distribution of the difference in the time of two crystals sharing energy and belonging to the same electromagnetic shower, after about 25% of the barrel and endcap crystals were exposed to electron beams with energy between 15 GeV and 250 GeV at H2 and H4 test beam facilities at CERN. This method of measuring  $\sigma(t)$  using the time difference of two crystals reduces the contribution to the constant term arising from crystal-to-crystal synchronization. And since the stochastic term is small, the parametrization of the time resolution expressed in Equation 4.3 can be reduced to

$$\sigma^2(t_1 - t_2) = \left( \frac{N}{A_{eff}/\sigma_n} \right)^2 + 2\bar{C}^2 \quad (4.4)$$

where  $A_{eff} = A_1 A_2 / \sqrt{A_1^2 + A_2^2}$ , while  $t_{1,2}$  and  $A_{1,2}$  are the times and amplitudes of the two crystals.  $\bar{C}$  is their residual constant term contribution.

In practice, the time resolution is measured from the standard deviation of a Gaussian fit to the time distribution from each slice of  $A_{eff}/\sigma_n$  of the  $A_{eff}/\sigma_n$  distribution. The resulting distribution of  $\sigma(t_1 - t_2)$  of these standard deviations plotted against  $A_{eff}/\sigma_n$  is used to extract the noise and residual constant terms. The result presented in Figure 4.2, of the test beam study gives a noise factor  $N = (35.1 \pm 0.2)$  ns which agrees with our Monte Carlo estimate to within 6%.

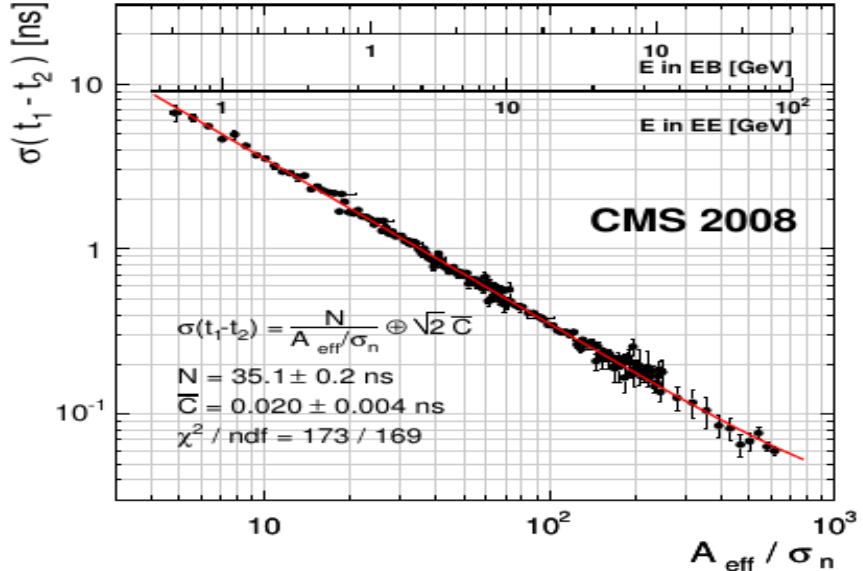


Figure 4.2: Difference in the time measurements as a function of  $A_{\text{eff}}/\sigma_n$  of two crystals sharing an energy and belonging to the same electromagnetic shower obtained during electron test beam measurements. The single crystal energy scales for barrel (EB) and endcap (EE) is overlaid. The fitted results give  $N = (35.1 \pm 0.2)$  ns and  $\bar{C} = (20 \pm 4)$  ns.

Knowing that it takes on average 4.3 ns for a photon to reach the ECAL surface produced from the proton-proton interaction point, this demonstrates an intrinsic time resolution of 2% for photons with energy  $E > 20$  GeV in the barrel.

### 4.3 ECAL Time Performance from Collision

The time resolution during LHC proton-proton ( $pp$ ) collisions is expected to be worse than what the test beam study show since the conditions during test beam are not the same as during LHC  $pp$  collisions. Effects like LHC clock time variations over extended periods, time bias with energy due to gain transitions in the front-end electronics and loss in crystal transparency due to radiation could affect the pulse shape which will ultimately worsen the ECAL time resolution. The impact of some of these effects can be minimized if all the crystals in ECAL are synchronize using events from  $pp$ .

### 4.3.1 Crystal Time Synchronization

The cause of crystal time variations may be either due to differences in pulse shape or LHC clock drift over time or time shifts introduced during CMS detector repairs. These variations of about 1 to 3 ns on average can be removed by time aligning or synchronizing all 75,848 PbWO<sub>4</sub> crystals in ECAL as the need arises. This synchronization ensures optimal timing resolution throughout the LHC stable beam collision period and continues to maintain the uniform response by all the crystals in measuring the times of electromagnetic particles produced from  $pp$  collisions. It also guarantees that the particles belonging to a given event are always assigned to the correct LHC proton bunch crossing.

Photons produced from  $pp$  collisions at the interaction point (IP), traveling along a straight path with nearly the speed of light and impinging on the front face of the crystals in ECAL are used to define the absolute zero or reference time.

The synchronization is performed at two levels. The first is by adjusting in steps of 1.04 ns the time delay of the LHC clock signal of a  $5 \times 5$  crystal matrix at the front-end electronics which make up the Clock and Control Unit (CCU). This is called *Hardware Synchronization*. The second is by adjusting the time of the individual crystals to correct for the presence of the “ $T_{max}$  Phase”, the difference in pulse shape and the different intrinsic delays in each channel. The crystal time is adjusted during event reconstruction to ensure the best timing reconstruction of each crystal and the process is called *Offline Crystal Synchronization*.

#### Offline Crystal Synchronization

The purpose of offline crystal synchronization is to compute time constants needed for the synchronization of all the crystals. Since the crystals are well synchronized if their measured average time over many events for photons produced from  $pp$  collisions at the interaction point (IP), traveling along a straight path with nearly the speed of light and impinging on the front face of the crystals is zero, this means the time constant of each crystal is taken to be the reverse sign of the mean average time measured by the crystal. To validate the crystal time constant, we expect the sum of its measured mean time and the time constant to be zero when averaged over many events. The average time and

time constant are computed using the reconstructed energy deposits (rechits) by the photon on the crystal. The time constants are produced in sets and have an *interval of validity* (IOV) which is defined by the a  $pp$  collision running period of the LHC. A total of 17 IOV sets of time constants were produced for the entire LHC run in 2011 and 44 IOV sets for 2012. Presented in Figure 4.3 and 4.4 are maps showing the average time for the 61,200 crystals in EB (top plots) and 14648 crystals in EE (bottom plots). The maps in Figure 4.3 show the average time of each crystal before synchronization. A few crystals in EB can be seen having an average time as large as  $-1.0$  ns while many in EE have average times varying from  $-1.0$  to  $+1.0$  ns, especially those in the high- $\eta$  region. The few white spots on the maps are crystals which were masked during data recording by ECAL. The mean time of the average time for all the crystals in EB is  $-0.113$  ns with an average of 205 number of rechits per crystal and  $-0.337$  ns ( $-0.346$  ns) with the number of rechits per crystal of 333 (342) for EE- (EE+). The standard deviation of the mean time for all the crystals in EB is 0.119 ns and 0.282 ns (0.256 ns) for EE- (EE+).

Figure 4.4 show the average time of the same ECAL crystals after synchronization. Most of the crystals have a mean average time of approximately 0 ns, indicating the accuracy of the time constants and performance of the synchronization. The improvement can be see in the mean time of the average time for all the crystals in EB is now  $-0.014$  ns and  $-0.003$  ns ( $-0.004$  ns) for EE- (EE+) for the same number of rechits per crystal as before synchronization. The standard deviation of the mean time for all the crystals in EB is 0.021 ns and 0.002 ns (0.021 ns) for EE- (EE+).

The details of the procedure for performing the synchronization and the results obtain for all the IOVs produced in the entire LHC Run 1 can be found in [41].

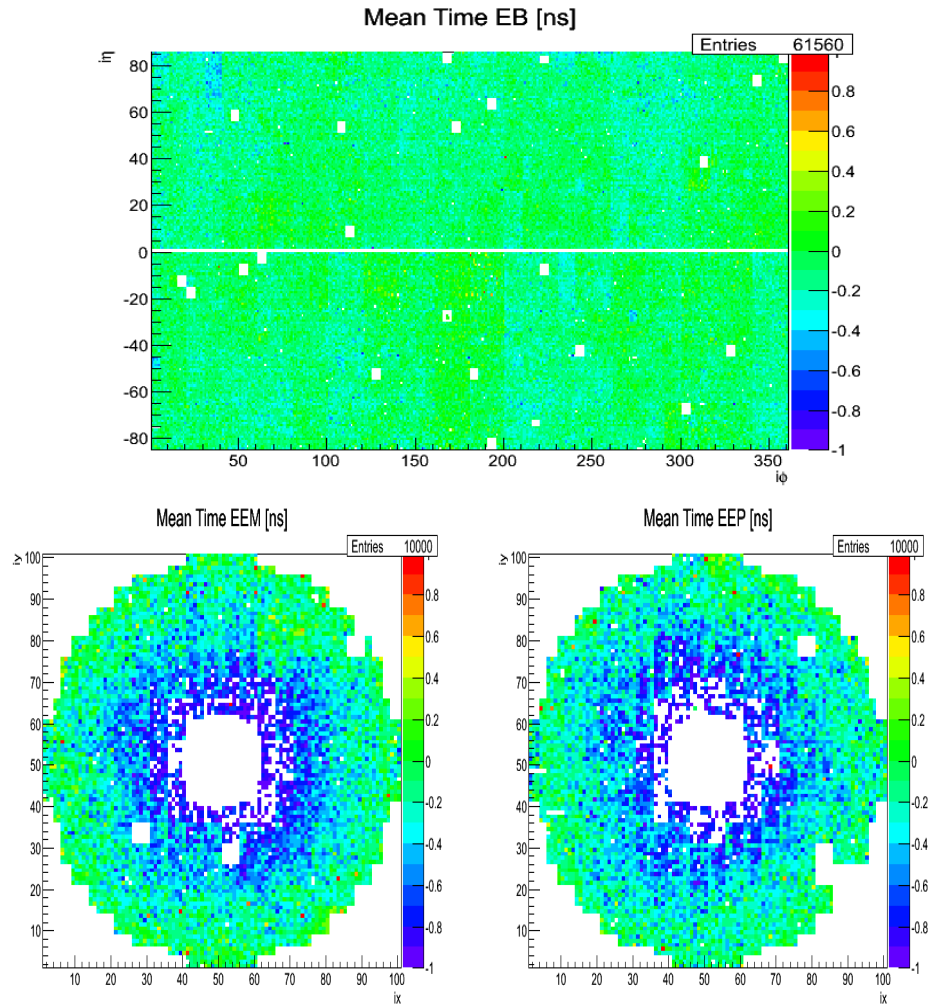


Figure 4.3: Timing maps showing the distribution of average (mean) time for each  $\text{PbWO}_4$  crystal in EB (top) and EE (below: EE- (left), EE+ (right)) before crystal synchronization.

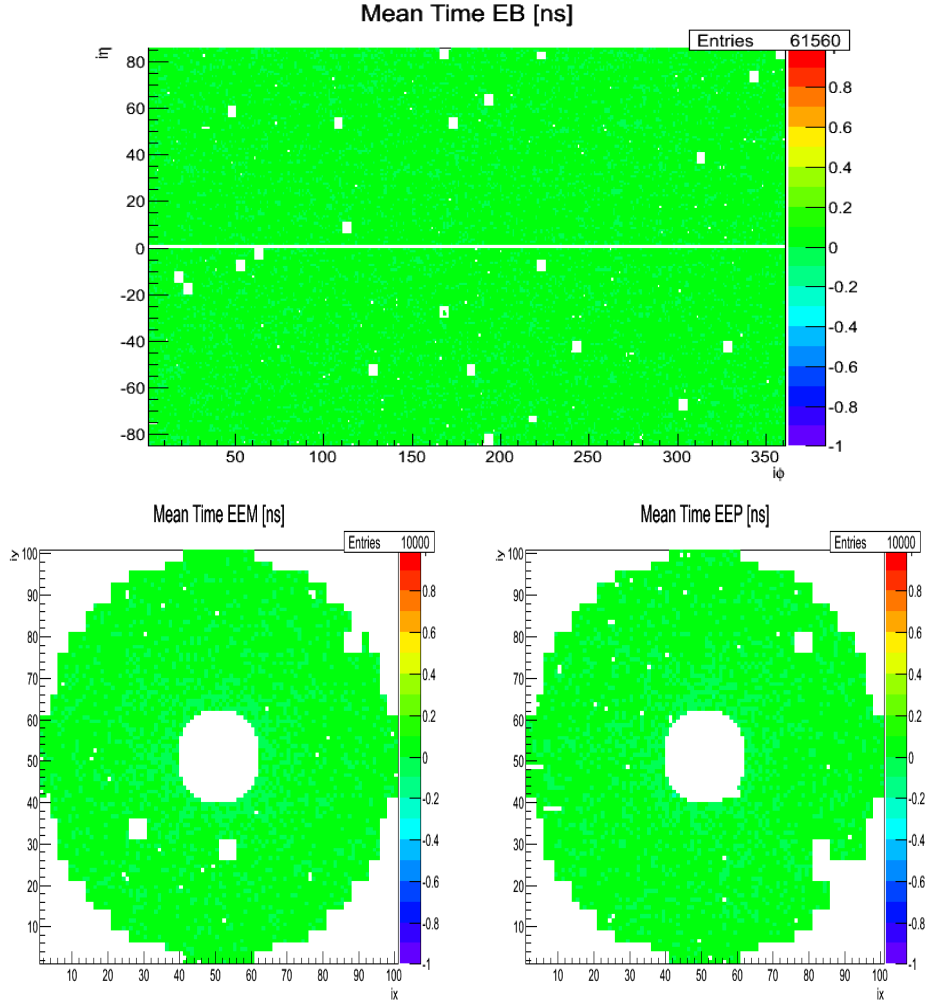


Figure 4.4: Timing maps showing the distribution of average time of each crystal after synchronization with most crystals having an average time of zero indicating the success of the crystal synchronization process and validity of the time constants.

### Hardware Synchronization

We synchronize the CCUs using histograms of the trigger tower timing from Data Quality Monitoring (DQM) services of events from  $pp$  collisions. The synchronization is often done during LHC stable proton beams and guarantees that trigger primitives are assigned to correct LHC proton bunch crossing. It is also possible to synchronize the CCUs using crystal transparency monitoring with lasers.

### Hardware Synchronization With Collision

The CCU average time is computed for events produced from  $pp$  collision and the sign of the time constants is chosen to be opposite to the offset observed from the LHC Clock drift so that their difference for each CCU is zero. During the process of synchronization, the CMS experiment experiences interruption of its data recording process during stable beams. The reason for the interruption is to update the CCUs with the new time constants before the next stable proton beams arrive. Since the CMS experiment wants to eliminate such interruptions, an alternative approach to synchronizing the CCUs is needed. This new approach, which is yet to be validated, is a laser based approach and does not require any interruption of the CMS experiment during stable beams.

### Hardware Synchronization With Laser

The ECAL laser system comprise of two lasers, a 440 nm wavelength (close to peak emission for  $\text{PbWO}_4$  crystals) laser used for monitoring crystal transparency losses and a 796 nm wavelength laser for monitoring the readout electronics chain from photodetectors to the electronics (i.e. APDs to ADCs). The timing information from the laser can be used for monitoring the Clock and Control Unit (CCU) time with the time of each crystal from laser averaged over 600 event pulses to minimize the effect of the jitter which is less than 4 ns. This crystal time is denoted as  $\mathbf{T}_{\text{MAX}}^{\text{APD}}$ . The laser system is also equipped with a fast acquisition card called MATACQ which also records the time for each crystal denoted as  $\mathbf{T}_{\text{MATACQ}}$ . This time is equally averaged over 600 event pulses. The difference,  $\mathbf{T}_{\text{MAX}}^{\text{APD}} - \mathbf{T}_{\text{MATACQ}}$ , of the two times, averaged over the 25 crystals of each CCU is used as the time for each CCU, i.e.  $\mathbf{t}_{\text{CCU}} \equiv \langle \mathbf{T}_{\text{MAX}}^{\text{APD}} - \mathbf{T}_{\text{MATACQ}} \rangle_{25}$ . To extract the time shift for each CCU, we study the change in  $\mathbf{t}_{\text{CCU}}$  before ( $\mathbf{t}_{\text{CCU}}^B$ ) and after ( $\mathbf{t}_{\text{CCU}}^A$ ) a hardware intervention during CMS machine repairs. The time difference,  $\Delta \mathbf{t}_{\text{CCU}} = \mathbf{t}_{\text{CCU}}^A - \mathbf{t}_{\text{CCU}}^B$ , averaged over the 25 crystals, i.e.  $\langle \Delta \mathbf{t}_{\text{CCU}} \rangle_{25}$ , gives the time shift, and the time constant for the CCU is the opposite sign of  $\langle \Delta \mathbf{t}_{\text{CCU}} \rangle_{25}$ , so that the sum of the CCU time shift and its time constant is on average zero. The CCU synchronization is done for all the 68 CCUs in a given supermodule (SM) or front-end-detector (FED). The effect of any global time shift of a given FED caused by the non-homogeneous laser light distribution on all the CCUs is also taken into account in the synchronization process if present. Each FED has 1,700  $\text{PbWO}_4$  crystals, thus 68

timing constants are needed per FED. Detail information on hardware synchronization using laser monitoring can be obtained from here [42].

### 4.3.2 Time Bias

The time reconstruction algorithm assumes the reconstructed time does not depend on the energy of the incident particle. However, it was observed during CMS data recording in LHC Run 1 that for very energetic particles (energy above 130 GeV in EB and 250 GeV in EE, an inherent bias in the time is introduced by the multi-gain pre-amplifier electronics at gain transition points due to not-quite-high-enough slew rate of the amplifiers. The time bias was also observed for very low energy values of less than 2 GeV. The first gain transition from gain-12 to gain-6 of the multi-gain pre-amplifier occurs near 159.744 GeV in EB and 258.048 GeV in EE. The next gain transition is from gain-6 to gain-1 and occur at energies of about TeV.

We correct the energy dependence timing bias on a rechit energy basis during event reconstruction. The corrections were applied depending on a CMS event reconstruction software (CMSSW) release version to account for different CMS data recording and event reconstruction conditions. In Figure 4.5 we show a comparison of the performance of the time bias corrections on the average time against rechit energy during the reconstruction of rechits between two CMS event reconstruction software releases. In CMSSW44X (left plot), the time bias corrections made previously did not perform as expected while in CMSSW53X (right plot) after the second set of time bias corrections were made, the average time is flat with energy. This flatness is seen even for the different modules 1 through 4 (modules contain crystals for different regions in EB) in the barrel.

The standard deviation on the time against rechit energy in plots CMSSW44X (left) and CMSSW53X (right) of Figure 4.6, show that despite the timing bias corrections, the standard deviation does not change in both CMSSW software releases. This is as expected since the ability to measure the arrival time should not depend on the choice of the reference time.

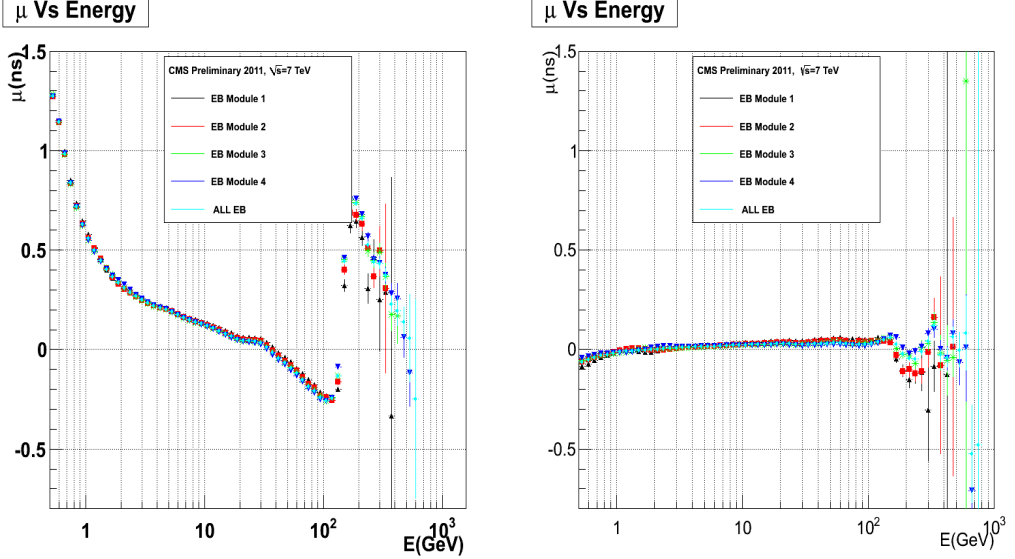


Figure 4.5: Average time ( $\mu$ ) against rechit energy for EB. The first gain transitions (gain-12 to 6) happens at about 130 GeV and time bias on energy is seen in CMSSW44X (left) and very little in CMSSW53X (right) where the corrections have been applied during rechit reconstruction.

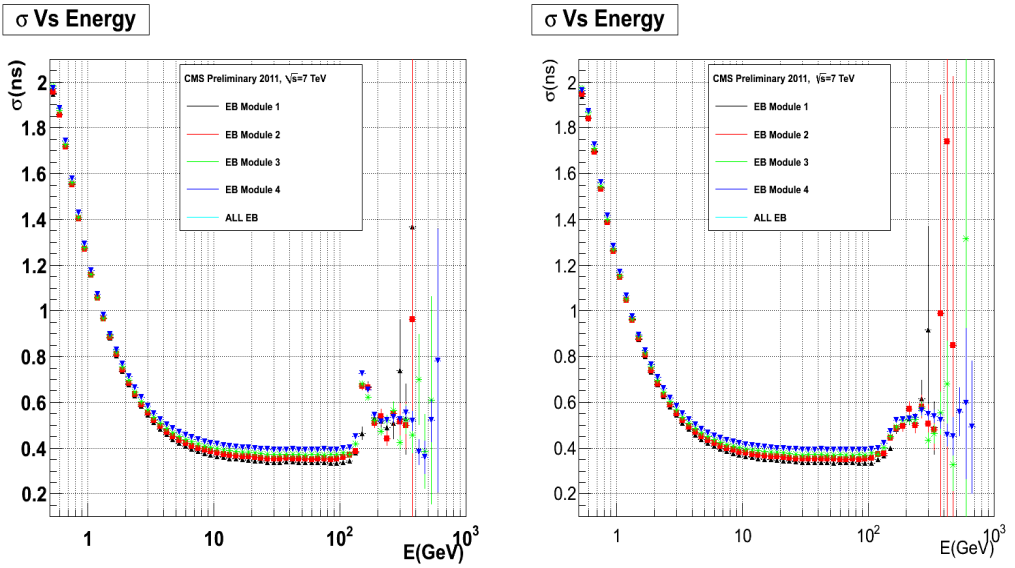


Figure 4.6: The standard deviation against rechit energy for EB in CMSSW44X (left) and CMSSW53X (right). The time bias corrections don't affect the standard deviation on the time.

## 4.4 ECAL Time Performance With Z Bosons

We evaluate the precision of ECAL timing measurements, during  $pp$  collisions, by studying the electron time measurements of events with the decay of the Z boson, i.e.  $Z \rightarrow e^-e^+$ . The selection for Z candidate events require that each electron have transverse energy above 10 GeV and the reconstructed Z mass is within,  $60\text{ GeV}/c^2 < m_{e_1,e_2} < 120\text{ GeV}/c^2$ , to ensure that the sample contains mostly good Z candidates.

We use the standard deviation,  $\sigma_{eff}$ , of the difference in arrival time of the two electrons to evaluate ECAL timing performance. This standard deviation is obtained from the difference in the seed time,  $t_{seed}$ , of each electron's electromagnetic shower after correcting for the extra time due to the bending of the electron's travel path inside the CMS magnetic field of 3.8 T. Figure 4.7 shows the distribution of the time difference,  $t_{electron1} - t_{electron2} \equiv t_{seed1} - t_{seed2}$ , and the value of the time resolution ( $\sigma_{eff}(t_1 - t_2)$ ) of both electrons after adjusting the time due to its non-straight time of flight path, and in Figure 4.8, we show the *absolute time resolution* ( $\sigma_{eff}(t_{seed})$ ), obtained from the time distribution of a single electron's seed crystal time after adjusting for the time due to the bending of the electron's flight path.

A time resolution of 0.232 ns in EB and 0.384 ns in EE is measured with a *single crystal precision resolution* ( $\sigma_{eff}(t_1 - t_2)/\sqrt{2}$ ) of 0.164 ns in EB and 0.272 ns in EE presented in Table 4.1.

The absolute time resolution,  $\sigma_{eff}(t_{seed})$ , for a single crystal is measured to be 0.386 ns for EB and 0.388 ns for EE. However, if we remove the contribution from the spread in time,  $\sigma(t_{colision})$ , due to the finite time it takes for the two proton bunches of length 5.5 cm to collide; which is about  $\sigma(t_{colision}) = \sigma(t_Z) = 0.183$  ns, we get an improvement in absolute time resolution which is 0.340 ns in EB and 0.342 ns in EE.

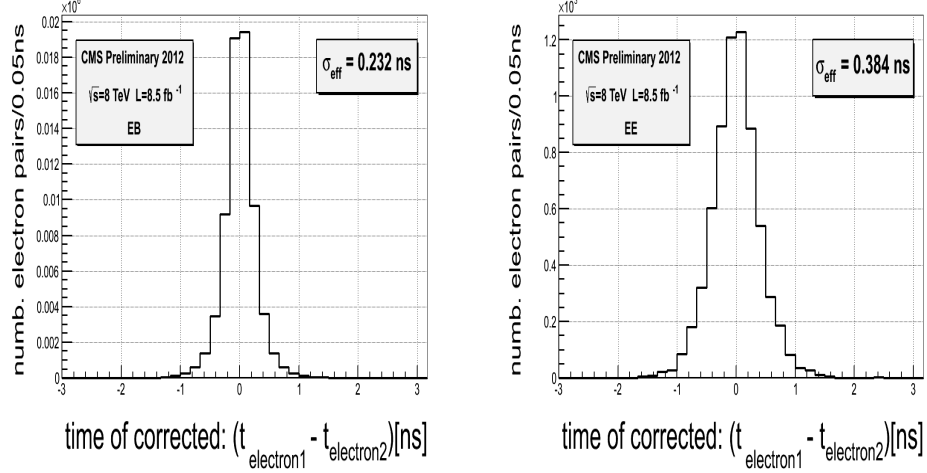


Figure 4.7: Time difference between the two reconstructed electrons in  $Z \rightarrow e^-e^+$  decay. The electron time is the seed (crystal with highest energy deposit) time with additional correction due to the time of flight of the electron in EB and EE.

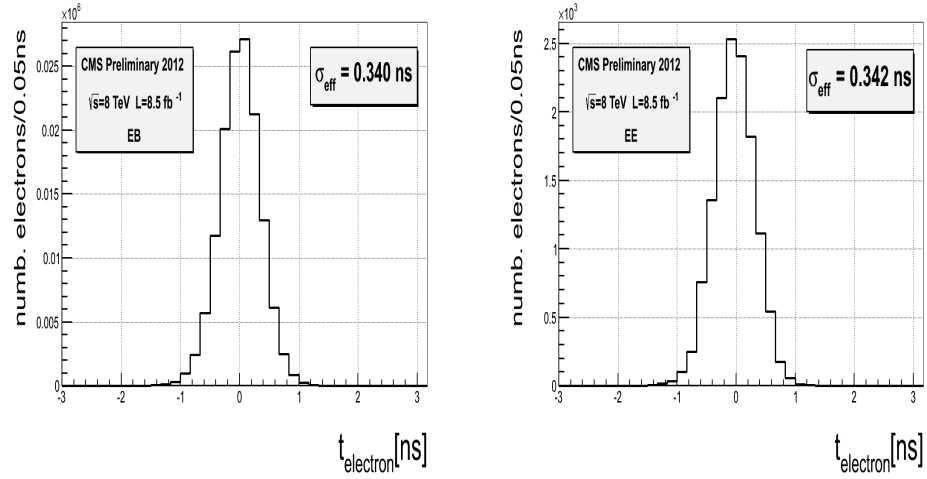


Figure 4.8: Absolute time of a single reconstructed electron in  $Z \rightarrow e^-e^+$  decay. The electron time is the seed (crystal with highest energy deposit) time of the electron in EB and EE.

We also investigate the timing bias attributed to the FE electronics using events with  $Z \rightarrow e^-e^+$  decay. Figure 4.9 (left) show the time resolution measured in the case where the seed crystal time is reconstructed from the same FE electronics compared to

the other case, shown in Figure 4.9 (right), where the seed crystal time is reconstructed from different FE electronics. The Constant term,  $C$ , for the same FE electronics is about 0.067 ns while that for different FE electronics is 0.130 ns, which indicates that the differences in electronic readout de-synchronization among different FE contributes to the worsening of the time resolution [43, 44, 45, 46, 47].

The ECAL time resolution for the entire LHC Run 1 of 2011 and 2012, comparing the absolute and single precision time measurements is summarized in Table 4.1. However, the source of approximately 0.400 ns limit in the improvement of the time resolution remains to be understood. We can only speculate that a combination of effects like pulse shape differences caused by loss of crystal transparency, fluctuations in the shower development in the crystals especially for energetic electromagnetic particles, about 0.100 ns differences arising from the differences in FE electronics de-synchronization among different electronics and phase shifts in the LHC clock phase lock by the QPLL. Additional studies are needed to fully understand and quantify the contributions from each of these sources.

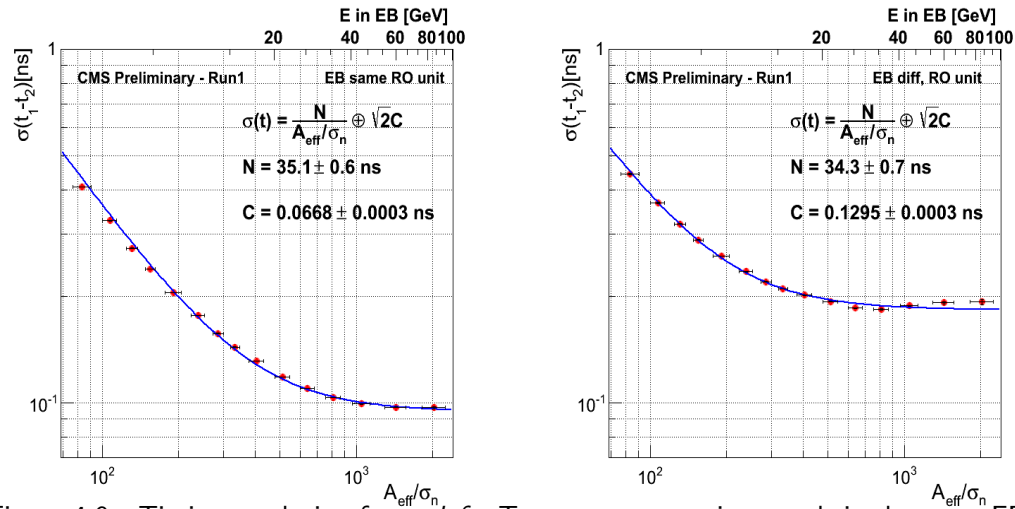


Figure 4.9: Timing resolution from: *left*: Two most energetic crystals in the same FE electronics, *right*: Two most energetic crystals belonging to different FE electronics, as a function of effective amplitude( $A_{eff} = A_1 A_2 / \sqrt{A_1^2 + A_2^2}$ ) normalized to noise in EB. Both crystals are from reconstructed electrons in  $Z \rightarrow e^- e^+$  events.

**ECAL Timing Resolution**

<b>2011</b>		
	<b>Absolute Time</b>	<b>Single Precision</b>
	$\sigma_{eff}(t_{seed})[\text{ps}]$	$\sigma_{eff}(t_{e1} - t_{e2})[\text{ps}]$
<b>EB</b>	376	190
<b>EE</b>	356	282
<b>2012</b>		
	<b>Absolute Time</b>	<b>Single Precision</b>
	$\sigma_{eff}(t_{seed})[\text{ps}]$	$\sigma_{eff}(t_{e1} - t_{e2})[\text{ps}]$
<b>EB</b>	340	164
<b>EE</b>	342	272

Table 4.1: ECAL timing resolution absolute time and single precision for 2011 and 2012 of LHC Run 1.

# Chapter 5

## Event Reconstruction

### 5.1 Event Reconstruction Overview

Event reconstruction is the process of reconstructing particles and their four momenta using raw data read from the electronics of the different CMS subdetectors. Event reconstruction is archived in CMS using the *Particle Flow* (PF) algorithm which reconstructs all the particles in an event, individually, using information from all CMS subdetectors. It is also possible to reconstruct particles without using the PF algorithm.

### 5.2 Supercluster Reconstruction

A clustering algorithm groups energy deposits from individual crystals to form clusters which are eventually grouped together forming clusters of clusters known as *superclusters*. A cluster is either a  $3 \times 3$  or  $5 \times 5$  crystals energy matrix. About 94% (97%) of the incident photon or electron energy is deposited in the  $3 \times 3$  ( $5 \times 5$ ) crystal matrix in  $(\eta, \phi)$  directions in the barrel and  $(x, y)$  directions in the endcaps.

The 3.8 T magnetic field and material in front of the calorimeter causes electrons and photons radiating off electrons to deposit their energy in a cluster of crystals spread in  $\phi$  and because of the spread in  $\phi$ , the clustering algorithms starts building clusters with a seed crystal (crystal with the maximum energy) and continues within a narrow window in  $\eta$  by summing the crystal energies along  $\phi$ , which is the direction of the energy spread due to the magnetic field. Figure 5.1 is a schematic picture showing the direction (left

Figure) of the clustering process in  $(\eta, \phi)$  directions in the barrel and the fraction (right Figure) of electromagnetic energy in a typical cluster.

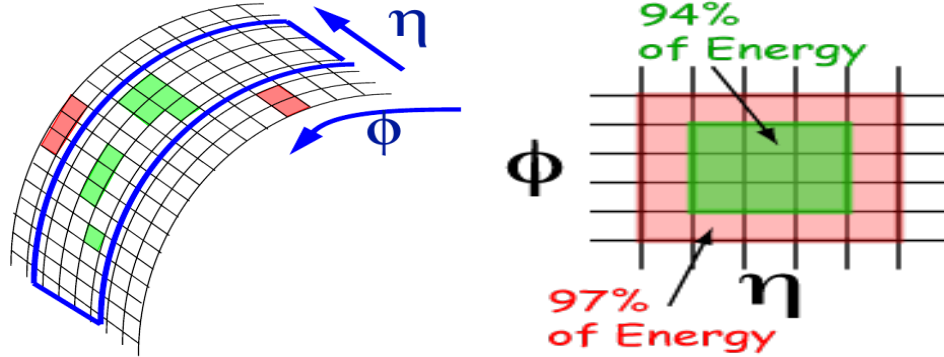


Figure 5.1: Superclustering algorithm direction (left) in the  $(\eta, \phi)$  plane in EB and fraction (right) of electromagnetic shower energy coverage in a crystal energy matrix.

Two major clustering algorithms are used in ECAL: the *hybrid* (EB) and *island* (EE) algorithms.

- **Hybrid Supercluster Algorithm:** This algorithm is used for making super clusters in the barrel (EB). It takes advantage of the  $\eta - \phi$  geometry of barrel crystals by taking a fixed 3 or 5 crystals in  $\eta$  and dynamically search and sum separate crystals energy along  $\phi$ . The Hybrid algorithm takes advantage of the knowledge of the lateral shower shape along the  $\eta$  direction. The supercluster consists of basic clusters which are usually  $3 \times 3$  crystals energy matrix.
- **Island Supercluster Algorithm:** This algorithm is used for making clusters in the endcap (EE). It begins by finding the seed crystal of the electromagnetic shower with maximum energy above a certain energy threshold. Using the seed crystal position, adjacent crystals are examined and added to a cluster until a rise in energy where a crystal belonging to another cluster or crystal that has no energy hit is reached. For each crystal to be added to the cluster, its energy read must be positive, it must not have been assigned to another cluster and the previous crystal added in the same direction must have a higher energy. These non-overlapping clusters (usually a  $5 \times 5$  crystals energy matrix) finally form a supercluster.

### 5.3 Track and Vertex Reconstruction

The track of a charge particle is reconstructed using *hits* which are themselves reconstructed from the ionization left in silicon by the passage of the charge particle. The particle's helical trajectory or track, reconstructed from these hits, is used to measure the it's momentum and direction.

Track reconstruction uses several algorithms with the main algorithm used for reconstructing the tracks of charge particles produced from  $pp$  collisions called the *Combinatorial Track Finder* (CTF). The CTF integrates track fitting and pattern recognition, building tracks from an initial trajectory or seed while taking into account the energy loss and multiple-scattering between the tracker detector layers. It proceeds in three stages: seeding, finding and fitting.

During the seeding, initial trajectories (seeds) made of a pair of pixel hits that are compatible with the beam spot and have a lower  $p_T$  limit are used as possible candidates of the charge tracks. Pixel hits are the best track seeds while in the more forward region of the tracker detector,  $2 < |\eta| < 2.5$ , silicon pixel and inner strips hits are used for better track seeding.

The track finding stage uses a *Kalman Filter* pattern recognition approach (since the tracks can be described as a discrete dynamic *track state*, characterized by some given set of parameters and uncertainties, which is recursively updated one hit at a time on each layer) where, starting with the track parameters determined by the seeds, the track trajectory is extrapolated to outer neighboring tracker layers and compatible hits are assigned to the track.

In the fitting stage, the Kalman Filter algorithm (because the position information of the hit is updated to estimate the track parameters and uncertainties and the fitting process is repetitive) is again applied where each candidate track is fitted using least-squares fitting in two stages. The first stage avoids possible bias on the track parameters from the initial trajectories used in the seeding stage while the next stage yields the best estimates of the track parameters and uncertainties at the original vertex.

Other algorithms like the *iterative tracking algorithm* which is a general purpose tracking algorithm is used in association with customized CTF tracking algorithm to reconstruct the tracks of non-collisions events like cosmic and beam halo.

Similar to track reconstruction, vertex reconstruction involves two stages: vertex finding and vertex fitting. During vertex finding, a set of valid tracks from track reconstruction, represented by a list of track parameter vectors, is fed into a vertex finding algorithm which classifies the tracks into vertex candidates. The type of vertex finding algorithm used depends on whether it is finding a primary vertex (vertex where the particles are produced from the collision of the two proton beams) or secondary vertex (vertex where the particles are produced from the decay of an unstable particle) or the reconstruction of an exclusive particle decay.

The classified vertex candidates from vertex finding are fed into the vertex fitting algorithm. The output of the vertex fitting is a list of vertices, with each vertex having an estimated vertex position and a set of updated track parameter vectors. In vertex fitting, the best estimates of the vertex parameter, co-variance matrix, track parameter and the fit quality (chi-square, number of degrees of freedom, track weights) are used in distinguishing among a given set of tracks and their vertices.

## 5.4 Photon and Electron Reconstruction

Photons are reconstructed using superclusters and since they are neutral and do not leave tracks in the tracker, they are identified as superclusters in ECAL not associated to any tracks or reconstructed hits in the pixel tracker. The photon identification, beyond simply using the ECAL supercluster, is improved through several selection requirements using information from the tracker, ECAL, HCAL and the ratio of the photon candidate's energy deposited in HCAL to ECAL. Photons are supposed to deposit very little or no energy in HCAL and this is one of the main selection requirements to help distinguish photons from hadronic jets with high electromagnetic energy fraction which can easily be misidentified as photons.

For electron reconstruction, electron candidates are found when a supercluster is associated to a track reconstructed in the silicon tracker detector and in particular, its inner most layers (pixel hits). Electron reconstruction begins with a seeding approach which is either driven by ECAL or by the tracker. The ECAL driven seeding approach is very efficient for electrons with  $p_T > 10 \text{ GeV}/c$ . The track driven seeding approach uses a boosted decision tree to perform a pre-selection of the tracker clusters, in order to reduce

fake electrons which are light hadrons with many hits in the tracker. Low- $p_T$  electrons and non-isolated electrons (electrons embedded in jets) are reconstructed efficiently using the tracker driven seeded approach, since most of their energy is deposited in the tracker and very little in the ECAL, as they lose most of their energy through multiple scattering before they reach ECAL. When fitting the electron tracks, we must account for the different energy loss mechanisms of the electron compared to other charged particles. Since electrons lose most of their energy by radiating photons (*bremsstrahlung*, which is non-Gaussian in nature, the *Gaussian Sum Filter* algorithm (combination of several Gaussians) is used to provide good estimate of the track momentum both at the ECAL surface and at the interaction point.

## 5.5 Muon Reconstruction

Muon tracks are reconstructed using the all-silicon inner tracker (tracker tracks) and the muon system (standalone tracks). The standalone tracks are reconstructed using reconstructed positions (hits) in the muon system consisting of the Drift Tubes (DT) in the barrel ( $|\eta| < 0.9$ ), Cathode Strip Chambers (CSC) in the endcaps ( $1.2 < |\eta| < 2.4$ ) and Resistive Plate Chambers (RPC) in the overlap region ( $0.9 < |\eta| < 1.2$ ). There are two independent muon reconstruction approaches: *Global muon reconstruction (Outside-in)* and *Tracker muon reconstruction (Inside-out)*. For Global muon reconstruction, each standalone-muon track is matched to a tracker track by comparing the parameters of the two tracks propagated to a common surface. The global muon track is fitted combining hits from the tracker track and standalone-muon track using the Kalman-filter algorithm. For the tracker muon reconstruction, all tracks with  $p_T > 0.5 \text{ GeV}/c$  and total momentum  $p > 2.5 \text{ GeV}/c$  are considered as possible muon candidates and are extrapolated to the muon system taking into consideration the magnetic fields, the average expected energy loss in the calorimeters and multiple Coulomb scattering in the detector material to locally reconstruct segments in the muon system. A combination of different muon algorithms depending on the muon  $p_T$ , provides a robust and efficient muon identification.

Using the beam spot as constraint for the muon's vertex, we can distinguish between muons produced from  $pp$  collisions from *cosmic muons* and *beam halo muons* (muons

produced from the interaction of the proton beam with the gas in the beam pipe). Figure 5.2 show an illustration of the trajectories of different muon sources interacting with the CMS detector.

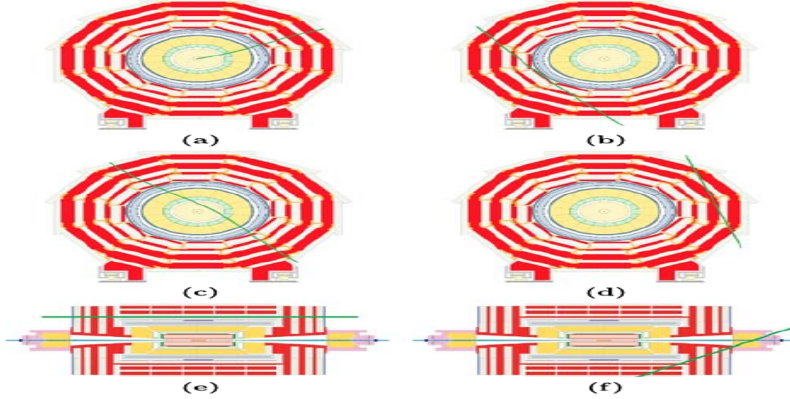


Figure 5.2: Illustration of muons from proton-proton collision, cosmic rays and beam halo. (a) Muons from collision propagating from the center and moving outwards, (b) Cosmic muons traveling through the detector leaving signals in opposite hemispheres of the muon system, (c) Cosmic muons leaving signals in the tracker and opposite hemispheres, (d) cosmic muons entering and leaving the detector without passing through the muon detector layers, (e) beam halo muons penetrating the detector and leaving signals in the endcaps and (f) Cosmic muons entering the detector through the endcap (EE) and leaving through the barrel (EB). This can happen in the reverse way; EB to EE.

## 5.6 Particle Flow Algorithm

The *Particle Flow* (PF) algorithm is an algorithm for reconstructing particles using detector information from the tracker, ECAL, HCAL and muon chambers of the CMS detector [48, 49]. It uses a combination of different algorithms comprising of calorimeter clustering, tracking and extrapolation to calorimeters, muon identification, electron pre-identification and linking local reconstructed elements, for reconstructing a list of particles which include photons, charge hadrons, neutral hadrons, muons and electrons. The same list of particles is subsequently used to reconstruct composite “particles” like jets,  $E_T^{\text{miss}}$  and taus. The versatility of the PF algorithm is the reason why it was introduced for reconstructing Jets and missing transverse energy ( $E_T^{\text{miss}}$ ), where complete information of the event content from every subdetector is needed for best performance.

The PF algorithm uses tracks, electron energy seeds, 4-momentum, super cluster energy calibration, bremsstrahlung tracks for electron and photon reconstruction making it extremely efficient at minimizing electron and photon misidentification. For  $E_T^{\text{miss}}$  reconstruction where full reconstruction of all the particles belonging to an event is necessary, the PF algorithm is very reliable.

## 5.7 Jet Reconstruction

A jet is a spray of particles arising from the hadronization of colored particles. Because jets are made of many particles like hadrons and photons from  $\pi^0$  decay, they are best reconstructed using the particle flow algorithm. Jets reconstructed using the PF algorithm are called *PF-Jets*.

Using calorimeter towers as input, jets can be reconstructed using the Anti- $k_T$  clustering algorithm which combines four vectors according to their relative transverse momentum ( $p_T$ ) within a standard cone size of  $\Delta R = 0.5$  in the  $(\eta, \phi)$  plane, where,  $\Delta R = \sqrt{\Delta\eta^2 + \Delta\phi^2}$ .

The quality of a reconstructed jet depends on a set of selection variables collectively referred to as the *JetID*. The JetID consist of variables which selects on jets candidate base on the composition of the jets. The jet composition can be described using the following quantities: electromagnetic energy fraction (EMF), the charge hadron fraction (CHF), the neutral hadron fraction (NHF), the charge electromagnetic fraction (CEF), neutral electromagnetic fraction (NEF) the number of calorimeter cells containing more than 90% of jet energy ( $N_{jet}^{90}$ ), the fraction of jet energy in the hottest Hybrid photodetector (HPD) unit in HCAL readout within a jet ( $f_{HPD}$ ) and the  $\eta$  region of the jet. The selection threshold and combination of jetID variables used will depend on a specific analysis and the type of jets involved. In general, jet candidates are required to have an electromagnetic energy fraction (EMF) more than 10% i.e.  $EMF > 0.01$ , must be within the ECAL fiducial region of  $|\eta| < 2.6$ , the number of calorimeter cells containing more than 90% of jet energy ( $N_{jet}^{90}$ ) must be  $> 1$ , the fraction of jet energy in the hottest Hybrid photodetector (HPD) unit in HCAL readout within a jet ( $f_{HPD}$ ) must be  $> 0.98$ , the charge hadron fraction (CHF)  $> 0.0$  if within  $|\eta| < 2.4$ , the neutral hadron fraction (NHF)  $< 1.0$ , the charge electromagnetic fraction (CEF)  $< 1.0$ , and

neutral electromagnetic fraction ( $NEF$ )  $< 1.0$ . These jetID selection requirements have been shown to remove mis-reconstructed jets arising from spurious energy deposition in subdetectors with good efficiency [50].

The jet energy is often mis-measured due to non-linear responses in the calorimeters as the hadronic shower develops, cracks in the detector and additional energy from events with PU. The jet energy is corrected for contributions from the above sources through *Jet Energy Corrections* (JEC) measurements [51]. Applying these corrections during reconstruction guarantee a reliable measurement of the jet energy , however, JEC is one of the sources of uncertainties in most analysis which involve jets.

## 5.8 Missing Transverse Energy Reconstruction

Missing Transverse Energy is defined as the negative vector sum of the transverse energy deposits of all the particle candidates in an event, including the JEC. Its magnitude,  $E_T^{\text{miss}}$  is given as

$$E_T^{\text{miss}} = \left| - \sum_n (E_n \sin \theta_n \cos \theta_n \hat{\mathbf{i}} + E_n \sin \theta_n \sin \theta_n \hat{\mathbf{j}}) \right| = |\not{E}_T^x \hat{\mathbf{i}} + \not{E}_T^y \hat{\mathbf{j}}| \quad (5.1)$$

Where,  $n$  is the sum over all calorimeter energy deposits including energy deposits in towers, reconstructed energies (hits) or generator level particle energies.  $E_T^{\text{miss}}$  is used to infer the presence of a particle which escaped the CMS detector like neutrinos ( $\nu$ ), neutralinos ( $\tilde{\chi}_1^0$ ) and gravitino ( $\tilde{G}$ ).

In order to measure  $E_T^{\text{miss}}$  accurately, a particle detector should be nearly hemispherical i.e. have a  $4\pi$  solid angle coverage, to allow for complete measurement of the transverse momentum of all the particles belonging to an event. The hadronic forward (HF) subdetector of the CMS detector, with little space allowing for the passage of the proton beams, provide this near  $4\pi$  solid angle.

Measuring  $E_T^{\text{miss}}$  is always challenging and is a source of uncertainty in most analysis which involve  $E_T^{\text{miss}}$  as machine induced background processes, mis-measured energy of and from mis-reconstructed particles and anomalous signals like spike can contribute to the measurement of  $E_T^{\text{miss}}$ . By minimizing the contributions from these processes we can measure  $E_T^{\text{miss}}$  better [52, 53].

The use of  $E_T^{\text{miss}}$  in event selection is common in most analysis which involves the search for new phenomena which is a common prediction in models Beyond Standard Model (BSM) like *supersymmetry*. The presence of large  $E_T^{\text{miss}}$  in an event indicates the presence of a new particle not described by standard model interactions which usually have small  $E_T^{\text{miss}}$  as in the case of the neutrino in the W boson decay,  $W \rightarrow e + \bar{\nu}$ .

## 5.9 Anomalous Signals

Sometimes anomalously large signals called “*spikes*” are produced when neutrons or charged hadrons like protons strike directly, ionizing the silicon of the photodiode producing an electronic signal even in the absence of any crystal scintillation.

Because spike signals are not produced through the crystal scintillation process, which takes about 10 ns, their measured arrival time is early and negative. Energy deposits from spikes range from a few GeV to the saturation energy of ECAL which is about 1.7 TeV. Since they are not due to showering particles, most often only one isolated crystal sees such energy. Spikes may occasionally have positive time, appearing late or delayed in their arrival time at ECAL, and populating the tails of the photon’s rechit time distribution. The late arrival time may be due to the slow propagation (takes an indirect route) of neutrons through the CMS detector.

Numerous test beam, collision data and simulation studies [54, 55], have been carried out towards understanding the properties of events with spikes and how they can be tagged and removed. These studies reveal that most spikes can be identified using a topological energy sharing variable called “*Swiss-Cross*” (SX) constructed as  $1 - \frac{E_4}{E_1}$ .  $E_1$  is the energy deposit of the central (highest energy) crystal and  $E_4$  is the sum total of the energy of the neighboring four crystals in the  $(\eta, \phi)$  plane. A selection cut  $\text{SX} > 0.95$  rejects more than 99% of isolated spikes with transverse energy greater than 10 GeV with very little impact on the efficiency of selecting electromagnetic (EM) showers. Other topological energy sharing variables like  $1 - \frac{E_6}{E_2}$  and  $1 - \frac{E_9}{E_2}$ , where  $E_2$  is the sum of the energy of two crystals sharing the energy deposited from simultaneous spikes and  $E_6(E_9)$  is the sum of the neighboring 6(pairs-of)(9) crystals in the  $(\eta, \phi)$  plane. The  $1 - \frac{E_6}{E_2}$  variable is used to identify isolated spikes whose energy deposit spread in two adjacent crystals while the  $1 - \frac{E_2}{E_9}$  is used to identify non-isolated spikes i.e. spikes which

are found embedded in a supercluster.

It has also been shown that applying selection cuts on the rechit time of  $\pm 3$  ns leads to more than 90% efficiency for rejecting spikes. However, in this thesis, we do not require such selection cuts on the rechit time as these rechits include rechits of possible delayed electromagnetic particles produced during  $pp$  collisions with arrival time beyond 3 ns.

## Chapter 6

# Search Analysis for Long-Lived Neutral Particles

### 6.1 Analysis Strategy

The search for a Long-Lived Neutral Particle in final state with at least one late photon and large Missing Transverse Energy ( $E_T^{\text{miss}}$ ) is described. The photon arrival time is measured using the Electromagnetic Calorimeter (ECAL). We use a counting method to perform the search where an excess number of events with photon time above a timing threshold over the expected number of background events indicates the presence of a new physics phenomenon like the decay of the lightest neutralino into a late photon and a gravitino. Since a final state with at least a late photon and large  $E_T^{\text{miss}}$  is difficult for standard model interactions to mimic, we expect most of the background events to arise from processes other than proton-proton ( $pp$ ) collision events.

#### 6.1.1 Signal and Background Events

The decay of the lightest neutralino ( $\tilde{\chi}_1^0$ ) to a late photon ( $\gamma$ ) and gravitino ( $\tilde{G}$ ),  $\tilde{\chi}_1^0 \rightarrow \gamma + \tilde{G}$ , gives rise to events whose final state consist of a late photon and large  $E_T^{\text{miss}}$  due to the undetected gravitino ( $\tilde{G}$ ) and since the  $\tilde{\chi}_1^0$  is produced from the cascade decay of heavier supersymmetric particles like gluino ( $\tilde{g}$ ) or squark ( $\tilde{q}$ ), i.e.  $gg \rightarrow \tilde{g}\tilde{g} \rightarrow q\bar{q}q\bar{q}\tilde{\chi}_1^0\tilde{\chi}_1^0$  or  $q\bar{q} \rightarrow \tilde{q}\bar{\tilde{q}} \rightarrow \bar{q}q\tilde{\chi}_1^0\tilde{\chi}_1^0$ , we expect the final state of a signal event to include multiple

high- $p_T$  jets. Thus, the final state of a typical signal event comprises of at least one late high- $p_T$  photon, large  $E_T^{\text{miss}}$  and multiple high- $p_T$  jets. The multiple high- $p_T$  jets provides an additional handle during event selection to help suppress background events with no jets.

If at all there are any background events with a similar final state to the signal event, they must be atypical events with late photons, large  $E_T^{\text{miss}}$  and jets in the final state produced from either  $pp$  collisions or some other source(s) which we refer to as *non-collision*.

These non-collision background events include the so-called proton *Beam Induced Backgrounds* or beam halo, cosmic rays and spikes.

The background events produced from  $pp$  collisions (collision background events) that can emulate signal events are those events for which the photon time and/or  $E_T^{\text{miss}}$  are mis-measured or those events produced from satellite bunch crossings described in section 3.1.4 which have late photons in the final state. Other collision events that could have real  $E_T^{\text{miss}}$  and a misidentified photon in the final state include: inclusive Z+jets/W+jets events, inclusive top-anti-top ( $t\bar{t}$ )+jets events and inclusive ZZ/WW/WZ+jets events which have true  $E_T^{\text{miss}}$  through the  $Z \rightarrow \nu\bar{\nu}$  and  $W \rightarrow e\bar{\nu}_e$  decays with the undetected neutrino ( $\nu$ ) giving rise to  $E_T^{\text{miss}}$ . Multijets and QCD events on the other hand give rise to fake  $E_T^{\text{miss}}$  (instrumental  $E_T^{\text{miss}}$ ), where an undetected particle is not part of the event but the  $E_T^{\text{miss}}$  arises due to poor reconstruction of the energies of the particles. The late photon arises when one of the jets or an electron is misidentified as a photon and its ECAL time is mis-measured. The other jets in the event might satisfy the high- $p_T$  multiple jets requirement.

### 6.1.2 Samples

#### Datasets

The data sample used for this search was recorded by the CMS detector and is equivalent to a total integrated luminosity of  $19.1 \text{ fb}^{-1}$ . It contains events passing an HLT trigger which requires that at least one photon belongs to the final state. These events were produced during LHC Run 1  $pp$  collisions at the center of mass energy,  $\sqrt{S} = 8 \text{ TeV}$ .

## Monte Carlo Samples

The MC samples are made with *Summer 2012* prescription of the calibration and alignment status of the CMS detector and pile up conditions at 8 TeV.

The SPS8 benchmark GMSB samples are produced for different mean lifetime ( $c\tau$ ) of the lightest neutralino ( $\tilde{\chi}_1^0$ ) ranging from 500 mm ( $\tau = 1.7$  ns) to 10000 mm ( $\tau = 33.3$  ns) for each effective SUSY breaking scale ( $\Lambda$ ) or mass of the lightest neutralino ( $m_{\tilde{\chi}_1^0}$ ) point. We vary  $\Lambda$  from 100 TeV to 220 TeV which is equivalent to  $m_{\tilde{\chi}_1^0}$  ranging from  $139 \text{ GeV}/c^2$  to  $314 \text{ GeV}/c^2$ . Each sample has 50,000 events for each  $c\tau$  and  $\Lambda$ . Table 6.1 shows a summary of our signal MC samples used where for each sample, equally given is the number of events, cross-section and branching ratio for  $\tilde{\chi}_1^0$  production and decay to  $\gamma$  and  $\tilde{G}$  for each  $\Lambda$ .

The  $\gamma$ +jet MC samples were generated for different momentum of the colliding parton ( $\hat{p}_T$ ) and normalized to the  $19.1 \text{ fb}^{-1}$  of integrated luminosity. The cross-sections, momentum of the colliding parton and the number of events in each sample is summarized in Table 6.2. The  $\hat{p}_T$  range is from  $50 \text{ GeV}/c$  to  $800 \text{ GeV}/c$ .

$\Lambda$ [TeV]	$m_{\tilde{\chi}_1^0}$ [GeV/ $c^2$ ]	$c\tau$ (mm)	$\sigma_{LO}$ (pb)	Total Events	BR
100	140	500-10,000	0.368	50,000	0.9444
120	169	500-10,000	0.133	50,000	0.9042
140	198	500-10,000	0.0574	50,000	0.8711
160	227	500-10,000	0.0277	50,000	0.8464
180	256	500-10,000	0.0145	50,000	0.8282
220	314	500-10,000	0.0044	50,000	0.8282

Table 6.1: Signal GMSB SPS8 Monte Carlo samples for different  $\Lambda$  with  $50 \text{ cm} < c\tau < 1000 \text{ cm}$  and Branching Ratios (BR).

$\hat{p_T}$	$\sigma_{LO}$ (pb)	Number of Events
50 ~ 80	3322.3	1995062
80 ~ 120	558.3	1992627
120 ~ 170	108.0	2000043
170 ~ 300	30.1	2000069
300 ~ 470	2.1	2000130
470 ~ 800	0.212	1975231

Table 6.2: The  $\gamma+$  jets samples for  $\hat{p_T}$  from 50 GeV/c to 800 GeV/c

## 6.2 ECAL Timing

In this section we describe the measurement of the photon time, tuning of the time from MC and the observation of late photons from satellite proton bunch collisions.

### 6.2.1 Photon Time Measurement for this Analysis

The electromagnetic shower of a photon spreads across several crystals and so the photon's time can be measured using the time from one or all these crystals. For example, the photon's arrival time can come from either the reconstructed time ( $t_{reco}$ ) of the *seed crystal* (crystal with the highest energy deposit),  $t_{seed}$ , or a weighted average time calculated using the reconstructed time and uncertainty of each crystal of the photon's supercluster:

$$t_{Ave} = \frac{\sum_{i=1}^N \frac{t_{reco}^i}{\sigma_i^2}}{\sum_{i=1}^N \frac{1}{\sigma_i^2}}, \quad (6.1)$$

where  $N$  is the total number of crystals of the supercluster,  $t_{reco}^i$  and  $\sigma_i$  are the time and uncertainty on the reconstructed time of each crystal, respectively. Figure 6.1 shows a comparison of the seed time,  $t_{seed}$ , and the average time,  $t_{Ave}$ , as the photon's time. Both distributions are normalized to total number of events.

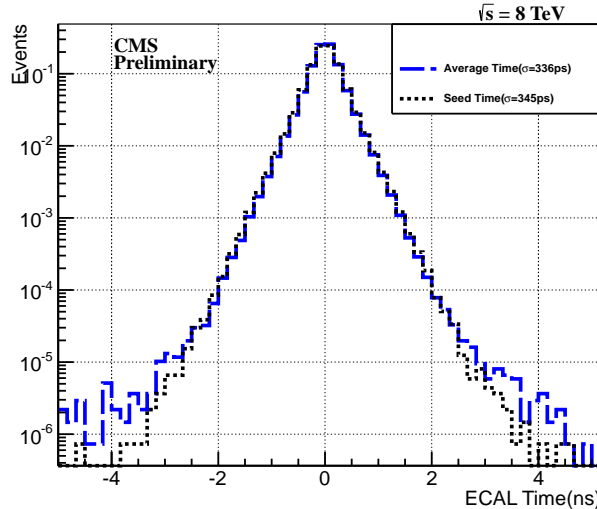


Figure 6.1: Seed (black) and Average (blue) times as the measured photon time.

The width ( $\sigma$ ) of both Gaussian distributions are similar, the standard deviation for the seed time,  $\sigma_{t_{seed}} = 345$  ps, and that for the average time,  $\sigma_{t_{Ave}} = 336$  ps. We expected the standard deviation of the average time to be smaller than the seed time, however due to the presence of crystals with atypically large times as seen in the tails of the average time distribution the average time shows no improvement on the seed time. The average time is susceptible to spurious timing measurements. If one of the crystals in the supercluster happens to be poorly time calibrated or embedded with a spike, the photon time will be biased and this happens often for  $t_{Ave}$  although the magnitude of the bias is smaller.

We use the seed time as the photon's time in this analysis, however, the presence of anomalous signals from spikes, noisy crystals and pile-up events demand a robust method for checking that the photon time has been properly reconstructed since we use the photon's time as our main observable for distinguishing background from signal events. To perform this check we use the  $\chi^2$  of the photon's time computed using the average time and reject those photons with very large  $\chi^2$  which is often the case for

photons with spurious timing measurements. The  $\chi^2$  is computed as

$$\chi^2 = \sum_{i=0}^N \frac{(t_{reco}^i - t_{Ave})^2}{\sigma_i^2} \quad (6.2)$$

where  $N$  is the number of crystals in the photon supercluster,  $t_{reco}$  and  $\sigma_i$  are the time and uncertainty from each crystal, and  $t_{Ave}$  is the average time defined in Equation 6.1. The  $\chi^2$  is used to help distinguish non-isolated spikes from true photons and a distribution of the normalized  $\chi^2$  against the photon time in Figure 6.2 show that spikes which have been misidentified as photons have large  $\chi^2$  and large negative time.

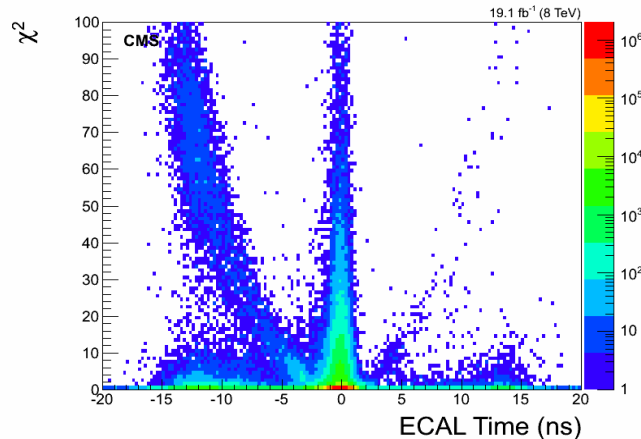


Figure 6.2: A  $\chi^2$  against photon time distribution. Spikes misidentified as photons have very large  $\chi^2$  and negative time particularly the region where  $\chi^2 > 4$  and  $t < -4$  ns.

It is clear from Figure 6.2 that most of the true photons have time around zero but there are also photons with time,  $t \approx 0$ , with large  $\chi^2$ . The contributions from these photons with spurious time measurements especially those with large negative times which we call spikes can be reduced by rejecting photons with  $\chi^2 > 4$ .

### Timing from Monte Carlo

It is challenging to properly simulate the time of MC events so that it captures the conditions of the ECAL sub-detector during data recording. As a result, the mean time and root mean squared (RMS) from MC events does not agree perfectly with those in

data. We correct for this disagreement by shifting the mean time and smearing the RMS with an additional Gaussian convolution on the photon time of MC events so that the MC mean time and RMS matches that of data. The amount (the difference between data and MC photon times) of shifting and smearing required is obtained using selected 1 or 2 jets events and to ensure that true photon events are used, we select events whose final state consist of 1 or 2 jets with in-time photons ( $|t_\gamma| < 2$  ns) of photon  $p_T > 80$  GeV from data and  $\gamma+$ jets MC samples. Shown in Figure 6.3 is the in-time photon time distributions for data and  $\gamma+$ jets MC samples before (left plot) and after (right plot) the corrections are applied on the photon time of  $\gamma+$ jets MC events. We see good agreement between MC and data photon time.

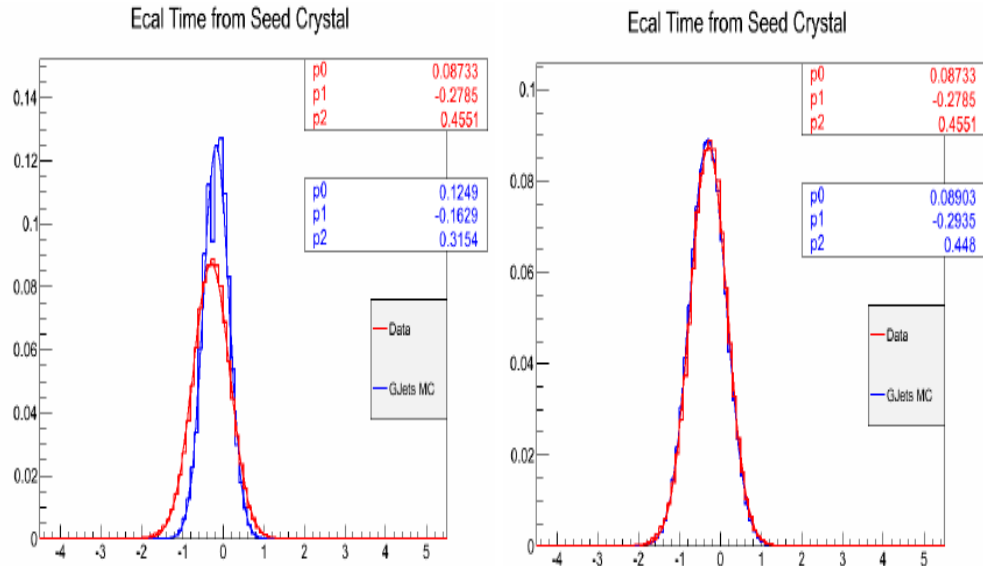


Figure 6.3: Time distributions of in-time photons from  $\gamma+$  jets MC (blue) and data (red) samples before (left) and after (right) we adjusted the MC photon time.

### 6.2.2 Satellite Bunches

Satellite proton bunches which lead or trail the LHC main proton bunch with a time spacing of 2.5 ns are also a source of background with positive times from Beam halo-induced photons observed in ECAL. Figure 6.4 shows the photon time for photons with  $p_T > 50$  GeV/c in ECAL. The 2.5 ns discrete pattern in the photon time confirm the

presence of satellite beam halo-induce photons in the endcap ( $1.47 < \eta < 3.0$ ) (mostly) and barrel ( $|\eta| < 1.47$ ) regions. We find that proton Beam halo-induced photons is a major background to late photons.

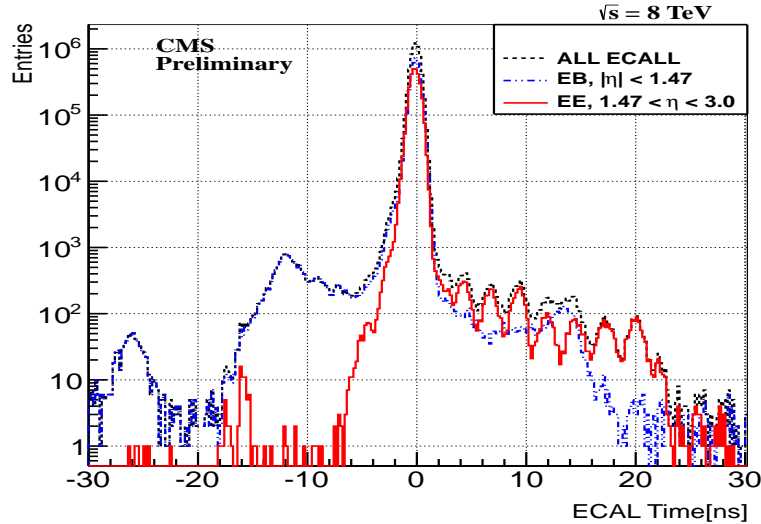


Figure 6.4: Time distribution of photons in barrel (EB), endcap (EE) and all of ECAL (ALL ECAL) with  $p_T > 50$  GeV from data. A 2.5 ns delay timing pattern is observed in ECAL with clarity in EE.

### 6.2.3 $E_T^{\text{miss}}$ Adjustments

In the formation of energy clusters which are used for event reconstruction by the particle flow (PF) algorithm “out-of-time” energy deposits in ECAL are excluded. The reason is because the PF algorithm avoids energy deposits from particles like cosmic muons and machine-induced backgrounds which are not produced from the main  $pp$  bunch collisions, as these are often out-of-time. Because of the exclusion, the out-of-time photon’s transverse energy,  $E_T$ , is not included in the calculation of missing transverse energy or  $\cancel{E}_T$  (from now on we will be using for convenience  $\cancel{E}_T$  instead of  $E_T^{\text{miss}}$  as the symbol for missing transverse energy) of the event. This exclusion introduces differences in the calculation of  $\cancel{E}_T$  for in-time ( $|t_\gamma| < 3.0$  ns) and for out-of-time photon events. Since we are searching for events with late arrival time photons coming from  $pp$  collisions, we correct for the momentum of the late photons by subtracting the out-of-time photon’s

$E_T$  from the particle flow reconstructed  $\cancel{E}_T$  (PF-MET) for events with out-of-time photons and introduce an additional missing transverse energy variable defined as  $\cancel{E}_T^\gamma = \cancel{E}_T - E_T$ , in our final event selection.

### 6.3 Event Selection

Our event selection happens in two stages. The first stage, consisting of L1 trigger at online and an HLT software trigger of multiple selection modules, selects only triggered single photon events. The second stage happens offline, where, our signal-like event selection requirements are applied.

The offline event selection criteria is designed to select signal-like events whose event topology comprise of at least a single photon, multiple jets and large  $\cancel{E}_T$ . The multiple jets arise from the cascade decay of gluino or squark to other quarks or gluons, in addition to the lightest neutralino. We require multiple jets in our event selection as part of the signal event topology, but, also as a way of suppressing non-collision background events like cosmic and beam halo muons, which are usually not associated with jets. Collision background events like multijets and QCD events, where a jet can be misidentified as a photon, are equally suppressed by selecting purely hadronic jets i.e. jets containing a greater portion of hadronic energy fraction from pions and kaons.

The single late photon and large  $\cancel{E}_T$  is from  $\tilde{\chi}_1^0 \rightarrow \gamma + \tilde{G}$  decay and we select only photons in the barrel ( $|\eta_\gamma| < 1.479$ ) with high transverse momentum. This suppresses out-of-time photons from the so-called halo-induced photons produced by ghost/satellite proton bunches. The high- $p_T$  photon requirement also helps suppress out-of-time photons due to timing mismeasurements of photons from QCD and multiple jets events.

The large  $\cancel{E}_T$  requirement is useful for suppressing  $\gamma+$ jets and QCD events with apparent  $\cancel{E}_T$  or *fake*  $\cancel{E}_T$  which arise from energy misreconstruction and cracks in the detector. Out-of-time photon contribution from spikes is also reduced by applying electromagnetic shower shape selection on  $S_{Minor}$  at the HLT trigger level.

#### 6.3.1 Trigger Selection

During the online event selection, only events passing our online higher level trigger (HLT): `HLT_DisplacedPhoton65_CaloIdVL_IsoL_PFMET25`, which is seeded by a L1

trigger: `HLT_L1SingleEG12`, are accepted. The HLT trigger is a combination of selection modules triggering events with at least one calorimeter identification standards of a very loose isolated photon with  $p_T$  of atleast  $65\text{ GeV}/c$  and  $\cancel{E}_T$  (without any out-of-time energy deposit bias) above  $25\text{ GeV}$ . The minor axis of the photon electromagnetic shower must not spread across many crystals in any direction. This is implemented as  $0.1 < S_{Minor} < 0.4$  of the photon.

We study the HLT trigger efficiency and turn-on (efficiency becomes nearly 100%) curve separately for the photon  $p_T$  and event  $\cancel{E}_T$ , using, as the denominator of the event ratio events with at least one jet and a photon also triggered by the HLT trigger: `HLT_Photon50_CaloIdVL_IsoL`. This trigger selects events with photon candidates also satisfying the calorimeter identification standards of a very loose isolated photon with  $p_T$  of at least  $50\text{ GeV}/c$ . The HLT event selection efficiency in  $p_T$  is defined as the fraction of events passing our HLT trigger to events with at least one jet and a photon triggered by the `HLT_Photon50_CaloIdVL_IsoL` trigger within  $\Delta R < 0.5$ , while the efficiency in  $\cancel{E}_T$  is defined as the ratio of events passing our HLT trigger (`HLT_DisplacedPhoton65_CaloIdVL_IsoL_PFMET25`) over events with at least one jet and a photon passing the `HLT_Photon50_CaloIdVL_IsoL` trigger, with no  $\cancel{E}_T$  selection cut applied. Photons selected by both triggers must also satisfy the loose selection cuts, excluding the photon  $p_T$  and  $\cancel{E}_T$  selection cuts, of our offline photon selection requirement summarized in Table 6.3.

The results of the trigger efficiency measurements in photon  $p_T$  and event  $\cancel{E}_T$  shown in Figure 6.5, indicate that the event selection efficiency is 100% for events with photon  $p_T > 80\text{ GeV}/c$  and  $\cancel{E}_T > 60\text{ GeV}$ . The slight difference between the  $\gamma+\text{jets}$  (black) and the GMSB (red) MC samples is because the events in  $\gamma+\text{jets}$  samples have no real  $\cancel{E}_T$ , and it is difficult to simulate apparent or fake ( $\cancel{E}_T$  from detector crack and unclustered energy deposits)  $\cancel{E}_T$  in MC simulation.

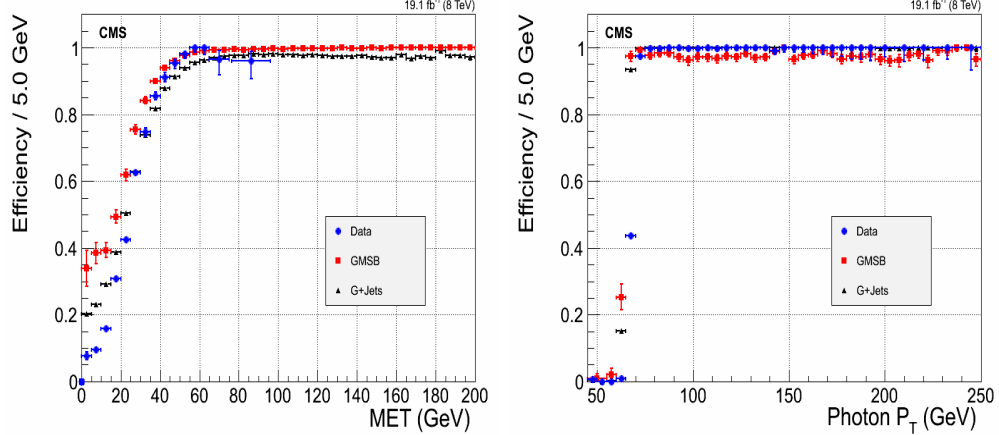


Figure 6.5: Our HLT trigger efficiency turn-on curves in event  $\cancel{E}_T$  (left) and photon  $p_T$  (right). The  $\gamma + \text{jets}$  samples require photon  $p_T > 170$  GeV/c.

### 6.3.2 Offline Selection

Our offline event selection, applied on the HLT triggered single photon events, require that the leading photon have  $p_T > 80$  GeV/c and if the event has more than one photon, the sub-leading photon have  $p_T > 45$  GeV/c. Electromagnetic showers initiated by charged hadrons are rejected by requiring  $E^{\text{HCAL}}/E^\gamma < 0.05$ , where  $E^{\text{HCAL}}$ , is the sum of the energy in the HCAL towers directly behind the ECAL photon supercluster within a  $\Delta R < 0.15$ , with  $\Delta R = \sqrt{(\eta - \eta^\gamma)^2 + (\phi - \phi^\gamma)^2}$ , and  $E^\gamma$  is the photon energy in ECAL.

Electrons are rejected by requiring the absence of hits in the first two layers of the pixel detector that is consistent with an electron track matching the observed location and energy of the photon candidate (this is known as pixel veto requirement).

The photon candidates must satisfy three *isolation* requirements that reject photons produced in hadronic decays: (1)  $Iso_{\text{TRK}} < 0.2$  GeV, where  $Iso_{\text{TRK}}$ , is the sum of the  $p_T$  of tracks compatible with the primary event vertex in an annulus  $0.015 < \Delta R < 0.40$ , excluding a strip half  $\eta$  width of 0.015 and the additional inner cone of size 0.04, optimized to exclude reconstructed tracks from  $Z \rightarrow e^+e^-$  events, centered around the line of vertex pointing to the photon supercluster. The exclusion is to remove the photon's own energy if it converts into an  $e^+e^-$  pair; (2)  $Iso_{\text{ECAL}} < 4.5$  GeV, where  $Iso_{\text{ECAL}}$ , is the transverse energy deposited in ECAL in an annulus  $0.045 < \Delta R < 0.4$ , centered

around the photon ECAL supercluster, excluding the strip half  $\eta$  width of 0.02 and the additional inner cone of size 0.045 centered around the ECAL supercluster position; (3)  $I_{\text{soHCAL}} < 4.0 \text{ GeV}$ , where  $I_{\text{soHCAL}}$  is the transverse energy of HCAL tower in an annulus of  $0.15 < \Delta R < 0.40$ , centered about the ECAL supercluster position. If the photon is very close to a track within a range in  $\Delta R(\gamma, \text{track}) < 0.6$ , it is rejected. This is to avoid misidentifying charge particles as photons and to prevent double counting jets with high electromagnetic energy component as photons. The photon must also be isolated from any other particle in a cone size of  $\Delta R(\gamma, \text{particle}) < 0.4$ . The size of the photon electromagnetic shower along the minor axis ( $S_{\text{Minor}}$ ) must be within 0.12 to suppress photons embedded in hadronic jets.

Only photons belonging to the barrel (EB) region i.e.  $|\eta_\gamma| < 1.479$ , are accepted, to avoid many out-of-time halo-induced photon candidates from ghost/satellite proton bunches, which belong to the endcap (EE) shown in Figure 6.4, and also since not many signal out-of-time photons go into the endcap.

Topological selection cuts,  $1 - E_6/E_2 < 0.98$  and  $1 - E_4/E_1 < 0.98$ , on the photon energy deposit, help suppress spikes which are caused by the direct interaction of the ECAL APDs by charged particles and neutrons producing anomalous photon signal. A summary of our full photon selection criteria is presented in Table 6.3.

For jets, we select jets with  $\eta_{\text{jet}} < 2.4$ , and require that the leading jet in the event has a  $p_T > 35 \text{ GeV}/c$  with the event having at least 1 jet. This helps suppress non-collision background events without jets. The jets are reconstructed using the PF algorithm and identified based on the identification selection criteria summarized in Table 6.4, where a jet candidate must satisfy the following: the Charge Electromagnetic Fraction (CHF) and the Neutral Electromagnetic Fraction (NEF) must make up a greater portion of the jet sub-structure ( $> 99\%$ ), the Neutral Energy Fraction (NEF) must smaller than 99%, in order that the jet is not easily misidentified as a photon. A jet near a photon object within a cone of 0.3 is rejected.

From our HLT trigger event selection efficiency plot in Missing Transverse Energy (MET) shown in Figure 6.5, and in order to suppress most of the background events with out-of-time photons, we observed that a missing transverse energy of at least  $60 \text{ GeV}$  for  $\cancel{E}_T$  and  $\cancel{E}_T^\gamma$  is enough to suppress  $\gamma + \text{jets}$  and QCD events with apparent missing transverse energy.

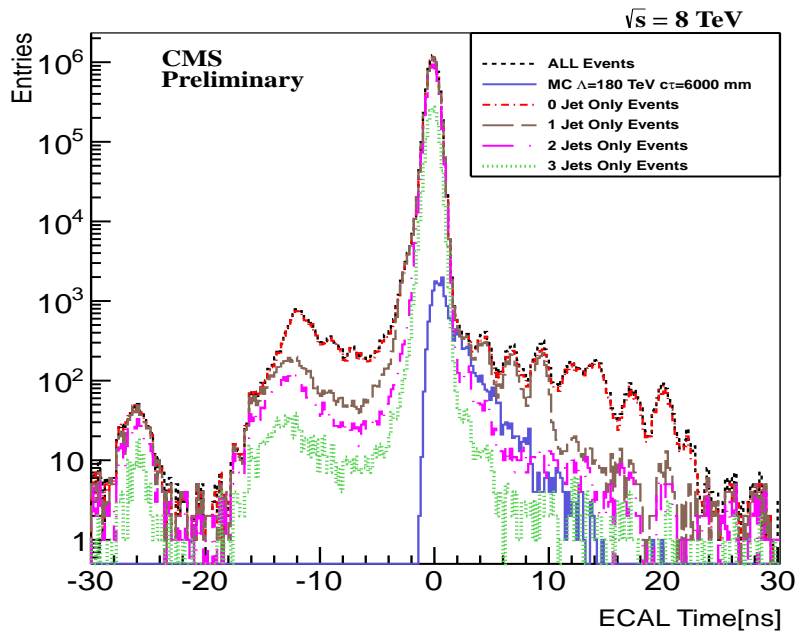


Figure 6.6: Comparing ECAL time distribution of events with different jet multiplicity from small sample of data and a single GMSB  $\Lambda = 180 \text{ TeV}$  and  $c\tau = 6000 \text{ mm}$  sample. Accepted photons must have  $p_T > 60 \text{ GeV}$  and belong to barrel and encaps.

---

**Photon Selection Criteria**


---

<b>Criteria</b>	<b>Requirement</b>
Event leading photon must have $p_T(\gamma^1)$	$> 80 \text{ GeV}$
Other photons in event must have $p_T(\gamma^{2,3,\dots})$	$> 45 \text{ GeV}$
$ \eta_\gamma , (\text{Barrel Only}),$	$< 3.0 (< 1.5)$
$S_{\text{Minor}}$	$0.12 \leq S_{\text{Minor}} \leq 0.38$
$E^{\text{HCAL}}/E^\gamma$	$< 0.05$
$\Delta R(\gamma, \text{track})$	$> 0.6$
$I_{\text{Iso}}^{\text{HCAL}}, I_{\text{Iso}}^{\text{ECAL}}, I_{\text{Iso}}^{\text{TRK}}$	$< 4.0 \text{ GeV}, < 4.5 \text{ GeV}, < 0.2 \text{ GeV}$
Photon Isolation cone size $\Delta R(\gamma, \text{particle})$	$< 0.4$
Topological Spike cuts	$1 - E_6/E_2 < 0.98, 1 - E_4/E_1 < 0.98$

---

Table 6.3: The photon identification and selection criteria used in this analysis

---

**Jet PF identification selection criteria**


---

<b>Criteria</b>	<b>Requirement</b>
Jet $p_T$	$> 35 \text{ GeV}$
Number of Jet constituents	$> 1$
Charge EM energy fraction (CEF)	$> 0.99$
Neutral Hadron energy fraction (NHF)	$< 0.99$
Neutral EM energy fraction (NEF)	$< 0.99$
If $ \eta $ of jet is $> 2.4$ , Charge Hadron energy fraction (CHF)	$> 0$
If $ \eta $ of jet is $> 2.4$ , Charge multiplicity (NCH)	$> 0$
$\Delta R(\gamma, \text{jet}) = \sqrt{(\phi_\gamma - \phi_{\text{jet}})^2 + (\eta_\gamma - \eta_{\text{jet}})^2}$	$> 0.3$
$\cancel{E}_T, \cancel{E}_T^\gamma$	$> 60 \text{ GeV}$

---

Table 6.4: The Jet ID and MET selection used in this analysis

In Figure 6.6, we observed that most of our background events with out-of-time beam halo-induced photons are mostly zero and one jet events. As a result, we use these zero and one jet events as a control sample only to study our background events, while our signal-like events are events with the following topology:  $\geq 1 \gamma + \geq 2 \text{ jets} + \cancel{E}_T > 60 \text{ GeV} + \cancel{E}_T^{\gamma} > 60 \text{ GeV}$ .

## 6.4 Background Estimation

Most of our background events with out-of-time photons are non-collision events produced from different sources. In order to qualify and quantify these different sources, we compare in-time ( $|t_\gamma| < 2 \text{ ns}$ ) photon candidates to out-of-time ( $t_\gamma < -3 \text{ ns}$  and  $t_\gamma > 3 \text{ ns}$ ) photon candidates. By also comparing photons from events with different number of jets, we were able to uncover the different background sources and better quantify the contribution from each source. In Figure 6.7, we present scatter plots of the photon’s ECAL time against  $\eta$  (left) and against  $\phi$  (right) for events with  $\cancel{E}_T > 25 \text{ GeV}$  and photon  $p_T > 60 \text{ GeV}$ , belonging to the barrel and endcap regions.

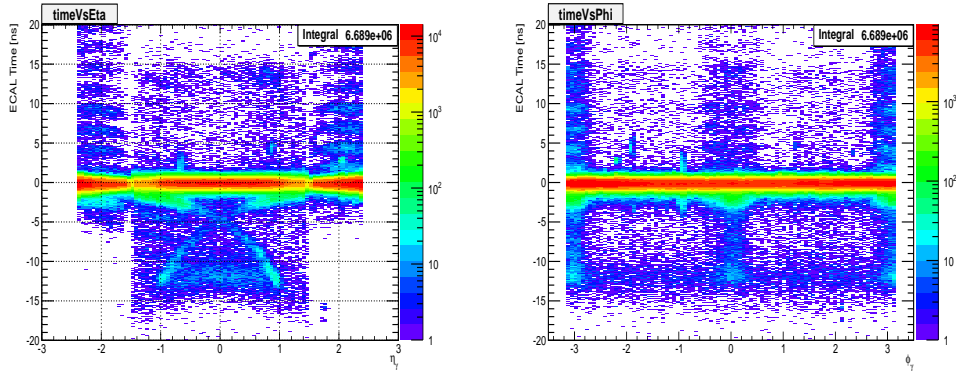


Figure 6.7: ECAL time against  $\eta$  (left) and ECAL time against  $\phi$  (right) for photons with  $p_T > 60 \text{ GeV}$  from data.

These scatter plots show that a good number of photons that are out-of-time belong to very different sources. For example, the “cross-like” feature seen on the left plot, is particular to photons with earlier time and in combination with the time-discrete

pattern, prominent in the endcaps ( $1.479 < \eta_\gamma < 3$ ) regions and the high concentration at  $\phi = 0 \pm \pi$  on the plot on the right, can be interpreted as photons produced by the same so-called proton beam halo. We argue the background out-of-time photon candidates can be split into 4 major categories: (1) Halo-induced photons from main and ghost/satellite beam halo muons, because they have early arrival times, creates the cross-like feature and time-discrete pattern and are also highly concentrated at  $\phi = 0, \pm\pi$ , (2) Cosmic-induced photons produced from cosmic muons, due to the random distribution of out-of-time photons throughout ECAL, (3) Spikes, due to the high concentration of photons with time of about -12.5 ns and Finally, (4) QCD or collision background events with photons with mis-measured ECAL time.

Since spikes are notoriously difficult to identify and eliminate, to reduce their contribution to out-of-time photons, we restrict our event selection to photons with time  $2.0 < t_\gamma < 13.0$  ns and  $-10.0 < t_\gamma < -3$  ns. This reduces our signal search window for events with late photon time to events with photon time between  $2.0 < t_\gamma < 13.0$  ns.

We split the background events into Collision and Non-Collision event categories and study each category separately. We first identify and reject photon candidates from beam halo, cosmic muons and spikes and then estimate the residual non-collision and collision background photon candidates using the **ABCD** background estimation technique.

#### 6.4.1 Collision Background

##### QCD Photons

Events from satellite/ghost proton bunches described in section 3.1.4, produce out-of-time photons which can be present in the barrel. We refer to the events from collisions with out-of-time photons, including QCD events with photons which have mis-measured time, as our *QCD background* events. It is challenging to define a strategy for rejecting this background events. Our approach, after rejecting non-collision events, is to estimate their contribution to signal using the ABCD background estimation method. We also perform a separate background estimation using a control sample of Z events, and show that, these events with out-of-time photons from collisions, are mostly QCD events with photon candidates with time mis-measurements.

### 6.4.2 Non-Collision Background

#### Halo-induced Photons

Protons in the main and sometimes ghost/satellite bunches can, through inelastic scattering with residual gas molecules like H<sub>2</sub> and CO<sub>2</sub> in beam pipe, produce pions which later decay into muons traveling with energy of a few TeV, called *Beam Halo* muons. These energetic muons radiate energetic photons, called *Halo-induced photons*, in the calorimeter through a process called *bremsstrahlung*. Some of the beam halo muons are produced when protons scatter off Tertiary Collimators (TCT), 50 m <  $z$  < 148 m, away from the center of the CMS detector. These halo muons can travel nearly parallel to the main proton bunch but often stir outward from the nominal orbit due to betatron oscillations, in the transverse direction spreading mostly in the horizontal plane, with respect to the CMS detector coordinates. Despite beam cleaning, a sizable population of beam halo muons remains and eventually produce energetic photons in the calorimeters. A scatter plot of the photon ECAL time against  $\phi$  shown earlier in the right plot of Figure 6.7, show that most of these beam halo muons enter the ECAL in the horizontal plane at  $\phi = 0, \pm\pi$ . The rate of halo-induced photons depend on the beam intensity, beam current and the operational conditions of the LHC, like, the machine optics, collimator settings, residual gas densities and LHC proton filling scheme.

The halo muons before entry into ECAL, produce tracks hits which can be reconstructed into muon tracks using segments in the Cathode Strip Chambers (CSC) Endcap muon detectors. The reconstructed tracks hits in the CSC segments can be associated with a halo-induce photon supercluster in ECAL within some narrow opening angle in  $\phi$ .

Due to the beam intensity, most of the halo muons end up in the endcaps, but, some can also end up in the barrel. The resulting halo-induced photons are usually out-of-time compared to photons produced directly from nominal  $pp$  collisions. All of halo-induced photons have early arrival time, since the beam halo muons arrive at the crystals in ECAL before those photons produced at the interaction point in  $pp$  collisions. The halo-induced photon's arrival time can be estimated from the unique flight path of the beam halo muons, with respect to the arrival time of photons from  $pp$  collisions, as

$$t_{\text{ECAL}}^{\text{expected}} = -1/c \left( \pm Z_{\text{cluster}} + \sqrt{Z_{\text{cluster}}^2 + R_{\text{cluster}}^2} \right), \quad (6.3)$$

where,  $Z_{\text{cluster}}$  is the point where the halo muon hits ECAL or the longitudinal distance along  $z$ -axis of the halo-induced photon supercluster position measured from the nominal interaction point,  $R$  is the radial distance of the supercluster from the beam line, which is equal to 1.29 m in the barrel, and  $c$  is the speed of light in vacuum. The estimated halo-induced photon arrival time can be re-arranged to become

$$t_{\text{ECAL}}^{\text{expected}} = -\frac{R}{2c} \exp(-\eta) \quad (6.4)$$

showing the direct dependence on  $\eta$ . In Figure 6.8, the halo-induced photon estimated time is shown as the two red lines, agreeing well with observation from data. This gives us confidence that we understand the source of halo-induced photons and can develop a method of identifying events with halo-induced photons.

By matching halo muon hit positions in CSC segments to photon supercluster positions in the ECAL in  $\phi$ , since halo muons spread mostly in the horizontal plane, we are able to match halo muons to their corresponding halo-induced photons. We use the quantity,  $\Delta\phi(\text{CSC Seg}, \gamma)$ , which is defined as the difference in  $\phi$  between the CSC segment and the photon supercluster position in ECAL, to express this matching. A plot of  $\Delta\phi(\text{CSC Seg}, \gamma)$  for in-time and out-of-time photons is shown in the left plot of Figure 6.8. We find that out-of-time photons often have small  $\Delta\phi(\text{CSC Seg}, \gamma)$ , further confirming that some out-of-time photons are produced by beam halo muons.

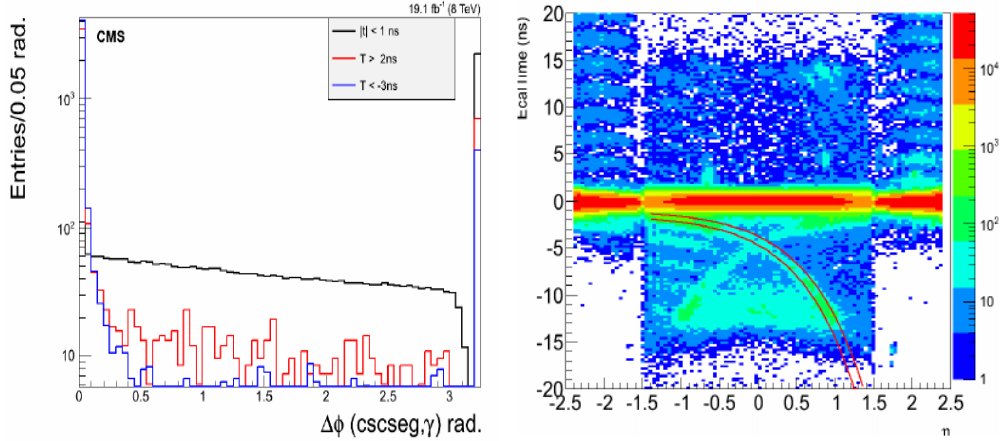


Figure 6.8: ECAL time *vs*  $\Delta\phi(\text{CSC Seg}, \gamma)$  (left) for in time (black) and out-of-time (red and blue) photons. Photon ECAL time *V.s*  $\eta$  (right), expected halo-induced photon time is shown as two red lines.

### Cosmic-induced Photons

Muons produced in cosmic rays with sufficient energy, traveling through the CMS detector, will radiate (bremsstrahlung) photons in ECAL. We refer to these photons as *cosmic-induced photons*. Unlike halo muons, muons from cosmic rays can arrive at ECAL from any direction at any time. We expect the cosmic-induced photons in the barrel to leave track hits, produced by the associated muons from cosmic, in the Drift Tubes (DT) segments found in the muon barrel behind the calorimeters.

Using DT segments and photon supercluster position, in  $\eta - \phi$  directions, in ECAL, we can match cosmic muon track hits in DT segments to ECAL photon superclusters within a narrow window in  $\Delta\eta$  and  $\Delta\phi$ . The DT position, used in the calculation of  $\Delta\eta$  and  $\Delta\phi$ , is a projection of the muon trajectory, using the direction of the DT segment, to the outer surface of ECAL; because of the large space between the muon barrel and the ECAL. A scatter plot for  $\Delta\eta(\text{DT Seg}, \gamma)$  and  $\Delta\phi(\text{DT Seg}, \gamma)$  of the matching, for events with out-of-time photons;  $t_\gamma > 2 \text{ ns}$  and  $t_\gamma < -3 \text{ ns}$ , is shown on the right plot of Figure 6.9. We compare these scatter plots of  $\Delta\eta(\text{DT Seg}, \gamma)$  and  $\Delta\phi(\text{DT Seg}, \gamma)$  to the scatter plots for in-time ( $|t_\gamma| < 1 \text{ ns}$ ), shown on the left plot, of the same Figure 6.9, and find that most out-of-time photons have a small  $\Delta\eta$  and  $\Delta\phi$ .

If we compare these scatter plots of  $\Delta\eta$  and  $\Delta\phi$ , for these out-of-time photons, to

the scatter plots for cosmic-induced photons from a pure cosmic muons sample (data recorded by the CMS detector without proton-proton collisions happening), shown in Figure 6.10, we find a similar small  $\Delta\eta$  and  $\Delta\phi$  occupancy for the true cosmic muons events from the pure cosmic sample. We conclude that, it is possible to use small  $\Delta\eta(\text{DT Seg}, \gamma)$  and  $\Delta\phi(\text{DT Seg}, \gamma)$ , to tag and reject events with cosmic-induced photons.

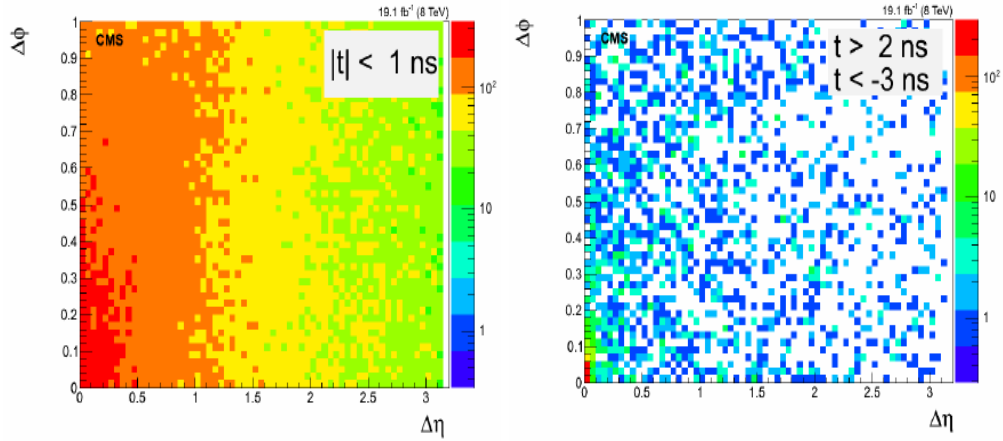


Figure 6.9: Scatter plot showing  $\Delta\eta(\text{DT Seg}, \gamma)$  against  $\Delta\phi(\text{DT Seg}, \gamma)$  for out-of-time ( $t_\gamma > 2 \text{ ns}$  and  $t_\gamma < -3 \text{ ns}$ ) photons (right) compared to in-time ( $|t_\gamma| < 1 \text{ ns}$ ) photons (left). Cosmic photon candidates have small  $\Delta\eta$  and  $\Delta\phi$ .

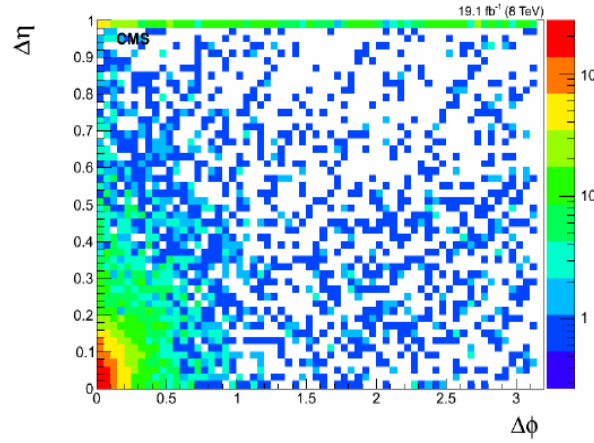


Figure 6.10: Scatter plot of  $\Delta\eta(\text{DT Seg}, \gamma)$  against  $\Delta\phi(\text{DT Seg}, \gamma)$  for photons from pure cosmic muon data. Small  $\Delta\eta$  and  $\Delta\phi$  are cosmic photons.

## Spike-Seeded Photons

Neutrons and charge hadrons can at times deposit their energy directly on the APDs in addition to going through the crystal scintillation process. Such signals, read from the APDs, are *anomalous* and referred to as *spike-seeded photons* or simply *spikes*. Spikes produced from  $pp$  collisions and passing our photon selection requirements, can easily be identified as good photon candidates. A spike supercluster consist of very few crystals; most often one or two crystals. Because spikes occupy few crystals, they can overlapped with good photon candidates, embedded in the photon's supercluster, or buried inside jets. Such embedded spikes cannot be easily identified.

The arrival time of spikes is much earlier (negative), usually about  $t = -12.0$  ns, than for photons produced in nominal  $pp$  collisions and depositing their energy, through crystal scintillation, on the APDs. This is because for spikes, there is the absence of the crystal scintillation process; which takes on average 10 ns. The few crystals holding the spike energy deposits, make it possible for spikes to be identified using a energy topological selection quantity, know as *swiss-cross* and defined as  $1 - \frac{E_4}{E_1}$ . A distribution of swiss-cross for in-time photon events, compare to events from a spike sample (events with photon time  $t = -12$  ns) is shown on the right plot of Figure 6.11. We find that most spikes have about 98% of their energy deposited in a single crystal.

Using the number of crystals in a photon supercluster and comparing the number of crystals belonging to in-time photons, halo-induced photons and spike-seeded photons (photons with  $1 - \frac{E_4}{E_1} > 0.98$ ), shown on the left plot of Figure 6.11, we conclude that most spikes, including spikes embedded in photon candidates, have less than 7 crystals belonging to their supercluster. A combination of the swiss-cross, number of crystals belonging to the supercluster, calculated  $\chi^2$  (defined in Equation 6.2) of ECAL time, and  $S_{\text{Minor}}$  ( $S_{\text{Minor}}$  describes the spread in width, in terms of number of crystals, of the photon electromagnetic shower), is useful for identifying and rejecting events with spike-seeded photons.

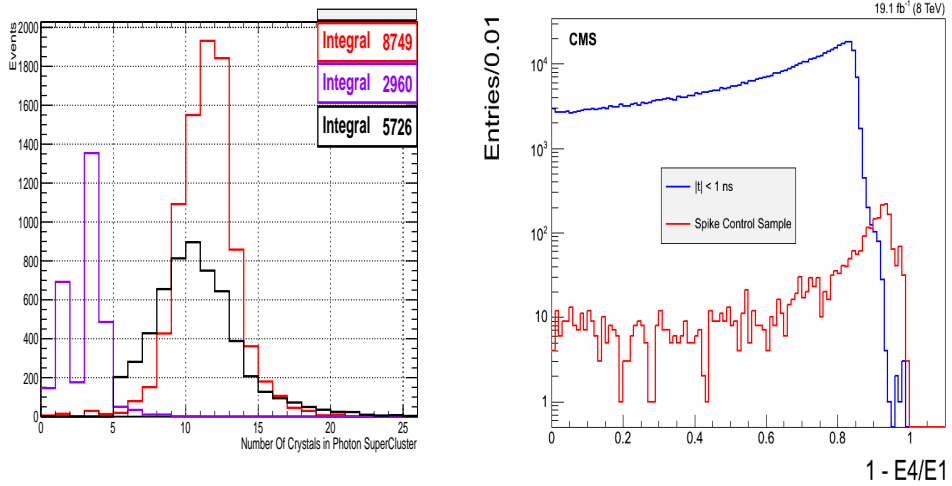


Figure 6.11: *Number of crystals* belonging to a photon supercluster (left) plot for in-time photon candidates (black), spike-seeded photon candidates (magenta) and halo-induced photon candidates (red). The spike-seeded photon candidates are selected using a swiss-cross variable ( $1 - E_4/E_1$ ) (right), shown comparing in-time photons ( $|t_\gamma| < 1.0$ ) to spike candidate sample selected using  $S_{Minor}$ .

### 6.4.3 Event Vetoing

We tag and veto events with halo-induced, cosmic-induced and spike-seeded photons as follows:

- An event with a halo-induced photon is tagged and vetoed, if a CSC segment for  $|\eta| > 1.6$ , is found within 0.05 radian of angle  $\phi$ , with the photon supercluster, i.e. a photon found within  $\Delta\phi(\text{CSC Seg}, \gamma) < 0.05$ , is vetoed.
- An event with cosmic-induced photon is tagged and vetoed, if the photon can be matched to a DT segment within  $\Delta\eta(\text{DT Seg}, \gamma) < 0.1$ , and  $\Delta\phi(\text{DT Seg}, \gamma) < 0.1$ .
- An event with spike-seeded photon is vetoed, if the photon has ECAL time  $\chi^2 > 4$ , number of crystals  $< 7$ ,  $1 - E_4/E_1 > 0.98$ , and  $S_{Minor} < 0.17$ .

The result of the event tagging is shown in Figure 6.12. We observe that most of the non-collision background events are events with halo-induced photons. Very few late arrival time photons are produced from spikes. There is also some significant contribution from cosmic-induced photons. The most interesting observation is the residual out-of-time background (in red) which could not be tagged.

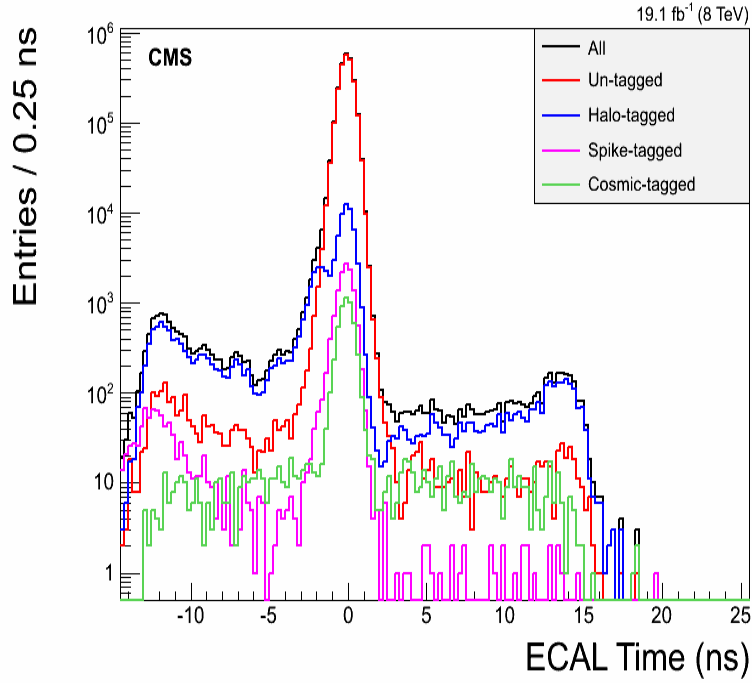


Figure 6.12: Photon ECAL time, for a data sample of 0 and 1-jet events, showing our tagging performance for non-collision background events.

These residual untagged events comprise of some non-collision events, since the tagging and vetoing are not 100% efficient, and mostly collision events with mis-measured time photons. In order to quantify our estimates of these different sources contributing to the untagged background events, we use control samples defined with  $\cancel{E}_T^\gamma$  and  $\cancel{E}_T$ .

We expect signal events, because of the undetected gravitino from the decay of  $\tilde{\chi}_1^0$ , to have large  $\cancel{E}_T^\gamma$  and  $\cancel{E}_T$ ; by large, we mean above 60 GeV. The non-collision (cosmic-induced, halo-induced, spike-seeded photons) and collision (ghost/satellite and QCD) background events can be categorized into high- $p_T$  and low- $p_T$  events. For high- $p_T$  non-collision events, we expect these events to have large  $\cancel{E}_T$ , due to the exclusion of the energy deposits from the out-of-time photons in the missing transverse energy reconstruction, and small  $\cancel{E}_T^\gamma$ , when the large transverse energy contribution from the energy deposits, of the out-of-time photons, is re-introduced, while for low- $p_T$  non-collision events, we expect these events to have both  $\cancel{E}_T^\gamma$  and  $\cancel{E}_T$  small, since the out-of-time photon transverse energy, which was excluded, was in the first place small.

For high- $p_T$  out-of-time collision events, which under normal circumstances should have large missing transverse energy, we expect their  $\cancel{E}_T$  to be large and after re-introducing the energy deposits from out-of-time high- $p_T$  photons, we expect their  $\cancel{E}_T^\gamma$  to be small, while, using the same argument made for low- $p_T$  non-collision events, we expect low- $p_T$  collision events to have both small  $\cancel{E}_T^\gamma$  and  $\cancel{E}_T$ . A summary of our expectations for  $\cancel{E}_T^\gamma$  and  $\cancel{E}_T$  for the different expected background events sources, with possible contribution to the residual untagged events with out-of-time photon, is presented in Table 6.5.

Event Sample	$\cancel{E}_T$	$\cancel{E}_T^\gamma$
Signal Events	Large	Large
High- $p_T$ Non-Collision(Mostly Beam Halo) Events	Large	Small
Low- $p_T$ Non-Collision Events	Small	Small
High- $p_T$ Collision(QCD/Ghost) Events	Large	Small
Low- $p_T$ Collision Events	Small	Small

Table 6.5: Summary of missing transverse expectation for events with out-of-time photons.

Using control samples defined using  $\cancel{E}_T$  and  $\cancel{E}_T^\gamma$  for events with in-time ( $|t_\gamma| < 2.0$  ns) photons, events with out-of-time photons,  $t_\gamma > 3.0$  ns and  $t_\gamma < -3.0$  ns, where each control sample is defined purposely to enhance the contribution of either collision or non-collision background events in the control sample, and simultaneously suppressing contributions from the other, we perform a background estimation in the signal sample ( $t_\gamma > 3.0$  ns,  $\cancel{E}_T^\gamma > 60$  GeV and  $\cancel{E}_T > 60$  GeV), using the so-called ABCD background estimation method and verify that the background estimation method is performing as expected using a data sample of zero and one jet events.

#### 6.4.4 Background Estimation with ABDC Method

Since we expect most of our background events to come from non-collision events, we estimate the number of events we expect from non-collision events in the signal control sample using the ABCD technique. We also estimate the possible contamination, we expect from collision events, to the control samples used in the ABCD method.

##### Non-Collision Background Estimation

To estimate the number of background events from non-collision events, we define regions labeled as ABCD, in photon ECAL time and  $\cancel{E}_T$ , for selected events with  $\cancel{E}_T^\gamma > 60$  GeV. Events with  $\cancel{E}_T^\gamma > 60$  GeV, defines a Control Sample (CS) in which the contribution from collision (QCD) background events is suppressed, since most collision background events have small  $\cancel{E}_T^\gamma$ , as we saw in Table 6.5. The regions: A and B, shown in Table 6.6, contain events with, respectively,  $\cancel{E}_T < 60$  GeV and  $\cancel{E}_T > 60$  GeV, and photon ECAL time,  $-10.0 < t_\gamma < -3.0$  ns, and region C, contain events with  $\cancel{E}_T < 60$  GeV and photon ECAL time,  $3.0 < t_\gamma < 13.0$  ns.

Non-Collision	$\cancel{E}_T < 60$ GeV	$\cancel{E}_T > 60$ GeV
$3.0 < t_\gamma < 13.0$ ns.	C	D
$-10.0 < t_\gamma < -3.0$ ns	A	B

Table 6.6: Definition of ABCD regions used for estimating non-collision background events in the signal region D. Events must satisfy the  $\cancel{E}_T^\gamma > 60$  GeV selection requirement, which reduces collision background events significantly.

The remaining collision background events, which may have some contribution in the B and D regions, are estimated in the next section and also corrected for.

Since the arrival time of photons is independent of the missing transverse energy in the event and since we are selecting events with out-of-time photons (where the definition of  $\cancel{E}_T$ , is the same for all events) in defining the ABCD regions, we expect the ratio in the number of events with high- $\cancel{E}_T$  and low- $\cancel{E}_T$ , for both out-of-time regions, to be the same, provided the contribution from collision events with mis-measured photon time is not large, i.e.  $\frac{N_D}{N_C} = \frac{N_B}{N_A}$ . With this, the number of non-collision background events, with out-of-time photons, expected in the signal region D, is given as

$$N_D^{non-col} = \left( \frac{N_B}{N_A} \right) \cdot N_C, \quad (6.5)$$

where,  $N_B$ ,  $N_A$  and  $N_C$ , are the number of events observed in B, A and C regions, in that order, and  $N_D^{non-col}$ , is the number of non-collision background events we expect in the signal region D.

### Collision Background Estimation

We want to estimate the contribution from collision background events to regions B and D of Table 6.6. Using the ABCD technique again, we define regions in photon ECAL time and  $\cancel{E}_T^{\gamma}$ , for selected events with  $\cancel{E}_T > 60$  GeV. The events with  $\cancel{E}_T > 60$  GeV define a control sample, where the contribution from collision events is dominant, as seen in Table 6.5. Since most collision events have in-time ( $|t_\gamma| < 2$  ns) photons, the few collision events with out-of-time photons contributing to the B and D regions, because the photon time is mis-measured, can be estimated using regions with in-time photons. The definition of each region used in the ABCD method, to estimate the out-of-time photon collision background, is given in Table 6.7.

Collision	$\not{E}_T < 60 \text{ GeV}$	$\not{E}_T > 60 \text{ GeV}$
$3.0 < t_\gamma < 13.0 \text{ ns.}$	C	D
$-2.0 < t_\gamma < 2.0 \text{ ns}$	E	F
$-10.0 < t_\gamma < -3.0 \text{ ns}$	A	B

Table 6.7: A,B,C,D,E,F regions used for estimating collision background events with out-of-time photons contamination the regions B and D of Table 6.6. Here, events must satisfy  $\not{E}_T > 60 \text{ GeV}$ , selection requirement.

Using a similar argument that the photon arrival time is independent of the missing transverse energy, the number of collision events contributing to the region B,  $N_B^{col}$ , is estimated as

$$N_B^{col} = N_B = \left( \frac{F}{E} \right) \cdot N_A, \quad (6.6)$$

and the number of events contributing to the signal region D,  $N_D^{col}$ , is estimated as

$$N_D^{col} = N_D = \left( \frac{F}{E} \right) \cdot N_C, \quad (6.7)$$

where,  $N_i$ , is the number of events in each region,  $i = A, B, C, D, E, F$ .

### Combined Background Estimation

Now that we have estimates for both collision and non-collision event contributions, we can estimate the total number of background events expected in the signal region D (Events with  $\not{E}_T > 60 \text{ GeV}$ ,  $\not{E}_T > 60 \text{ GeV}$  and  $3.0 < t_\gamma < 13.0 \text{ ns}$ ), as

$$N_D^{Total} = \left( \frac{N_B - N_B^{col}}{N_A} \right) \cdot N_C + N_D^{col} = N_D^{non-col} + N_D^{col} \quad (6.8)$$

where,  $N_D^{Total} = N_D^{non-col} + N_D^{col}$ , is the total background events estimated in our signal region D from non-collision and collision background events.

### Background Estimation Method Validation

We verify that our background estimation method performs as expected using a data sample of 0 and 1-jet events. We do not expect signal events in this sample. A statistical agreement between the expected number of background events, obtained using our background estimation method, and the number of events observed in our signal region D, affirms that the method is reliable. The accepted 0 and 1-jet events used must pass the same event selection requirements as potential signal events described in Tables 6.3 and 6.4, in addition to vetoing non-collision background events. The event yields in each control sample including tagged events with halo-induced, cosmic-induced and spike-seeded photons is shown in Table 6.8.

Control Sample	Yield	Beam Halo	Cosmic	Spike
A	851	5075	237	65
B	38	300	17	1
C	359	1508	368	9
D	10	22	30	0
<hr/>				
A	8	1	1	0
C	2	0	0	0
F	35271	-	-	-
E	1445254	-	-	-
B	-	-	-	-
D	-	-	-	-

Table 6.8: Event yields used in validating the ABCD background estimation method using 0 and 1-jet events sample. Halo/cosmic/spikes yields are obtained from tagged events. All events must pass photon, jet and  $E_T^{\text{miss}}$  selection requirements.

Using the event yields in Table 6.8 for each region, and Equations 6.6, 6.7 and 6.8,

we obtain the following estimates for the expected number of events in signal region D:

$$\begin{aligned} N_B^{col} &= \frac{35271}{1445254} \times 8 = 0.64^{+0.35}_{-0.34}, \\ N_D^{col} &= \frac{35271}{1445254} \times 2 = 0.46^{+0.11}_{-0.09}, \\ N_D^{Total} &= \left( \frac{38 - 0.64}{851} \times 359 \right) + 0.46 = 16.41^{+3.00}_{-2.59}. \end{aligned}$$

The uncertainty are statistical uncertainties based on the event statistics in each region. Our expected number of background events in signal region D is  $16.41^{+3.00}_{-2.59}$ , which is, within the statistical uncertainties, agreeable with the 10 events we observe, satisfying all our event selection requirements, in the signal region D. This give us confidence in our background estimation method and the impetus to use the method in our background estimation of signal events.

#### 6.4.5 Background Estimation Cross Check

Another method for estimating our background events with out-of-time electromagnetic particles from collision, is using  $Z \rightarrow e^+e^-$  events, since we expect the electron candidates from Z decay to be in-time because of the prompt nature of the decay of Z bosons. We use events with electron candidates from a **SingleElectron** (single electron triggered events) and **DoubleElectron** (double electron triggered events) data samples, where we expect contributions from non-collision events to be very small. These events are selected such that out-of-time energy deposits in ECAL, from electron candidates, are accepted. The background events to the Z-boson events are events with candidate electrons from collision with mis-measured electron time. An out-of-time electron can be randomly matched with another candidate electron to give a di-electron mass which is of the order of the mass of Z. These background events also include events with poorly reconstructed out-of-time energy deposits in ECAL.

To reduce any out-of-time event from beam halo and cosmic events, occurring simultaneously with true  $pp$  collision events, we accept only events satisfying the following event selection requirements: the two electron candidates for the Z boson must each have a  $p_T > 30 \text{ GeV}/c$ , the di-electron mass,  $|m_{e^+e^-} - 91| > 61 \text{ GeV}/c^2$ , both electrons must be in the barrel, i.e.  $|\eta_{e^-}| < 1.479$  and  $|\eta_{e^+}| < 1.479$  and the electron ECAL arrival time

$\chi^2 < 4$ . The electron's arrival time is taken to be the seed crystal time, and corrected to account for the electron's time of flight, which is different from photons. The chosen seed crystal must satisfy the recommended crystal (reconstructed hit) cleaning criteria; which requires that the seed crystal is not a spike, is not noisy and has been properly time calibrated.

From the accepted events with Z candidates, we define a signal event sample for which the di-electron mass is between  $76 \text{ GeV}/c^2 < |m_{e^+e^-}| < 100 \text{ GeV}/c^2$ , i.e.  $76 \text{ GeV}/c^2 < m_{e^+e^-} < 100 \text{ GeV}/c^2$ , and a background or sideband event sample where the di-electron mass is either between  $50 \text{ GeV}/c^2 < m_{e^+e^-} < 76 \text{ GeV}/c^2$  or  $100 \text{ GeV}/c^2 < m_{e^+e^-} < 130 \text{ GeV}/c^2$ . The di-electron mass (left plot) and electron arrival time (right plot) of both electron candidates of the Z boson (signal (blue)) together with the total Z boson candidates is shown in Figure 6.13.

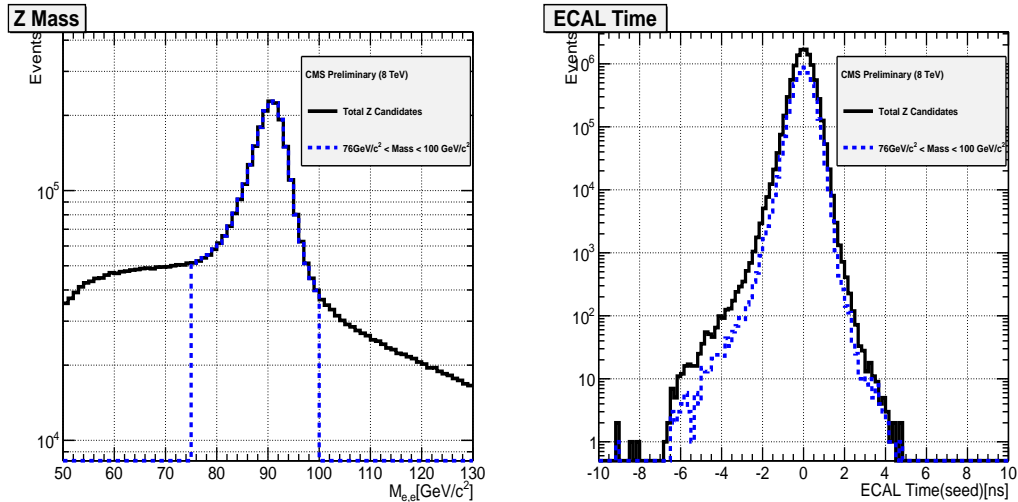


Figure 6.13: Di-electron mass distribution (left) and the time (right) of the two electron candidates for the signal,  $76 < m_{e^+e^-} < 100 \text{ GeV}/c^2$ , of Z boson sample. Events are from the Single/DoubleElectron data sample.

A scatter plot of the arrival ECAL time against  $\eta$  (top right plot) and  $\phi$  (bottom right plots) of both electrons of the Z is shown in Figure 6.14. A clear difference in the scatter plots is seen comparing events from the Single/DoubleElectron data sample (plots on the right), which do not have the familiar beam halo features (the “cross-shape” and

high event concentration at  $\phi = 0, \pm\pi$ ), to events from **SinglePhoton** data sample (plots on the left). We conclude that, the candidate Z event sample is free from contamination from non-collision events and is useful for estimating out-of-time background events from collisions.

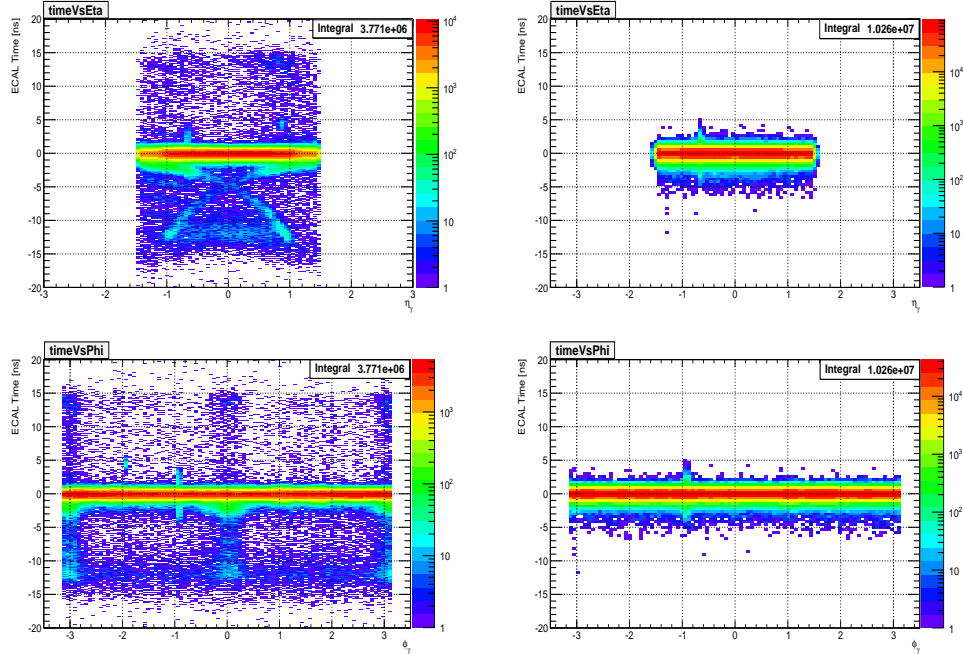


Figure 6.14: ECAL time  $Vs \eta$  (top plots) and  $Vs \phi$  (bottom plots) for electromagnetic particle candidates from **SinglePhoton** data sample (left) compared to electromagnetic particle candidates from the **Single/DoubleElectron** data sample (right). All electromagnetic particle candidates are in barrel. Most of the electromagnetic particles with “cross-shape” and at  $\phi = 0, \pm\pi$ , are halo-induced photons.

In order to estimate the out-of-time background events from collision, we estimate the probability for an in-time ( $|t| < 2$  ns) event to become out-of-time ( $t < -3$  ns or  $t > 3$  ns) because of the mis-measurement of the time of the electron candidates.

We estimate this probability by dividing the Z candidate events according to their arrival time as follows:

- In-time Z boson events: Both electrons of the Z boson candidate have arrival time,  $|t| < 2$  ns. Their di-electron mass is shown on the top right plot of Figure 6.15,

- Early time Z boson events: Both electrons of the Z boson candidate have arrival time,  $t < -3$  ns. Di-electron mass shown in the bottom left plot of Figure 6.15,
- Late time Z boson events: At least one of the electrons of the Z boson candidate have arrival time,  $t > 3$  ns. The di-electron mass is shown in the bottom right plot of Figure 6.15.

The true Z boson events in each of the three Z boson event samples, defined above, is estimated as follows: we first fit, with a polynomial function, a sideband ( $50 < m_{e^+e^-} < 76 \text{ GeV}/c^2$  and  $100 < m_{e^+e^-} < 130 \text{ GeV}/c^2$ ) of the di-electron mass distribution (see top left plot of Figure 6.15). Using the side band fit function, we subtract the integral of the fit function from the total number of Z boson candidates in the Z boson mass peak ( $76 < m_{e^+e^-} < 100 \text{ GeV}/c^2$ ) in each of the three samples. The result of the subtraction gives an estimate of the true Z boson events in the in-time and out-of-time Z boson event samples.

Table 6.9 show the resulting number of Z boson events.

Event Sample	Early Time ( $t < -3$ ns)	In-time ( $ t  < 2$ ns)	Late Time ( $t > 3$ ns)
Total	378	2349187.0	41.0
Estimated Z boson Background	329	996803.6	8.6
Estimated signal Z bosons	49	1352383.4	32.4

Table 6.9: Number of Z boson events with di-electron invariant mass,  $76 < m_{e^+e^-} < 100 \text{ GeV}/c^2$  in the in-time and out-of-time Z boson samples.

The 32.4 events for the late time Z boson events consist of 3 Z events with both electrons with time,  $t > 3$  ns. These 3 Z events could be attributed as produced from ghost/satellite bunch collisions since the ratio of these 3 events to in-time Z events (1.35 million) from main proton bunch collisions is of the order  $10^{-6}$ , which is consistent expected luminosity at collision for ghost/satellite bunches. The intensity of ghost/satellite proton bunch is about  $10^3$  less than that for the main proton bunch [32, 33].

The probability for in-time events becoming out-of-time for proton bunch collision is  $P_1$ , and can be estimated as  $29.4/1352383.4 = 1.09^{+0.28}_{-0.23} \times 10^{-5}$ , while the probability

for in-time events becoming out-of-time for ghost/satellite bunch collisions is  $P_2$ , and can be estimated as  $3/1352383.4 = 2.22_{-0.96}^{+1.7} \times 10^{-6}$ .

Using these probabilities we can predict the number of collision background events in out analysis, which have late time ( $t > 3.0$ ), as

$$N = n_1 \times P_1 + n_2 \times (2P_1(1 - P_1) + P_1^2) + n_1 \times P_2 + n_2 \times P_2 \quad (6.9)$$

where  $n_1$  is the number of in-time one photon events (28208) and  $n_2$  is the number of two photon in-time events (38) taken from the F region of the final results of our background estimation, shown in Table 6.10.

The estimated the number of background events from collisions in the signal region D,  $N_D^{col} = 0.370_{-0.072}^{+0.092}$ , events. Comparing this to the estimated background from collision, using the ABCD method, which is  $28283/1446522 = 0.093_{-0.047}^{+0.093}$ , events, we find that the two methods of estimating the number of background events from collision are not exactly equal. However, both method agree that the background contribution from collision events with out-of-time electromagnetic particles is almost negligible (less than a single event) such that the uncertainties on the ratio of out-of-time to in-time events used in our ABCD collision background estimation does not affect the final results.

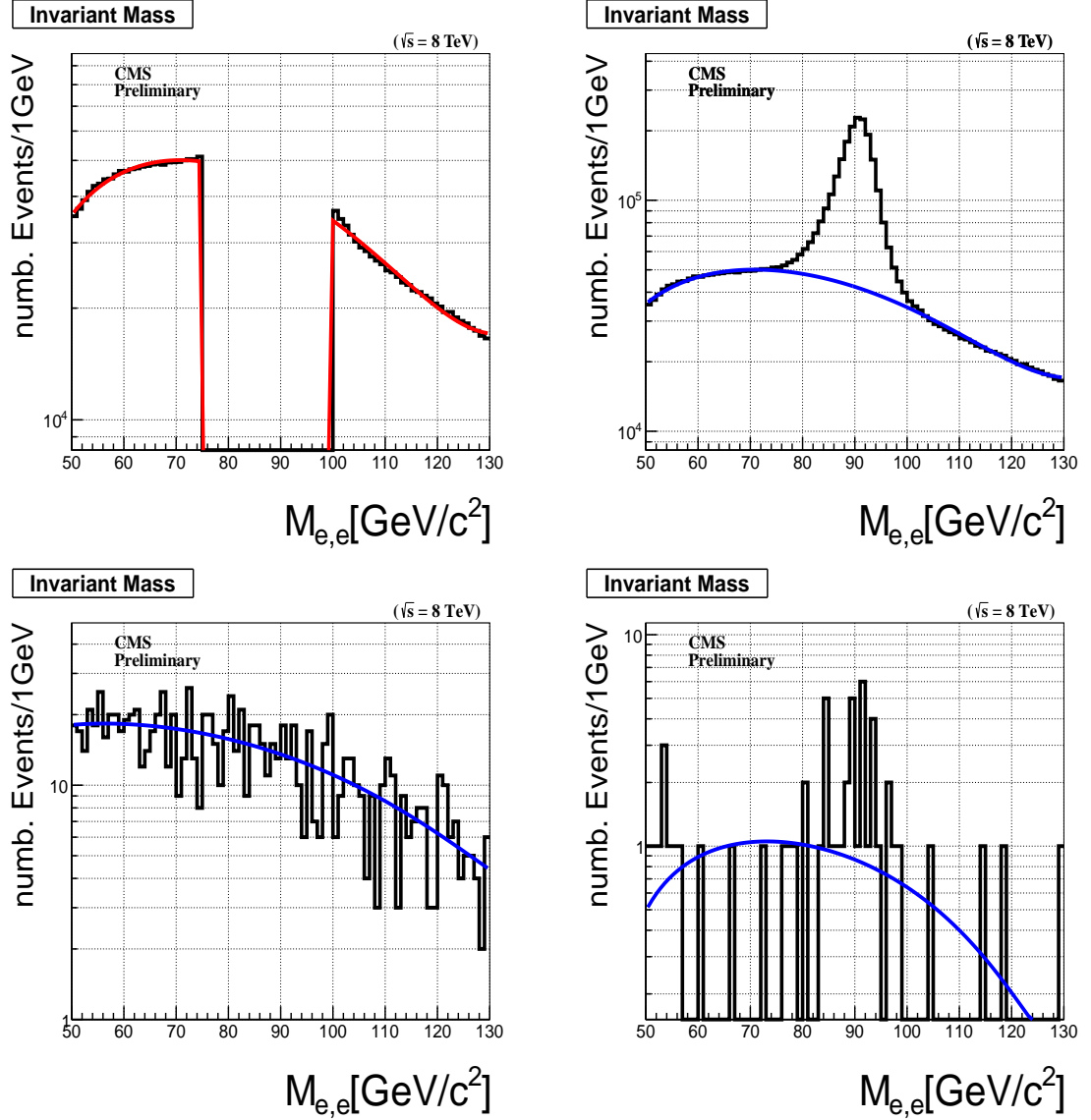


Figure 6.15: Di-electron invariant mass and polynomial fit (red) for sideband sample ( $50 < m_{e+e-} < 76 \text{ GeV}/c^2$  and  $100 < m_{e+e-} < 130 \text{ GeV}/c^2$ ). Di-electron invariant mass and polynomial fit (blue) for in-time ( $|t| < 2 \text{ ns}$ )  $Z$  candidates (*top right*). Di-electron invariant mass and polynomial fit for out-of-time ( $t < -3 \text{ ns}$ )  $Z$  candidates (*bottom left*). Di-electron invariant mass and polynomial fit for out-of-time ( $t > 3 \text{ ns}$ )  $Z$  candidates (*bottom right*). The fits are used to estimate the number of true  $Z$  bosons in the in-time and out-of-time  $Z$  candidate samples.

## 6.5 Results

After running our analysis on the SinglePhoton data samples requiring events with at least 2 jets, at least one photon with ECAL time  $3.0 < t_\gamma < 13.0$  ns,  $\cancel{E}_T^\gamma > 60$  GeV, and  $\cancel{E}_T > 60$  GeV, we observed a single event passing all our event selection requirements as a signal candidate. This event has one photon and two jets. The photon has a transverse momentum of  $224$  GeV/c and an ECAL time of  $12.17$  ns.

Our expected number of background events estimated is  $0.093^{+0.301}_{-0.047}$ . This number was computed as

$$\begin{aligned} N_B^{col} &= \frac{28246}{604958} \times 3 = 0.140^{+0.108}_{-0.061} \\ N_D^{col} &= \frac{28246}{604958} \times 2 = 0.093^{+0.093}_{-0.047} \\ N_D^{Total} &= \left( \frac{1 - 0.14}{3} \times 0 \right) + 0.093 = 0.093^{+0.301}_{-0.047} \end{aligned}$$

using the event yields presented in Table 6.10.

In our final result, we use the collision background estimated using the  $Z \rightarrow e^+e^-$  method which gave us the following:

$$\begin{aligned} N_B^{col} &= 0.51^{+0.28}_{-0.27} \\ N_D^{col} &= 0.37^{+0.09}_{-0.07} \\ N_D^{Total} &= \left( \frac{1 - 0.51}{3} \times 0 \right) + 0.37 = 0.37^{+0.39}_{-0.07}. \end{aligned}$$

From the result of our counting experiment and assuming a Poisson distribution for the observed number of events we obtain a upper limit of 4.37 on the number of signal events at 95% Confidence Level (CL) using the one event observed in the signal region and the estimated 0.37 background events.

Control Sample	Yield
<b>Total Events</b>	
D	1
C	0
B	1
A	3
<b>Collision Background Events</b>	
A	2
C	4
F	28246
E	604958

Table 6.10: Event yields used in our final background estimation for signal candidate events whose final state consist of at least one photon, at least two jets,  $\cancel{E}_T^{\gamma} > 60 \text{ GeV}$  and  $\cancel{E}_T > 60 \text{ GeV}$ .

## Chapter 7

# Limit Setting and Interpretation

### 7.1 Exclusion Limit Setting

Since we did not find any excess of events over the expected SM background prediction we compute *exclusion limits* based on our findings. In a search and discovery experiment, the exclusion limit is either an “upper” or a “lower” limit which is set on some *Parameter Of Interest* (POI) of a model, like the signal-strength modifier,  $\mu$ , which is directly related to the production cross-section of a new particle predicted to exist by the model. An exclusion limit on  $\mu$  can be easily translated into exclusion limits on the mass and lifetime of the new particle allowing us to make following quantitative statements:

- a Long-Lived Neutral Particle, if it exists, is produced with a cross-section below a certain threshold with this probability and the certain threshold is an **upper** limit on the Long-Lived Neutral Particle’s production cross-section.
- a Long-Lived Neutral Particle decay, if it happens, takes place with a mean lifetime larger than a certain threshold with this probability and the threshold is a **lower** limit on the Long-Lived Neutral Particle’s mean lifetime.

Other equally important parameters like the uncertainties of the experiment, detector inefficiencies and luminosity measurements which can impact the exclusions limits but are not the parameters under investigation by the analysis are called *nuisance parameters*, usually denoted as  $\theta$ . Nuisance parameters are used to introduce uncertainties in the computation of the exclusion limits.

### 7.1.1 $CL_S$ Method to Determine Exclusion Limits

The  $CL_S$  method is a statistical procedure used in a search and discovery experiment for evaluating exclusion limits and making constraints on the possible range of values of the fundamental parameters of a model which attempts to describe the observation or data from the experiment [56]. The goal of the method is to constraint the value of the POI,  $\mu$ , and this is obtained from the ratio of the probabilities or  $p$ -values of the confidence interval derived from the signal plus background model or hypothesis to the background-only hypothesis. This ratio which is the  $CL_S$  is defined as:

$$CL_S \equiv \frac{CL_{s+b}}{CL_b} \equiv \frac{p_{s+b}}{1 - p_b} \quad (7.1)$$

where  $CL_b$  and  $CL_{s+b}$  are the probabilities of the confidence intervals derived from the background-only and signal plus background ( $s + b$ ) hypothesis, respectively, and  $p_{s+b}$  and  $p_b$  are the  $p$ -values of  $s + b$  and  $b$ -only hypothesis, respectively. The  $CL_S$  is computed for different values of  $\mu$  with each value signifying the level of signal contribution required to describe the observation. A set of values of  $\mu$  in an experimentally defined region in the phase-space is excluded if the corresponding evaluated value of the  $CL_S$  is below 0.05 and this automatically corresponds to 95% Confidence Level (CL) in the excluded region of the parameter.

The  $CL_S$  is the most favorable method compared to the  $CL_{s+b}$  for evaluating the exclusion limits. This is because in some cases using the  $CL_{s+b}$  produces limits where the background-only hypothesis is also excluded or the limit on the signal is negative (large background and small observed number of events) and such limits are difficult to interpret. Thus with the  $CL_S$  we are always guaranteed to produce non-negative limits. In other words, by *normalizing* the  $CL_{s+b}$  (dividing the  $CL_{s+b}$  with the  $CL_b$ ) we avoid producing erroneous limits like in the scenario where when the background rate,  $b$ , is small the evaluated interval using  $CL_S$  still covers the true value unlike using the  $CL_{s+b}$  procedure where when  $b$  is small the procedure is more likely to produce an error i.e. evaluates an interval which does not cover the true value [57].

Theoretical, systematic and statistical uncertainties are taken into account in the  $CL_S$  method through the use of nuisance parameters.

### 7.1.2 Uncertainty Studies

We have required in our event selection that the photon  $p_T$  be greater than  $80\text{ GeV}/c$ , the jet  $p_T$  be greater than  $35\text{ GeV}/c$  and the missing transverse energy be greater than  $60\text{ GeV}$ . The same selection requirements applied to our MC signal event sample should guarantee a good event selection efficiency estimate. Any difference in the photon  $p_T$ , jet  $p_T$  and missing transverse energy between MC and data will be a source of systematic uncertainty on the efficiency of selecting signal events. These uncertainties can come from quantities like jet energy scale (JES), jet energy resolution (JER), electron-photon energy scale, instrumentation related and energy deposits not clustered during missing transverse energy reconstruction, photon arrival time bias and ECAL time resolution. Table 7.1 presents some of the sources of uncertainties considered in this analysis. The uncertainty values displayed are computed by varying by  $1\sigma$  deviation of the nominal value of the given quantity, like JES, while keeping the values of the other uncertainty sources fixed and counting the number of events passing our event selection requirements. ECAL timing bias which has to do with the absolute reference time ( $0\text{ ns}$ ) of the ECAL time is the source of our largest uncertainty and since the photon arrival time is measured with respect to this reference time the ECAL time uncertainty has the largest impact on our analysis as our analysis is based on counting the number of events with photon ECAL time above  $3\text{ ns}$ . The next largest uncertainties are from energy deposits missed by the clustering algorithm. This affects the photon energy scale, missing transverse energy scale, jet energy scale and resolution. The uncertainty on the photon energy scale in the barrel was estimated to be  $4.0\%$  which is based on measuring the photon energy of events with  $Z \rightarrow \mu\mu\gamma$  decay where the muon radiates a photon in a process known as the final-state radiation (FSR) [58].

The uncertainty on the  $E_T^{\text{miss}}$  resolution uses a conservative estimate from  $E_T^{\text{miss}}$  measurements in QCD events [59, 60] where the  $E_T^{\text{miss}}$  uncertainty is calculated using the fraction of events passing an event selection based on  $E_T^{\text{miss}}$  for different  $E_T^{\text{miss}}$  thresholds.

The uncertainty on the ECAL time resolution was obtained by comparing the mean time of photons of events from  $\gamma+\text{jet}$  MC sample to events from data with photon ECAL time,  $|t_\gamma| < 2\text{ ns}$ . The difference is found to be of the order of  $200\text{ ps}$  per event.

Meanwhile, the systematic uncertainty on luminosity measurement has the recommended value of 2.2% provided by CMS and LHC luminosity measurements while the uncertainty from the measurement of the Parton Density Functions (PDF) is evaluated using the re-weighting technique which uses the Master Equation of CTEQ65 model set described in [61].

The systematic uncertainties do not impact our results in a significant way since we use a data-driven method for estimating our background.

The statistical uncertainty in the ABCD background estimation method is our largest source of uncertainty in this analysis and we estimate it to vary upward by 223% and downward by 51%. This large background statistical uncertainty is because of the very low event yields. Our final result is affected by the signal selection efficiency only despite the large background estimation uncertainty. These signal selection uncertainties are used as nuisance parameters in the calculation of the upper limit on the observed signal cross-section ( $\sigma_{UL}$ ).

Source	Uncertainty(%)
ECAL absolute time (0.0 ns)	< 10.0%
ECAL time resolution (0.5 ns)	< 5.0%
Unclustered energy deposits	< 9.0%
Photon energy scale	< 4.0%
Jet energy scale (JES)	< 9.0%
Jet energy resolution (JER)	< 9.0%
$E_T^{\text{miss}}$ resolution	< 2.8%
PDF uncertainty	< 1.70%
Background estimation uncertainty	51.0% to 223%
Luminosity (4.5%)	< 2.2%

Table 7.1: Summary of systematic uncertainties for signal efficiency and background estimation in this analysis and applied to our final results.

### 7.1.3 The HiggsCombine Tool for Evaluating Upper Limits

CMS has developed a statistical software package which implements the  $CL_S$  method for hypothesis testing and evaluating confidence limits called HIGGS COMBINE [62]. The HIGGS COMBINE tool provides access to a variety of robust statistical methods with optimized performance for computing limits and takes as input the expected number of events or a histogram of the signal, the estimated background, the observed number of events from data and the uncertainties and produces an upper limit in the signal-strength modifier,  $\mu$ , which is translated to the production cross-section of a given physics process. In addition to the numerous computing and optimization advantages, the HIGGS COMBINE tool allows for the possibility of using several different statistical inference methods like Frequentist, Bayesian, Analytical and Hybrid methods to compute the upper limits. Through this way we are able to make comparisons and perform simple checks for any inconsistency. In this analysis we used the prescribed HybridNew (a hybrid of Frequentist and Bayesian methods) method to evaluate the observed limits. We describe in detail in the next subsections how the statistical hypothesis testing is formulated and upper limits are derived.

#### Statistical Test Formalism

The objective of a statistical test is to set upper limits on the cross-sections derived from a signal plus background hypothesis which in our case is the SPS8 benchmark GMSB model. The region of the phase-space of the cross-section defined by the POI,  $\mu$ , of the SPS8 benchmark GMSB model which fails the goodness-of-fit test to the observed data which is the result of our search experiment is excluded. The statistical formalism to perform such a test goes in the following way.

Since our search experiment is an event counting experiment, we construct a histogram in the photon ECAL time of the number of events,  $\mathbf{M}$ , passing our final event selection and acceptance. Suppose the number of events in each bin of the histogram is  $n_i$  with  $i = 1, \dots, N$ , where  $N$  is the number of bins of the histogram. Since we only observed a single event filling just one bin this means  $N = 1$ . The expected number of events in the  $i^{th}$  bin given as:  $E[n_i] = \mu s_i + b_i$ , is the sum of events from all known physics processes which is a combination of events due to the Standard Model which we call background

events,  $b_i$ , and events due to the SPS8 benchmark GMSB model which we call signal events,  $s_i$ . The signal-strength modifier,  $\mu$ , being the POI relates the expected cross-section ( $\sigma_{th}$ ) as predicted by the SPS8 benchmark GMSB model to the actual observed cross-section ( $\sigma^{Obs}$ ) as

$$\mu = \frac{\sigma^{Obs}}{\sigma_{th}}. \quad (7.2)$$

When  $\mu = 0$  it means the SPS8 benchmark GMSB model contributes nothing to the number of events in each bin and gives an opportunity to test the Standard Model background-only hypothesis.

When  $\mu = 1$  it means the SPS8 benchmark GMSB theory contributed to the number of events in each bin and gives an opportunity to tests the signal plus background hypothesis.

The other values for  $\mu$  corresponds to different rates of contribution by the SPS8 benchmark GMSB model.

In order to measure the compatibility of a given hypothesis to the observed data we define a joint probability density function called the *likelihood*. The cross-section of an interesting event like a new particle is very low compared to the total cross-section of any scattering event happening, as a result, the likelihood function,  $\mathcal{L}$ , is the product of the Poisson probabilities for all the bins of the histogram:

$$\mathcal{L}(\mu, \theta) = \prod_{i=1}^N \frac{(\mu s_i + b_i)^{n_i}}{n_i!} e^{-(\mu s_i + b_i)} \cdot \mathcal{G}(\theta), \quad (7.3)$$

where  $\mathcal{G}(\theta)$  is a product of probability distributions of the *nuisance parameters* through which the uncertainties which impact the limit on  $\mu$  are introduced. This probability distributions can be different for different uncertainties ranging from Poisson, log-normal, Gaussian and Gamma distributions. In our evaluation of the exclusion limits in this analysis we introduced all the uncertainties presented in Table 7.1 as nuisance parameters with log-normal distributions. In the  $CL_S$  method the uncertainties are treated differently depending on the method used to perform the statistical inference. In the HybridNew method which is prescribed by both CMS and ATLAS experiments to compute upper limits the uncertainties are treated according to the Frequentists methods by “marginalizing” the likelihood i.e. integrating out all the nuisance parameters.

### Test-Statistics and *p*-values

According to the Neyman-Pearson theorem the profile likelihood ratio gives the most powerful hypothesis test [63]. Therefore using the marginalized likelihood function we define the *profile likelihood* ratio (for simplicity, instead of writing the explicit dependence of  $\mathcal{L}$  on  $n_i$  we write  $\mathcal{L}$  in terms of the parameters) as

$$\lambda(\mu) = \frac{\mathcal{L}(\mu, \hat{\theta})}{\mathcal{L}(\hat{\mu}, \hat{\theta})} \quad (7.4)$$

where  $\hat{\theta}$  is the *conditional maximum-likelihood estimator* (CMLE) of  $\theta$  and it is the value of  $\theta$  that maximizes  $\mathcal{L}$  for a fixed value of  $\mu$ .  $\hat{\theta}$  is a function of  $\mu$ .  $\mathcal{L}(\hat{\mu}, \hat{\theta})$  is the maximized (unconditional) likelihood function with  $\hat{\mu}$  and  $\hat{\theta}$  being its *maximum likelihood* (ML) estimators for each Monte Carlo simulated toy experiment or real data. The nuisance parameter causes a broadening of the distribution of the profile likelihood ratio and this reflects the loss in sensitivity or loss of information about the parameter  $\mu$  due to the uncertainties.

The expression for  $\lambda(\mu)$  given in Equation 7.3 suggest that  $0 \leq \lambda(\mu) \leq 1$ . When  $\lambda(\mu)$  is close to 1 it means  $\mu$  is compatible with data. Thus, in order to assess the agreement between the observed data with either the background-only or signal plus background hypothesis we define a quantity called the *test-statistics*. The test-statistics is used to distinguish between two hypothesis based on the agreement of their predictions with data. Our choice of test-statistics is the *profile log-likelihood ratio* given as

$$q_\mu = -2 \ln \lambda(\mu), \quad (7.5)$$

with the compatibility between these hypothesis and data taking an even more simpler interpretation: higher values of the test-statistics indicates that the assumed level of the signal represented by the value of  $\mu$  is incompatible with data compared to the background-only hypothesis. The level of incompatibility is quantified using a probability or *p*-value which is derived from the Probability Density Distribution (PDD) of the test-statistics,  $f(q_\mu|\mu)$ . The analytic evaluation of  $f(q_\mu|\mu)$  is generally very difficult so in practice  $f(q_\mu|\mu)$  is approximated by evaluating  $q_\mu$  for a large number of simulated toy

experiments with the simulated data obtained by Monte-Carlo generating Poissonian random numbers with the expected number of events according to the model prediction for a given value of  $\mu$ . By repeating this process for different values of  $\mu$  we sample the distribution of  $f(q_\mu|\mu)$ .

For the signal plus background hypothesis, the  $p$ -value for the signal plus background hypothesis being compatible with the data is evaluated as

$$CL_{s+b}^{(\mu)} = p_{s+b} = \int_{q_\mu^{obs}}^{\infty} f(q_\mu|\mu) dq_\mu, \quad (7.6)$$

where  $q_\mu^{obs}$  is the value of the test-statistics ( $q_\mu$ ) from the real data. Large values of  $CL_{s+b}^{(\mu)}$  suggests that chances are high that the observation is compatible with the prediction of the signal plus background hypothesis.

For the background-only hypothesis, the test-statistics is defined with  $\mu = 0$  as

$$q_\mu = \begin{cases} -2 \ln \lambda(0), & \hat{\mu} \geq 0 \\ 0, & \hat{\mu} \leq 0 \end{cases}$$

where  $\lambda(0)$  is the profile log-likelihood ratio with  $\mu = 0$  defined in Equation 7.4. The probability or  $p$ -value for the background-only ( $\mu = 0$ ) hypothesis being compatible with the data is evaluated as

$$CL_b^{(\mu)} = 1 - p_b = \int_{q_\mu^{obs}}^{\infty} f(q_\mu|0) dq_\mu, \quad (7.7)$$

where  $f(q_\mu|0)$  is the PDD of the test-statistics,  $q_{\mu=0}$ , under the background-only ( $\mu = 0$ ) hypothesis and is also approximated using simulated toy experiments. The  $CL_b$  probability measures the disagreement of the data and the prediction from the background-only hypothesis.

### The $CL_S$ value and exclusion limits

Using Equations 7.1.3 and 7.7 the probability,  $CL_S^{(\mu)}$ , given as

$$CL_S^{(\mu)} \equiv \frac{CL_{s+b}^{(\mu)}}{CL_b^{(\mu)}}, \quad (7.8)$$

measures how well we can statistically distinguish the signal plus background from the background only hypothesis looking at the data. Small values of the  $CL_S^{(\mu)}$  indicates that the data strongly favors the background-only hypothesis over the signal plus background hypothesis.

The  $CL_S^{(\mu)}$  is used to obtain an exclusion limit on the POI,  $\mu$ , with some confidence level commonly referred to as  $CL_S^{(\mu)}$  Confidence Levels (CL). By increasing the value of  $\mu$  (increasing the contribution of the signal) the  $CL_S^{(\mu)}$  decreases down to a certain threshold value. The threshold value for which  $CL_S^{(\mu^{UL})} = \alpha$  is the **upper limit** for  $\mu$  at the desired  $1 - \alpha\%$  CL. At 95%  $CL_S$  confidence level,  $\alpha = 0.05$ .

From the observed data, the observed test-statistics,  $q_\mu^{obs}$ , gives the **observed** upper limit and the interpretation of the limit is such a prediction by the signal plus background hypothesis corresponding to  $\mu > \mu_{obs}^{UL}$  is excluded at a 95% CL and  $\mu_{obs}^{UL}$  is the upper limit of  $\mu$ .

From the simulated toy Monte Carlo data, the median of the test-statistics obtained from the background-only hypothesis with  $\mu = 0$  gives the **expected** exclusion limit ( $\mu_{med}^{UL}$ ) of the SPS8 benchmark GMSB model. This expected limit is used to quantify the sensitivity of the search experiment.

In addition to the expected limit we are also interested in quantifying the range of possible statistical deviations from the median i.e. how much the expected exclusion limit can statistically fluctuate upward or downward due to statistical uncertainties and so we evaluate the 68% ( $+1\sigma$ ), 16% ( $-1\sigma$ ), 98% ( $+2\sigma$ ) and 2.5% ( $-2\sigma$ ) errors on the median. The exclusion limits obtained with the  $CL_S$  method are presented in exclusion plot where the observed limits obtained from the experiment and the expected limits are displayed simultaneously. Figure 7.2 shows an exclusion plot where the dashed red line represent the expected limit while the **green** and **yellow** bands represents the  $\pm 1\sigma$  and  $\pm 2\sigma$  errors on the expected limit, respectively. These deviations from the median

expected limit allows us to assess the exclusion potential of the search experiment. The **observed** limit is indicated by the solid black line.

## 7.2 Limit Interpretation in the SPS8 Benchmark GMSB Model

We set upper limits at 95%  $CL_S$  confidence level on the product of the production cross-section and branching ratio for the decay of the lightest neutralino ( $\tilde{\chi}_1^0$ ) into a photon ( $\gamma$ ) and gravitino ( $\tilde{G}$ ) as predicted by the SPS8 benchmark GMSB model. The exclusion limits are presented in an exclusion plot as a function of the mean lifetime,  $\tau_{\tilde{\chi}_1^0}$  (ns), and the mass of the lightest neutralino,  $m_{\tilde{\chi}_1^0}$  (GeV/c<sup>2</sup>), or equivalently the effective SUSY breaking scale,  $\Lambda$  (TeV).

### 7.2.1 Cross-section Upper Limits

The HIGGS COMBINE tool gives us an upper limit on the number of events,  $N_{UL}$ , and knowing our signal event selection efficiency ( $\varepsilon$ ) and acceptance ( $A$ ) we can compute the upper limit on the cross-section as

$$\sigma_{UL} = \frac{N_{UL}}{\varepsilon \times A \cdot \mathcal{L}}, \quad (7.9)$$

where  $\mathcal{L}$  is the integrated luminosity (19 fb<sup>-1</sup>).

#### Signal Efficiency and Acceptance

The plot in Figure 7.1 shows our signal event selection efficiency and acceptance for events from signal MC samples for different mean lifetime or *proper decay length*,  $c\tau$ , ranging from 500 mm ( $\tau = 1.7$  ns) to 6000 mm ( $\tau = 20.0$  ns) with the same lightest neutralino mass of 255 GeV/c<sup>2</sup> or equivalently  $\Lambda = 180$  TeV.

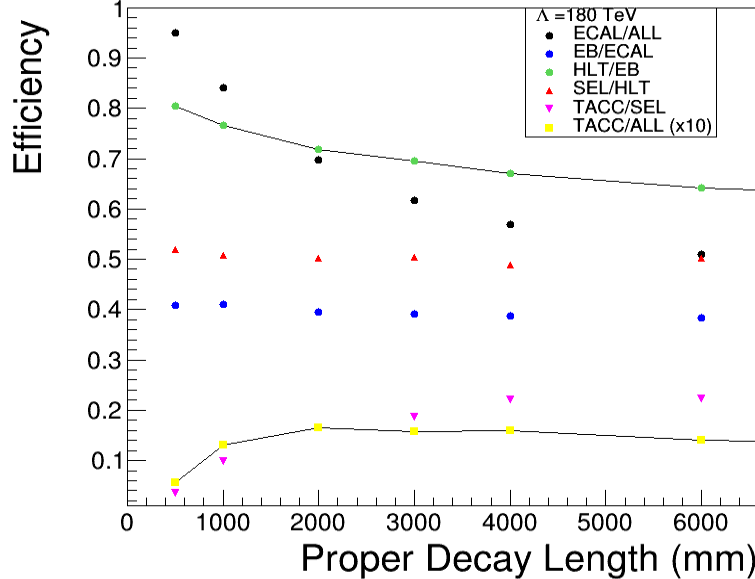


Figure 7.1: The efficiency for different mean decay length,  $c\tau$  [ mm ] with  $\Lambda = 180$  TeV. TACC/ALL (yellow square markers) is the Efficiency  $\times$  Acceptance( $t > 3$  ns) i.e.  $\varepsilon \times A$ , used in evaluating the exclusion limits. The TACC/ALL is magnified by factor  $\times 10$  for display purpose.

The efficiency plot is described as follows: ALL means all the photons from the decay of the MC generated lightest neutralino, ECAL means the photons in barrel (EB) and endcaps (EE) inclusive, EB means only reconstructed photons in EB are selected, HLT means the photon triggered our HLT trigger, SEL means the events passed our event selection requirement and TACC means the event pass our event selection and the photon acceptance of  $t > 3.0$  ns. Each ratio defines an efficiency at a different event selection stage. The important efficiency to focus on is the TACC/ALL defined as the ratio of the events passing our event selection with photon time greater than 3 ns in the barrel to all the events with photons from the decay of the generated lightest neutralino since this is the efficiency times acceptance ( $\varepsilon \times A$ ) used in Equation 7.9 to evaluate the exclusion limits on the cross-section.

The efficiency times acceptance, TACC/ALL, is small (less than 1%) for smaller values of  $c\tau = 500$  mm ( $\tau = 1.7$  ns) since very few of the events from the lightest neutralino decay have photons with time more than 3 ns despite many of the photons reaching

ECAL as shown by the ECAL/ALL efficiency which is defined as the ratio of events with photons reaching ECAL to all events with photons from the decay of the generated lightest neutralino. This indicates that the efficiency without the 3.0 ns requirement is high for low  $c\tau$  values. The TACC/ALL begins to slowly rise with  $c\tau$  up to  $c\tau = 2000$  mm ( $\tau = 6.7$  ns) where it has a maximum value of about 1.6% and then begins to fall again (less than 1%) for large  $c\tau$  values. The fall with large  $c\tau$  values ( $c\tau > 6000$  mm) is because most of the lightest neutralinos decay outside of the ECAL and the photon is undetected.

The theory prediction for the product of the lightest neutralino production cross-section and branching ratio ( $\sigma \times BR_{\tilde{\chi}_1^0}$ ) decay to a photon and gravitino channel,  $\tilde{\chi}_1^0 \rightarrow \gamma + \tilde{G}$ , by the SPS8 benchmark GMSB model at Leading Order (LO) interactions for an effective SUSY breaking scale,  $\Lambda = 180$  TeV is 0.015 pb, indicated by the blue line in Figure 7.2. The theoretical cross-section decreases with increasing values of  $\Lambda$  as shown in Figure 7.3.

Prior to this search experiment, the upper limit set on  $\sigma \times BR_{\tilde{\chi}_1^0}$  by CMS was  $\sigma \times BR_{\tilde{\chi}_1^0} < 0.02$  pb for a lightest neutralino mass of 215 GeV/c<sup>2</sup> or equivalently  $\Lambda = 154$  TeV and  $c\tau = 1$  mm [26]. From the results of this search experiment, using Equation 7.9 we set an upper limit of  $\sigma \times BR_{\tilde{\chi}_1^0} < 0.0125$  pb and which is translated into the mean lifetime of the lightest neutralino,  $\tau_{\tilde{\chi}_1^0}$ , to be either less than 3.2 ns or larger than 19.87 ns for mass of lightest neutralino,  $m_{\tilde{\chi}_1^0} = 255$  GeV/c<sup>2</sup>, or equivalently  $\Lambda = 180$  TeV as shown in Figure 7.2. For lightest neutralinos with different masses and lifetimes the corresponding cross-section upper limits can be read directly from Figure 7.5 which is the region in parameter space described by  $\Lambda$  and  $\tau_{\tilde{\chi}_1^0}$  where the ECAL sub-detector is most sensitive to late photons.

### 7.2.2 Mass and Lifetime Upper Limits

The excluded region in the mass and mean lifetime of the lightest neutralino are the values  $\tau_{\tilde{\chi}_1^0}$  and  $m_{\tilde{\chi}_1^0}$  or equivalently  $\Lambda$  for which the observed  $\sigma \times BR_{\tilde{\chi}_1^0}$  is lower than the predicted  $\sigma \times BR_{\tilde{\chi}_1^0}$  by the SPS8 benchmark GMSB model i.e. the point where the observed cross-section and the theoretical cross-section intersect is upper limit and all the values of  $\tau_{\tilde{\chi}_1^0}$  and  $m_{\tilde{\chi}_1^0}$  where the observed is below the theoretical prediction are said to be excluded. In Figure 7.2 which shows  $\sigma \times BR_{\tilde{\chi}_1^0}$  at 95%  $CL_S$  confidence level as

a function of the mean lifetime,  $\tau_{\tilde{\chi}_1^0}$ , for  $\Lambda = 180 \text{ TeV}$ , we find that lightest neutralinos with lifetime  $3.2 \text{ ns} \leq \tau_{\tilde{\chi}_1^0} < 19.87 \text{ ns}$  are excluded and in Figure 7.3 showing  $\sigma \times BR_{\tilde{\chi}_1^0}$  at 95%  $CL_S$  confidence level as a function of  $m_{\tilde{\chi}_1^0}$  or equivalently,  $\Lambda$  for  $\tau_{\tilde{\chi}_1^0} = 6.7 \text{ ns}$  we find that lightest neutralinos with mass less than  $275 \text{ GeV}/c^2$  or  $\Lambda < 195 \text{ TeV}$  described by the SPS8 benchmark GMSB model have been excluded.

In a two dimensional exclusion plot defined by  $(\Lambda, \tau_{\tilde{\chi}_1^0})$ , the excluded lightest neutralino mean lifetime,  $\tau_{\tilde{\chi}_1^0}$ , is from  $2.0 \text{ ns}$  to  $45.0 \text{ ns}$  for low mass ( $m_{\tilde{\chi}_1^0} < 150 \text{ GeV}/c^2$ ) lightest neutralino while for larger masses up to  $m_{\tilde{\chi}_1^0} \leq 300 \text{ GeV}/c^2$  or  $\Lambda \leq 220 \text{ TeV}$ , lightest neutralinos with lifetime less than  $10 \text{ ns}$  have been excluded as shown in Figure 7.4. The shaded regions are the excluded regions in lifetimes and mass of lightest neutralinos as described by the SPS8 benchmark GMSB model by different experiments (CDF,ATLAS(7 TeV,8 TeV),CMS(7 TeV)) and our current CMS 8 TeV analysis. This excluded region in mean lifetime shrinks as the mass of the lightest neutralino increases or equivalently the effective SUSY breaking scale increases. This is because the expected production cross-section for the lightest neutralino decreases with increasing effective SUSY breaking scale.

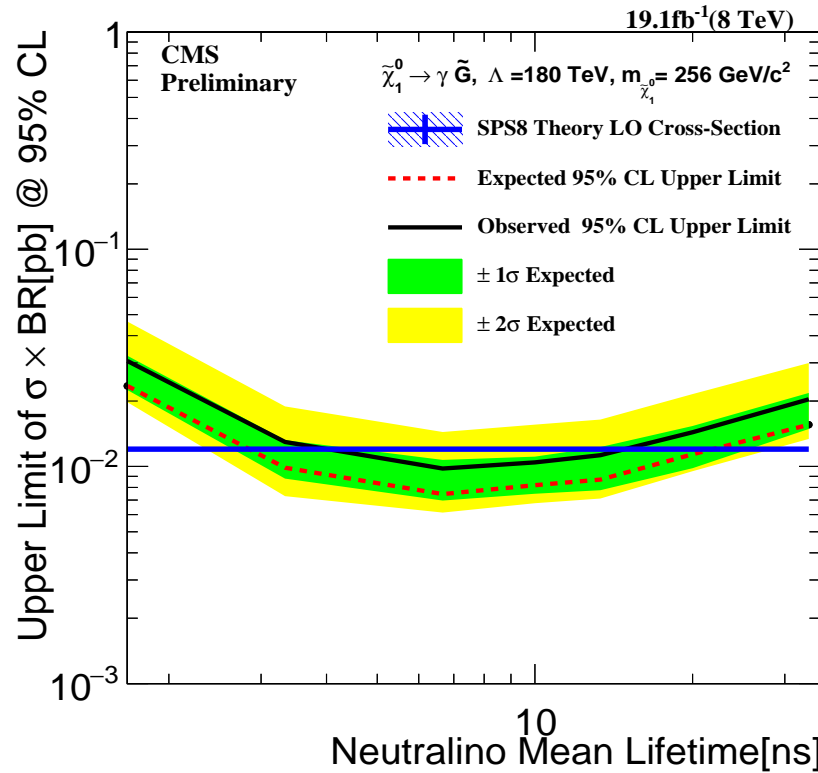


Figure 7.2: 95%  $CL_S$  CL on the lightest neutralino production cross-section times branching ratio ( $\sigma \times BR$ )[ pb ] against mean lifetime[ ns ] for  $\Lambda = 180 \text{ TeV}$  in the SPS8 benchmark GMSB model.

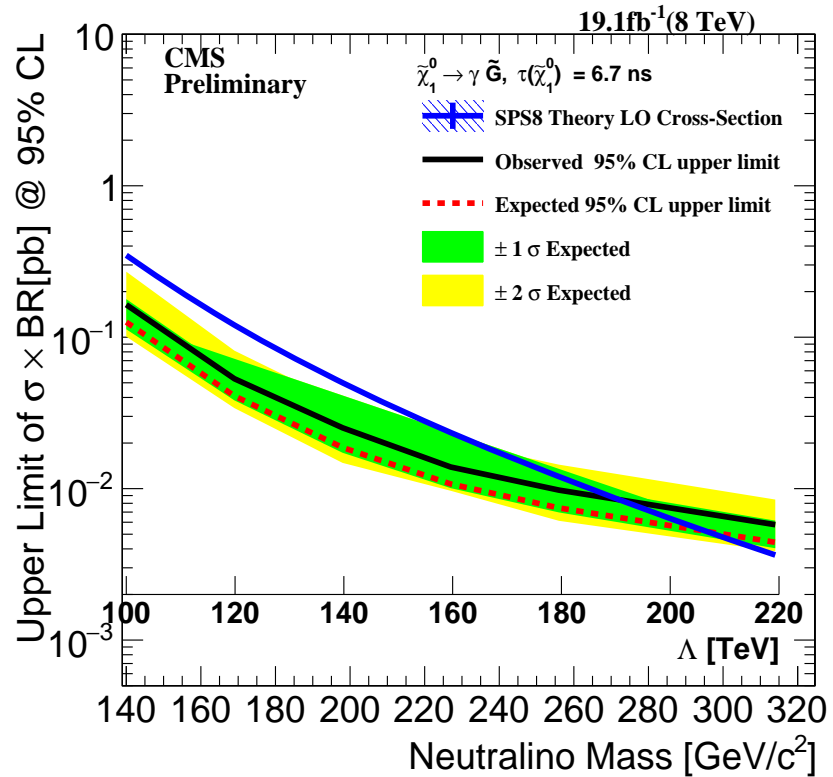


Figure 7.3: 95%  $CL_S$  CL on the lightest neutralino production cross-section times branching ratio ( $\sigma \times BR$ ) for different  $\Lambda$  (or mass of lightest neutralino) for  $\tau = 6.7$  ns ( $c\tau = 2000$  mm) in the SPS8 benchmark GMSB model.

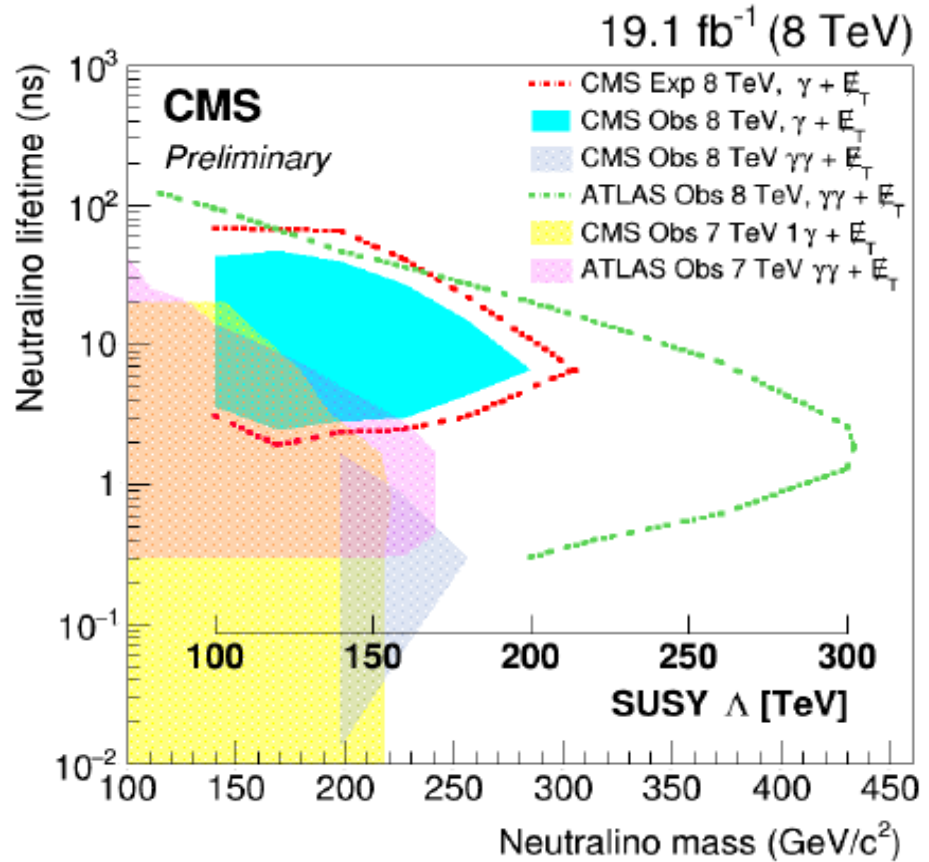


Figure 7.4: Exclusion limit in lightest neutralino mass (or  $\Lambda$ ) against mean lifetime in SPS8 benchmark GMSB model. Limits from previous experiments also shown.

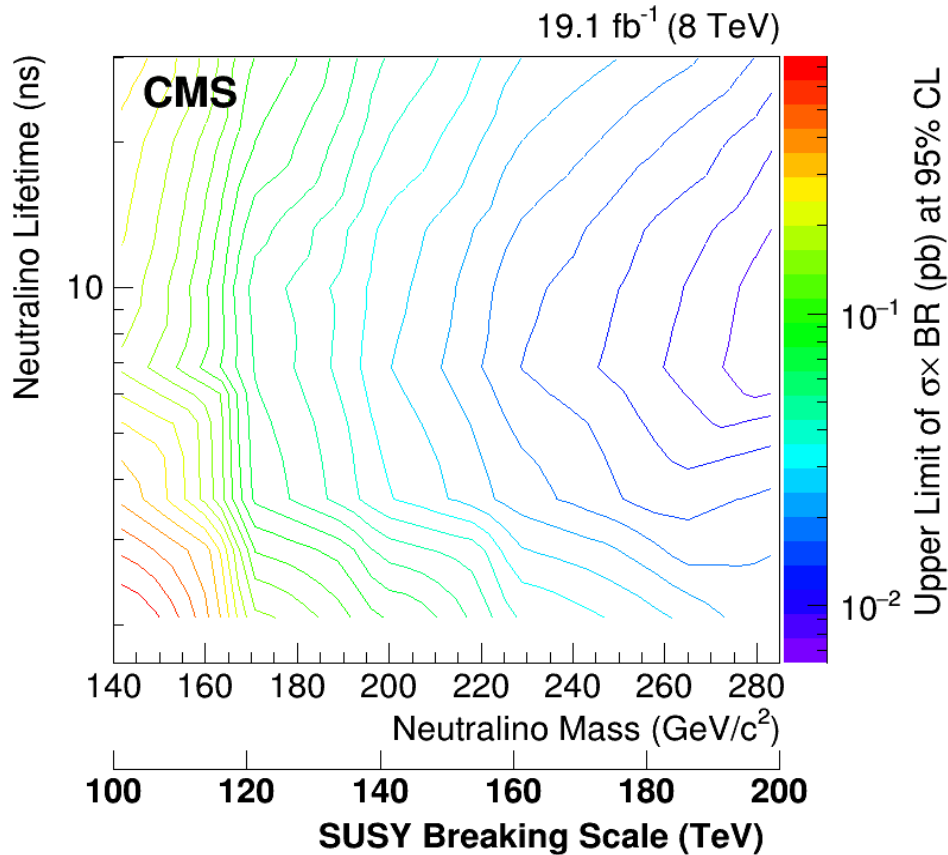


Figure 7.5: Cross-section upper limits at 95%  $CL_S$  CL for different mass and lifetime of the lightest neutralino using 8 TeV data corresponding to an integrated luminosity of  $19.1 \text{ fb}^{-1}$  of the CMS experiment.

## Chapter 8

# Conclusion

We perform a search for delayed photons which may be produced from, for example, the decay of the lightest neutralino which is a Long-Lived Neutral Particle (LLNP) by measuring the arrival time of the photon with CMS Electromagnetic Calorimeter (ECAL). This search was carried out on the data recorded by the CMS detector equivalent to  $19.1 \text{ fb}^{-1}$  of integrated luminosity from LHC proton-proton collisions at a center-of-mass energy of 8 TeV.

Our exclusion limits on the lifetime, mass of lightest neutralino or effective SUSY breaking scale and the production cross section times branching ratio are the strongest limits using timing measurements alone to search for events with delayed photon. This is the first time that the CMS ECAL timing has been used as the only search quantity to search for LLNPs and the results demonstrate that CMS ECAL timing has good sensitivity and provides a reference for measuring future improvement on the sensitivity from additional search quantities, particularly in search experiments which use a combination different search quantities.

# Bibliography

- [1] N. Jarosik et al. (WMAP), *Astrophys. J. Suppl.* **192**, 14 (2011); Overview: K.A. Olive et al.(PDG), *Chin.Phys.C***38**,090001(2014).
- [2] Ellis John, Olive Keith A. (2010). *Supersymmetric Dark Matter Candidates*. arXiv:1001.3651 [astro-ph]
- [3] Laura Covi, *Gravitino Dark Matter confronts LHC*, Journal of Physics: Conference Series 485 (2014) 012002
- [4] M. Kuhlen, M Vogelsberger, R. Angulo, *Phys.Dark Univ.***1**,50(2012).
- [5] J.Ellis, J.Hagelin, D. Nanopoulos, K.A. Olive and M. Srednicki; *Nucl. Phys.* B238 (1984) 453; H. Goldberg, *Phys. Rev. Lett* 50 (1983) 1419; J. Ellis, T. Falk, G. Ganis, K.A. Olive and M. Srednicki, *Phys. Lett. B* 510 (2001) 236, arXiv: hep-ph/0102098.
- [6] K.A. Olive et al. (Particle Data Group), *Chin. Phys. C*, 38, 090001 (2014).
- [7] Steven Weinberg, *A Model of Leptons*, *Phys. Rev. Lett.* 19, 12641266 (1967)
- [8] Peter W. Higgs, *Broken symmetries and the masses of gauge bosons*, *Phys.Rev.Lett.* 13.508,19 October, 1964;
- [9] *Observation of a new boson at a mass of 125 GeV with the CMS experiment at LHC*, *Phys. Lett. B* 716 (2012) 30-61
- [10] Haag, Rudolf; Sohnius, Martin; opuszaski, Jan T. *All possible generators of supersymmetries of the S-matrix*, *Nuclear Physics* B88: 257274 (1975),

- [11] Salam, A.; Strathdee, J. (1974). *Super-gauge transformations*. Nuclear Physics B 76 (3): 477201,
- [12] Ian J. R. Aitchison, *Supersymmetry and the MSSM: An Elementary Introduction*, arXiv:hep-ph/0505105,
- [13] S.Mathin, *Supersymmetry Primer*, arXiv:hep-ph/9709356,
- [14] H. Nilles, *Supersymmetry, Supergravity and Particle Physics*, Phys. Rept. 110(1984) 1.
- [15] Howard Baer, Xerxes Tata, *Weak Scale Supersymmetry:From Superfields to Scattering Events*.
- [16] G.F. Giudice and R. Rattazzi, *Theories with Gauge-Mediated Supersymmetry Breaking* arXiv:hep-ph/9801271v2.
- [17] S. Ambrosanio, Graham D. Kribs, and Stephen P. Martin, arXiv:hep-ph/9703211  
arXiv:hep-ph/9703211v2.
- [18] B.Allanach et al, arXiv:hep-ph/0202233v1.
- [19] D.del Re et al, *An algorithm for the determination of the flight path of long-lived particles decaying into photons*, CMS AN -2010/212.
- [20] T. Sj ostrand, S. Mrenna, and P. Skands, *PYTHIA 6.4 physics and manual*, JHEP 05 (2006) 026, doi:10.1088/1126-6708/2006/05/026, arXiv:hep-ph/0603175
- [21] ISAJET 7.84, F.E. Paige, S.D. Protopopescu, H. Baer and X. Tata,  
<http://www.nhn.ou.edu/> isajet/
- [22] GEANT4 Collaboration, *GEANT4a simulation toolkit*, Nucl. Instrum. Meth. A 506(2003) 250, doi:10.1016/S0168-9002(03)01368-8.
- [23] J.Dann et al.(LEPSUSY Working Group), Internal note LEPSUSYWG/97-04(1997), P. Janot, talk at the EPS Conference, Jerusalem, 1997.
- [24] CDF Collaboration, *Search for Supersymmetry with Gauge-Mediated Breaking in Diphoton Events with Missing Transverse Energy at CDFII*, Phys. Rev. Lett.

- [25] ATLAS Collaboration *Search for Diphoton Events with Large Missing Transverse Momentum in 1  $fb^{-1}$  of 7TeV Proton-Proton Collision Data with the ATLAS Detector*, arXiv:1111.4116v1, 17th Nov 2011.
- [26] CMS Draft Analysis, *Search for Long-Lived Particles using Displaced Photons in PP Collision at  $\sqrt{S} = 7$  TeV*, CMS AN AN-11-081 104(2010)011801,
- [27] ATLAS Collaboration, J. High Energy Phys. 1212, 124 (2012), arXiv:1210.4457 [hep-ex]
- [28] The LHC Machine, Lyndon Evans and Philip Bryant *Jinst*,
- [29] CMS Collaboration, *CMS Physics: Technical design report*, Volume 1 CERN-LHCC-2006-001.
- [30] CMS Collaboration, *CMS Physics: Technical design report, Volume 2* CERN-LHCC-2006-001.
- [31] A. Jeff et al *Measurement of Satellite Bunches at the LHC*, slac-pub-15737, slac-pub-16058.
- [32] *Study of the LHC ghost charge and satellite bunches for luminosity calibration.*, CERN-ATS-Note-2012-029 PERF
- [33] *LHC bunch current normalization for the April-May 2010 luminosity calibration measurements.*, CERN-ATS-Note-2011-004 PERF
- [34] CMS Collaboration, *The CMS experiment at the CERN LHC*, JINST 0803:S08004, 2008.
- [35] CMS Collaboration, *The electromagnetic calorimeter. Technical design report.*, CERN-LHCC-97-33.
- [36] Bo Lofstedt, *The digital readout system for the CMS electromagnetic Calorimeter*, Nucl. Inst. Methods in Physics Research, A 453 (2000) 433-439.
- [37] J. Valera et al *Trigger Synchronization Circuits in CMS*, CMS CR 1997/017.

- [38] CMS Electromagnetic Calorimeter Collaboration, *Energy resolution of the barrel of the CMS Electromagnetic Calorimeter*, JINST 2(2007)P04004.
- [39] CMS Collaboration, *Reconstruction of the signal amplitude of the CMS electromagnetic Calorimeter*, Eur.Phys.J. C46S1(2006)23-35.
- [40] CMS Collaboration, *Time Reconstruction and Performance of the CMS Crystal Electromagnetic Calorimeter*, CFT-09-006, 2009.
- [41] <https://twiki.cern.ch/twiki/bin/viewauth/CMS/ECALDPGTimeCalibration>
- [42] <https://twiki.cern.ch/twiki/bin/viewauth/CMS/ECALDPGHwTimeCalibration>
- [43] CMS Collaboration, *The CMS ECAL performance With examples*, JINST 9 C02008, 2014.
- [44] Daniele Del Re for CMS Collaboration, *Timing performance of the CMS electromagnetic calorimeter and prospects for the future.*, CMS-CR-2014/074
- [45] CMS-DP-2014/011: *ECAL Timing Performance Run1*
- [46] <https://twiki.cern.ch/twiki/bin/view/CMSPublic/EcalDPGResultsCMSDP2014011>
- [47] <https://twiki.cern.ch/twiki/bin/view/CMSPublic/EcalDPGResultsCMSDP2014012>
- [48] Florian Beaudette (the CMS Collaboration), *The CMS Particle Flow Algorithm*, arXiv:1401.8155 [hep-ex].
- [49] CMS Collaboration, *Particle-Flow Event Reconstruction in CMS and Performance for Jets, taus and  $\cancel{E}_T$*  CMS Physics Analysis Summary CMS-PAS-PFT-09-001(2009).
- [50] CMS Collaboration, *Jet Performance in pp Collisions at  $\sqrt{S} = 7$  TeV*, CMS PAS JME-10-003 (2010).
- [51] CMS Collaboration, *8 TeV Jet Energy Corrections and Uncertainties based on  $19.8 \text{ fb}^{-1}$  of data in CMS*, CMS-DP-2013-033 ; CERN-CMS-DP-2013-033, *Jet Energy Corrections and Uncertainties*, CMS Public Note CMS-DP-2012/012.

- [52] CMS Collaboration, *Missing Transverse Energy Performance in Minimum-Bias and Jet Events from Proton-Proton Collisions at  $\sqrt{s} = 7$  TeV*, CMS Physics Analysis Summary CMS-PAS-JME-10-004 (2010).
- [53] CMS Collaboration, *Missing transverse energy performance of the CMS detector*, arXiv:1106.5048v1., Missing Transverse Energy, JINST ,arXiv:1106.5048.
- [54] *Characterization and treatment of anomalous signals in the CMS Electromagnetic Calorimeter* CMS AN AN-10-357.
- [55] *Mitigation of Anomalous APD signals in the CMS ECAL,2013*, JINST 8 C03020, W.Bialas and D.A. Petyt.
- [56] *Presentation of search results: the CLs technique*,A L Read 2002 J. Phys. G: Nucl. Part. Phys. 28 2693.
- [57] *Computation of confidence levels for search experiments with fractional event counting and the treatment of systematic errors*, Peter Bock JHEP01(2007)080.
- [58] “<https://twiki.cern.ch/twiki/bin/viewauth/CMS/EGamma2012>.”
- [59] CMS Collaboration,*Determination of Jet Energy Scale in CMS with pp collisions at  $\sqrt{S} = 8$  TeV*, JME-10-010(2012).
- [60] CMS Collaboration, *Search for ADD Extra-dimensions with Photon + MET signature*, AN-11-319(2011).
- [61] *Parton distributions for the LHC*, Eur.Phys.J C63(2009) 189-285 or arXiv:0901.0002.
- [62] <https://twiki.cern.ch/twiki/bin/viewauth/CMS/>
- [63] Neyman, Jerzy; Pearson, Egon S. (1933), *On the Problem of the Most Efficient Tests of Statistical Hypotheses*. Philosophical Transactions of the Royal Society A: Mathematical, Physical and Engineering Sciences 231 (694706): 289337

## Appendix A

# Glossary and Acronyms

Care has been taken in this thesis to minimize the use of jargon and acronyms, but this cannot always be achieved. This appendix defines jargon terms in a glossary, and contains a table of acronyms and their meaning.

### A.1 Glossary

- **Cosmic-Ray Muon (CR  $\mu$ )** – A muon coming from the abundant energetic particles originating outside of the Earth’s atmosphere.
- **SUSY** – A theoretical model based on a fundamental symmetry called supersymmetry in which the fermions and bosons can exchange their spin, extending the standard model to account for the stability in the observed Higgs boson mass and to also predicting the existence of many extra new particles which could be candidates of dark matter.
- **CMS Coordinate System** – CMS uses a right-handed coordinate system, with the origin at the nominal interaction point, the  $x$ -axis pointing to the center of the LHC, the  $y$ -axis pointing up (perpendicular to the LHC plane), and the  $z$ -axis along the counterclockwise-beam direction. The polar angle,  $\theta$ , is measured from the positive  $z$ -axis and the azimuthal angle,  $\phi$ , is measured in the  $x$ - $y$  plane.
- **Eta** –

$$\eta = -\ln \tan(\theta/2) \tag{A.1}$$

- **Transverse Energy and Momentum** – The transverse energy and momentum are defined as

$$E_T = E \sin \theta \quad (\text{A.2})$$

$$p_T = p \sin \theta \quad (\text{A.3})$$

where  $p$  is the momentum measured in the tracking system and  $E$  is the energy measured in the calorimeters.

- **Missing Transverse Energy** or  $E_T^{\text{miss}}$

$$E_T^{\text{miss}} = \left| - \sum_i E_T^i \vec{n}_i \right| \quad (\text{A.4})$$

where  $\vec{n}_i$  is a unit vector that points from the interaction vertex to the transverse plane.

## A.2 Acronyms

Table A.1: Acronyms

LLNP	Long-Lived Neutral Particle.
DM	Dark Matter.
DE	Dark Energy.
SM	Standard Model
BSM	Beyond Standard Model
SUSY	Supersymmetry
GMSB	Gauge Mediated Supersymmetry Breaking
LHC	Large Hadron Collider
CMS	Compact Muon Solenoid
DAQ	Data Acquisition Board
FPGA	Field Programmable Gate Arrays
ASIC	Application Specific Integrated Circuits
CR $\mu$	Cosmic-Ray Muon

## A.3 Analysis How To and Data Samples

### A.3.1 Check Out Software Packages

To check out the analysis packages, do the following steps:

- `cmsrel CMSSW_5_3_29`
- `cd CMSSW_5_3_29\src`

### A.3.2 Data Samples

In Table A.2 show the data samples and the corresponding integrated luminosity.

The *jason* file with the list of certified good luminosity sections is

**Cert\_8TeV\_PromptReco\_Collisions12\_JASON.txt**.

<b>Data Sample</b>	<b>Recorded Luminosity</b> [fb <sup>-1</sup> ]
/Run2012B/SinglePhoton/ <b>EXODisplacedPhoton-PromptSkim-v3</b>	5.1
/Run2012C/SinglePhoton/ <b>EXODisplacedPhoton-PromptSkim-v3</b>	6.9
/Run2012D/SinglePhoton/ <b>EXODisplacedPhoton-PromptSkim-v3</b>	7.1
/SingleElectron/Run2012A-22Jan2013-v1/AOD	5.2
/DoubleElectron/Run2012C-22Jan2013-v1/AOD	4.8

Table A.2: Data samples and their corresponding integrated luminosity totaling 19.1 fb<sup>-1</sup> used in the our delayed photon search analysis